

# University of St Andrews



Full metadata for this thesis is available in  
St Andrews Research Repository  
at:

<http://research-repository.st-andrews.ac.uk/>

This thesis is protected by original copyright

L

Angular momentum of light, self-imaging beams,  
and fractal resonator modes

Johannes Courtial

Ph. D. thesis  
University of St Andrews

May 11, 1999



## Abstract

In this thesis work on the angular momentum of light and related topics is described.

The fundamentals of angular momentum, both in mechanics and in quantum mechanics, are reviewed in chapter 1 and an introduction into the angular momentum of light and the important Laguerre-Gaussian (LG) modes is given.

In chapter 2 the performance of the cylindrical-lens mode converter for transforming Hermite-Gaussian modes into Laguerre-Gaussian modes is modelled. The implications of incorrect lens positioning or focussing of the input mode are analysed.

In chapter 3 it is shown that the so-called elliptical Gaussian light beams with general astigmatism can contain orbital angular momentum.

In chapter 4 the frequency doubling of multi-ringed ( $p > 0$ ) Laguerre-Gaussian modes is examined. Unlike that of a single-ringed ( $p = 0$ ) LG mode, the second harmonic of a multi-ringed LG mode is no longer a LG mode but a structurally unstable, self-imaging beam that satisfies the conservation of orbital angular momentum within the light beams.

Some theoretical insights concerning self-imaging beams, in particular their connection to other families of beams, are described in chapter 5.

A novel effect is introduced in chapter 6: the rotational Doppler shift. This shift, the rotational equivalent of the first-order Doppler effect, occurs when a light beam rotates with respect to the observer.

The polarisation state of a light beam is related to its spin angular momentum and can be represented on the Poincaré sphere. In chapter 7 a sphere for light beams in analogous orbital-angular-momentum states is constructed.

In chapter 8 fundamental design ideas for resonators with fractal eigenmodes are outlined. Preliminary numerical simulations of a "Sierpinski gasket eigenmode" are presented.

A computer program that incorporates an algorithm devised by Sziklas and Siegman to simulate the propagation of a light beam between two planes is discussed in appendix A.

## Publications

1. J. Courtial, K. Dholakia, L. Allen, and M. J. Padgett, "Gaussian beams with very high orbital angular momentum," *Opt. Commun.* **144**, 210–213 (1997)
2. J. Courtial, K. Dholakia, L. Allen, and M. J. Padgett, "Second harmonic generation and the observation of orbital angular momentum with high-order Laguerre-Gaussian modes," *Phys. Rev. A* **56**, 4193–4196 (1997)
3. J. Courtial, K. Dholakia, D. A. Robertson, L. Allen, and M. J. Padgett, "Measurement of the rotational frequency shift imparted to a rotating light beam possessing orbital angular momentum," *Phys. Rev. Lett.* **80**, 3217–3219 (1998)
4. J. Courtial, "Self-imaging beams and the Guoy effect," *Opt. Commun.* **151**, 1–4 (1998)
5. M. A. Clifford, J. Arlt, J. Courtial, and K. Dholakia, "High-Order Laguerre-Gaussian laser modes for studies of cold atoms," *Opt. Commun.* **156**, 300–306 (1998)
6. J. Courtial, D. A. Robertson, K. Dholakia, L. Allen, and M. J. Padgett, "Rotational frequency shift of a light beam," *Phys. Rev. Lett.* **81**, 4828–4830 (1998)
7. J. Courtial and M. J. Padgett, "Performance of a cylindrical lens mode converter for producing Laguerre-Gaussian laser modes," *Opt. Commun.* **159**, 13–18 (1999)
8. M. J. Padgett and J. Courtial, "A Poincaré-sphere equivalent for light beams containing orbital angular momentum," *Opt. Lett.* **24**, 430–432 (1999)

I, Johannes Courtial, hereby certify that this thesis, which is approximately 30,000 words in length, has been written by me, that it is the record of work carried out by me and that it has not been submitted in any previous application for a higher degree.

date 12/05/99 signature of candidate .

I was admitted as a research student in October 1994 and as a candidate for the degree of Ph. D. in October 1995; the higher study for which this is a record was carried out in the University of St Andrews between 1995 and 1998.

date 12/05/99 signature of candidate .

I hereby certify that the candidate has fulfilled the conditions of the Resolution and Regulations appropriate for the degree of Ph. D. in the University of St Andrews and that the candidate is qualified to submit this thesis in application for that degree.

date 12 May 99 signature of supervisor

In submitting this thesis to the University of St Andrews I understand that I am giving permission for it to be made available for use in accordance with the regulations of the University Library for the time being in force, subject to any copyright vested in the work not being affected thereby. I also understand that the title and abstract will be published, and that a copy of the work may be made and supplied to any bona fide library or research worker.

date 12/05/99 signature of candidate .

## Acknowledgements

Lots of thanks to Prof. Miles Padgett for being a very helpful, patient and enthusiastic supervisor and friend. Special thanks to the other people that I was essentially in constant contact with, Prof. L. Allen and Dr Kishan Dholakia. I am grateful to a lot of other people who helped me with my work, in particular Jochen Arlt, Paul Lesso, Karsten Siebert (University of Frankfurt (Germany)), Prof. W. Dultz (Deutsche Telekom AG, Darmstadt (Germany)), Brett Patterson, Prof. S. M. Barnett (University of Strathclyde), and Graham Gibson. Finally, thanks to all the other “Padgett people”, past and present, who were always very helpful and provided a very pleasant working atmosphere (in alphabetical order): Mark Begbie, Richard Conroy, Jacqueline Hewett, Tracy McKechnie, Anna O’Neil, Neil Simpson, and Darren Steers.



L. Allen

Jochen Arlt

Mark Begbie

Richard Conroy



Kishan Dholakia

Graham Gibson

Jacqueline Hewett

Paul Lesso

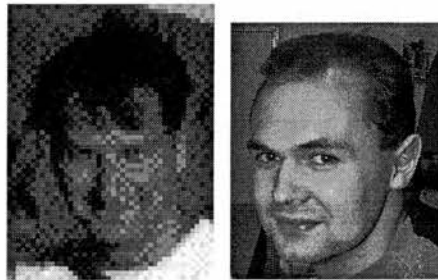


Tracy McKechnie

Anna O'Neil

Miles Padgett

Brett Patterson



Neil Simpson

Darren Steers

Figure 1: "Padgett people", past and present.

# Contents

<b>Publications</b>	<b>2</b>
<b>Acknowledgements</b>	<b>4</b>
<b>1 Angular momentum of light</b>	<b>9</b>
1.1 Introduction . . . . .	9
1.2 Angular momentum in mechanics . . . . .	10
1.2.1 Angular momentum and angular momentum density . . .	10
1.2.2 Independence from the reference point . . . . .	11
1.2.3 Conservation of angular momentum . . . . .	12
1.3 Angular momentum in quantum mechanics . . . . .	13
1.3.1 Angular momentum operators and rotations . . . . .	13
1.3.2 Spin and orbital angular momentum . . . . .	14
1.4 Angular momentum of light . . . . .	16
1.4.1 Milestones in the history of the angular momentum of light	16
1.4.2 Laguerre-Gaussian (LG) modes . . . . .	21
<b>2 Misaligned cylindrical-lens mode converters</b>	<b>27</b>
2.1 Introduction . . . . .	27
2.2 Modelling of the mode spectrum of a misaligned mode converter	28
<b>3 Propeller beams</b>	<b>37</b>
3.1 Introduction . . . . .	37
3.2 Orbital angular momentum content of propeller beams . . . . .	37
3.3 Phase structure of propeller beams . . . . .	40

<b>4</b>	<b>Frequency doubling of LG modes</b>	<b>45</b>
4.1	Introduction . . . . .	45
4.2	Frequency doubling of LG modes with $p = 0$ . . . . .	46
4.3	Frequency doubling of LG modes with $p > 0$ . . . . .	47
<b>5</b>	<b>Self-imaging beams and the Guoy phase</b>	<b>60</b>
5.1	Introduction . . . . .	60
5.2	Self-imaging superpositions of LG modes . . . . .	61
5.3	Spiral-type beams . . . . .	65
5.4	Structurally stable beams . . . . .	66
5.5	Self-imaging superpositions of other beams . . . . .	68
<b>6</b>	<b>Rotational Doppler effect</b>	<b>69</b>
6.1	Translational Doppler effect . . . . .	69
6.2	Rotational Doppler effect for circularly polarised light . . . . .	71
6.3	Rotational Doppler effect for light beams with helical phase fronts	73
6.3.1	Experiment . . . . .	76
6.4	Rotational Doppler effect for general light beams . . . . .	79
6.4.1	Experiment . . . . .	89
6.5	Rotational Doppler effect and translational Doppler effect of a rotating object . . . . .	89
<b>7</b>	<b>Sphere of first-order modes</b>	<b>91</b>
7.1	Introduction . . . . .	91
7.2	Poincaré sphere and the sphere of first-order modes . . . . .	91
7.3	Wave plates and mode converters . . . . .	94
7.4	Evolving geometric phase . . . . .	95
<b>8</b>	<b>Fractal resonator modes</b>	<b>98</b>
8.1	Self-similar fractals and multiple reduction copy machines . . . . .	98
8.2	Previous optical realisations of multiple reduction copy machines	99
8.3	A resonator with a Sierpinski-gasket eigenmode . . . . .	101
8.3.1	Numerical calculation of the eigenmodes . . . . .	103
8.4	Fractal lasers and atomic resonators . . . . .	108

<i>CONTENTS</i>	8
<b>A Beam propagation program</b>	<b>109</b>
A.1 Introduction . . . . .	109
A.2 Description of the algorithm . . . . .	114
A.3 Limitations of the beam propagation program . . . . .	115
<b>Bibliography</b>	<b>121</b>

# Chapter 1

## Angular momentum of light

### 1.1 Introduction

Sometimes it is difficult, perhaps even impossible to completely integrate the equations of motion for a mechanical system. However, this does not necessarily mean that nothing can be known about the time evolution of the system: usually the properties of its environment imply the conservation of certain quantities, for example energy or angular momentum (see section 1.2). Such conservation laws are very dear to the physicist as they can often be considered to express the essence of the dynamical evolution.

The angular momentum of closed systems is always conserved. The influence of the environment on many physical systems is so small that they can, to a very good approximation, be considered closed. Kepler's second law, for example, states that the radius vector from the Sun to the Earth sweeps over equal areas in equal times; this is an expression of the law of conservation of the angular momentum contained in the orbiting motion of the Earth. On a smaller scale, the conservation of angular momentum has direct consequences on molecular, atomic, or nuclear spectra.

That light can contain angular momentum has been known since 1909, when Poynting published his seminal work [1]. Nowadays it is universally accepted that light can contain spin angular momentum; however, it is still widely unknown that light can also contain orbital angular momentum. This thesis de-

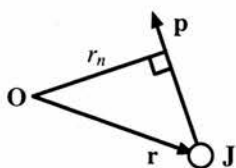


Figure 1.1: Angular momentum  $\mathbf{J}$  of a point mass  $m$  at position  $\mathbf{r}$  and with momentum  $\mathbf{p}$ . The vector  $\mathbf{J}$  points out of the paper plane and has a modulus of  $J = r_n p$ .

scribes a small part of the flurry of activity in the field of the angular momentum of light which was sparked off by the attribution of orbital angular momentum to the well-known Laguerre-Gaussian laser modes in 1992 [2].

For the understanding of the angular momentum of light, a number of concepts regarding angular momentum in mechanics and quantum mechanics are essential. Some of these are reviewed in the following two sections of this chapter. As an introduction into the angular momentum of light, the last section presents an outline of the history of the field.

## 1.2 Angular momentum in mechanics

### 1.2.1 Angular momentum and angular momentum density

The angular momentum of a set of point masses  $m_i$  at positions  $\mathbf{r}_i$  and with momenta  $\mathbf{p}_i$  is defined as [3]

$$\mathbf{J} = \sum_i \mathbf{r}_i \times \mathbf{p}_i. \quad (1.1)$$

Equation (1.1) can be considered the sum of the individual angular momenta associated with each point mass  $m_i$  at position  $\mathbf{r}_i$  and with momentum  $\mathbf{p}_i$ ,

$$\mathbf{J}_i = \mathbf{r}_i \times \mathbf{p}_i \quad (1.2)$$

(fig. 1.1).

A light field is not a set of point masses, but has associated with it a momentum distribution; it is therefore useful to generalise the concept of angular

momentum to continuous momentum distributions. The (infinitesimal) mass  $dm$  in the infinitesimal volume  $dV$  at position  $\mathbf{r}$  can be treated like a point mass, and the (infinitesimal) momentum  $d\mathbf{p}$  contained within the volume as the corresponding momentum. According to equation (1.2), it has associated with it an (infinitesimal) angular momentum of

$$d\mathbf{J} = \mathbf{r} \times d\mathbf{p}. \quad (1.3)$$

In analogy to equation (1.1), the total angular momentum associated with a momentum distribution  $d\mathbf{p}(\mathbf{r})$  can be expressed as

$$\mathbf{J} = \int \mathbf{r} \times d\mathbf{p}(\mathbf{r}). \quad (1.4)$$

If the momentum distribution  $d\mathbf{p}(\mathbf{r})$  is written in terms of the momentum density

$$\mathbf{p}_V(\mathbf{r}) = \frac{d\mathbf{p}(\mathbf{r})}{dV}, \quad (1.5)$$

the formula for the total angular momentum, equation (1.4), becomes

$$\mathbf{J} = \int \mathbf{r} \times \mathbf{p}_V dV. \quad (1.6)$$

In equation (1.6) the dependence on  $\mathbf{r}$  is not explicitly stated; unless it causes ambiguity, this practice will usually be followed in the rest of this thesis.

### 1.2.2 Independence from the reference point

In the above equations the angular momentum vector  $\mathbf{J}$  has been calculated with respect to the origin of the frame of reference,  $\mathbf{O}$ ; in the following discussion about the significance of this reference point, any angular momentum vector, or component thereof, that is calculated with respect to the origin will carry an index  $\mathbf{O}$ .

When calculated with respect to an arbitrary reference point at  $\mathbf{R}$ , expression (1.6) for the angular momentum associated with a momentum distribution becomes

$$\begin{aligned} \mathbf{J}_{\mathbf{R}} &= \int (\mathbf{r} - \mathbf{R}) \times \mathbf{p}_V dV \\ &= \left( \int \mathbf{r} \times \mathbf{p}_V dV \right) - \left( \mathbf{R} \times \int \mathbf{p}_V dV \right) \\ &= \mathbf{J}_{\mathbf{O}} - \mathbf{R} \times \mathbf{P}, \end{aligned} \quad (1.7)$$

where  $\mathbf{J}_0$  is the angular momentum calculated with respect to the origin and

$$\mathbf{P} = \int \mathbf{p}_V dV \quad (1.8)$$

is the total momentum of the distribution. It can be seen from equation (1.7) that the expression for  $\mathbf{J}_R$  is independent of  $\mathbf{R}$  if the total momentum of the momentum distribution is equal to zero. Perhaps more important, especially when dealing with the angular momentum associated with light beams, is the fact that the component of  $\mathbf{J}_R$  in the direction of  $\mathbf{P}$ ,

$$J_{R,P} = \mathbf{J}_R \cdot \hat{\mathbf{P}} = \mathbf{J}_0 \cdot \hat{\mathbf{P}} - (\mathbf{R} \times \mathbf{P}) \cdot \hat{\mathbf{P}} = \mathbf{J}_0 \cdot \hat{\mathbf{P}} = J_{0,P}, \quad (1.9)$$

is always independent of the choice of reference point.

Often angular momenta or angular momentum densities are calculated not with respect to a given reference point but with respect to an axis, i.e. a straight line, in the direction of the total momentum  $\mathbf{P}$ . Indeed, substitution of the equation for a point on such an axis,

$$\mathbf{R}(a) = \mathbf{S} + a\hat{\mathbf{P}}, \quad (1.10)$$

into the equation for the angular momentum calculated with respect to an arbitrary point, equation (1.7), gives

$$\begin{aligned} \mathbf{J}_{R(a)} &= \mathbf{J}_0 - (\mathbf{S} + a\hat{\mathbf{P}}) \times \mathbf{P} = \mathbf{J}_0 - \mathbf{S} \times \mathbf{P} + a\hat{\mathbf{P}} \times \mathbf{P} \\ &= \mathbf{J}_0 - \mathbf{S} \times \mathbf{P}, \end{aligned} \quad (1.11)$$

so the angular momentum as calculated with respect to any point on the axis takes the same value. It is therefore justified to specify an axis as the reference in the calculation of angular momentum.

Please note that non-zero angular momentum densities are always dependent on the choice of reference point. In this thesis angular momentum densities of light beams are, unless otherwise stated, calculated with respect to the optic axis.

### 1.2.3 Conservation of angular momentum

In a straightforward calculation it is possible to show that the angular momentum of a closed system, i.e. a system on which no external forces are acting, is conserved [4].

The Lagrangian formulation of mechanics can, in a very elegant fashion, yield a more general result. If the Lagrangian  $\mathcal{L}$ , the difference between the kinetic and potential energies written as a function of the generalised coordinates  $q_i$  and the corresponding velocities  $\dot{q}_i$ , of a system does not explicitly depend on a generalised coordinate  $q_j$ , then the corresponding generalised momentum  $\partial\mathcal{L}/\partial\dot{q}_j$  is conserved [5]. Independence of the Lagrangian from a generalised coordinate is another way of saying that the Lagrangian has a symmetry under displacement along that coordinate [6]. Examples of generalised momenta are energy, which can be considered formally to be the generalised momentum corresponding to time,  $t$ , momentum, which corresponds to the Cartesian coordinates  $x, y, z$ , and angular momentum [5]. Angular momentum is the generalised momentum corresponding to the generalised coordinate describing the rotation angle of the system about a given axis. As the kinetic energy is independent of the orientation of the system, a component of the angular momentum of the system is conserved whenever rotation of the system about an axis leaves the potential energy of the system unchanged. For example, the potential energy of the Earth on its orbit around the Sun does not change when the position of the Earth is rotated around the Sun; consequently the angular momentum associated with the Earth orbiting the Sun is conserved. More generally, the angular momentum of any system in an isotropic environment is conserved.

## 1.3 Angular momentum in quantum mechanics

### 1.3.1 Angular momentum operators and rotations

The strong relationship between energy, momentum, and angular momentum on the one hand and displacements in time and space and rotations in space on the other that was found in mechanics is further underpinned by the properties of the quantum-mechanical operators for energy (the Hamiltonian operator), momentum and angular momentum. Consider the operator

$$\exp\left(\frac{-i\hat{M}_\alpha\Delta\alpha}{\hbar}\right), \quad (1.12)$$

which is constructed around variable  $\Delta\alpha$ , which has the same dimension as the (arbitrary) parameter  $\alpha$ , and the operator for the corresponding momentum,

$\hat{M}_\alpha$ . Now let  $\Delta\alpha = \Delta t$ , a displacement in time, and  $\hat{M}_\alpha = \hat{H}$ , the Hamiltonian operator. It can be shown [6]<sup>1</sup> that the operator constructed according to the recipe (1.12) from the Hamiltonian operator  $\hat{H}$  displaces functions in time by an amount  $\Delta t$ , i.e.

$$\exp\left(\frac{-i\hat{H}\Delta t}{\hbar}\right)|\psi(t)\rangle = |\psi(t + \Delta t)\rangle \quad (1.13)$$

(this is the so-called time-evolution operator). Similarly, the operator constructed from any Cartesian coordinate,  $\Delta\alpha = \Delta x_j$ , and the corresponding component of the momentum operator,  $\hat{M}_\alpha = \hat{p}_j$ , translates functions it acts upon by  $\Delta x_j$  in the  $x_j$  direction. The operators  $\hat{H}$  and  $\hat{\mathbf{p}}$  are known as the generators of time displacements and translations, respectively.

In analogy to the cases of energy and momentum the angular momentum operator  $\hat{\mathbf{J}}$  is the generator of rotations. The operator

$$\exp\left(\frac{-i\hat{J}_z\Delta\phi}{\hbar}\right), \quad (1.14)$$

for example, has to rotate the functions it acts upon through an angle  $\Delta\phi$  about the  $z$  axis. From the requirement that the operators for the components of the angular momentum are the generators of rotations and the properties of rotations in three dimensions it is possible to derive a set of equations for the components of the angular momentum operator  $\hat{\mathbf{J}}$ . These so-called *fundamental commutation relations of angular momentum* read

$$[\hat{J}_x, \hat{J}_y] = i\hbar\hat{J}_z, \quad [\hat{J}_y, \hat{J}_z] = i\hbar\hat{J}_x, \quad [\hat{J}_z, \hat{J}_x] = i\hbar\hat{J}_y. \quad (1.15)$$

### 1.3.2 Spin and orbital angular momentum

At this point it is instructive to study the simultaneous eigenfunctions of the operator for one of the components of the angular momentum, usually  $\hat{J}_z$ , and the operator corresponding to the square of the magnitude of  $\mathbf{J}$ ,

$$j^2 = j_x^2 + j_y^2 + j_z^2. \quad (1.16)$$

---

<sup>1</sup>This review of important concepts concerning the angular momentum in quantum mechanics is based on the discussion of angular momentum in reference [6], which will not be cited in the remainder of this section.

Those eigenfunctions are denoted  $|j, j_z\rangle$ . It can be shown that the corresponding eigenvalues of  $\hat{J}^2$  are of the form

$$\hbar^2 j(j+1), \quad j \in \{0, 1/2, 1, 3/2, 2, \dots\}, \quad (1.17)$$

and that the corresponding eigenvalues of  $\hat{J}_z$  can be in the range

$$\hbar j_z, \quad j_z \in \{-j, -j+1, \dots, j-1, j\}. \quad (1.18)$$

The fundamental commutation relations of angular momentum, equations (1.15), provide an abstract description of the properties of angular momentum operators. An actual candidate for an angular momentum operator can be constructed by following the standard recipe for ‘guessing’ the quantum-mechanical operator corresponding to a classical observable, which involves the replacement of all observables in the expression for the observable by their corresponding quantum-mechanical operators. The expression for the angular momentum of a single particle, equation (1.2), contains the momentum vector  $\mathbf{p}$ . Replacement by the corresponding operator yields the orbital angular momentum operator

$$\hat{\mathbf{L}} = \mathbf{r} \times \frac{\hbar}{i} \nabla. \quad (1.19)$$

The Cartesian components of  $\hat{\mathbf{L}}$  indeed satisfy the fundamental commutation relations of angular momentum, equations (1.15). Direct calculation of the eigenvalues corresponding to simultaneous eigenfunctions of  $\hat{L}_z$  and  $\hat{L}^2 = \hat{L}_x^2 + \hat{L}_y^2 + \hat{L}_z^2$  reveals that the possible eigenvalues of  $\hat{L}^2$  are

$$\hbar^2 l(l+1), \quad l \in \{0, 1, 2, \dots\}; \quad (1.20)$$

possible corresponding eigenvalues of  $\hat{L}_z$  are

$$\hbar l_z, \quad l_z \in \{-l, -l+1, \dots, l-1, l\}. \quad (1.21)$$

The restriction in the possible eigenvalues of the operator for the square of the magnitude of the orbital angular momentum,  $\hat{L}^2$ , to integers is due to the fact that the ‘normal’ part of the wave function, which also describes the orbital angular momentum, is single-valued.

Experiments have demonstrated that in addition to orbital angular momentum another type of angular momentum exists: *intrinsic* or *spin* angular momentum. The operator for the square of the magnitude of the spin,  $\hat{S}^2$ , has

eigenvalues

$$\hbar^2 s(s+1), \quad s \in \{0, 1/2, 1, 3/2, \dots\}. \quad (1.22)$$

Different values of  $s$  correspond to different types of particles: in electrons, for example,  $s = 1/2$ ; electrons are therefore said to be spin-1/2 particles. As before, the eigenvalues for the Cartesian components of  $\hat{\mathbf{s}}$ , for example  $\hat{s}_z$ , take on the values

$$\hbar s_z, \quad s_z \in \{-s, -s+1, \dots, s-1, s\}. \quad (1.23)$$

## 1.4 Angular momentum of light

### 1.4.1 Milestones in the history of the angular momentum of light

In 1909 Poynting [1] concluded that circularly polarised light passing through a wave plate should exert a torque on it. He suggested that this is due to a non-zero angular momentum component in the direction of propagation contained in the light beam. The usual choice of the orientation of the frame of reference, which is also adopted in this thesis, is that the light beam travels in the positive  $z$  direction.

Nowadays, the part of the angular momentum of light that is associated with its polarisation state is called spin. Mathematically, photons are spin-1 particles [7], i.e. the quantum number describing the square of the magnitude of the spin, equation (1.22), takes on the value  $s = 1$ .

The reason for the special role of the spin component in the direction of propagation can perhaps be found in the fact that only the component of the corresponding spin operator along the propagation axis “is a true spin angular momentum operator, since only this component generates spin rotations” [7]. It is perhaps also helpful to note that there exists no frame of reference in which the total momentum of a light beam would be zero. According to section 1.2, this implies that only the angular momentum component along the propagation axis is independent of the choice of reference point.

The first experimental measurement of this spin component along the propagation direction was performed in 1935 by Beth [8, 9]. In his experiment a

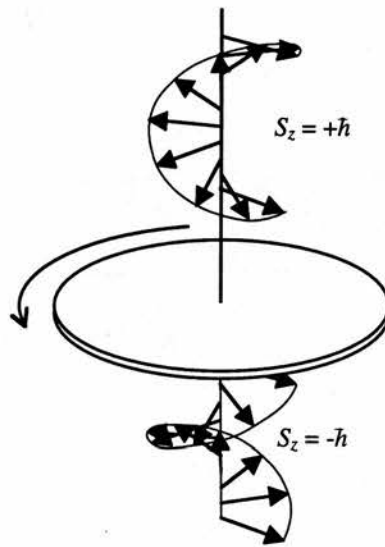


Figure 1.2: Schematic of Beth's experiment for the measurement of the mechanical torque exerted by a circularly polarised light beam on a half-wave plate. The torque is due to an exchange of angular momentum between the wave plate and the light beam, whose spin component changes sign on passing through the wave plate.

half-wave plate, suspended like a torsion pendulum, reversed the handedness of the polarisation of incoming light (fig. 1.2). Conservation of angular momentum implies that due to the concomitant reversal of the spin of the beam a torque acted on the wave plate, causing slight rotation. Beth's results were subsequently confirmed in a number of independent experiments [10, 11].

In 1979, Vaughan and Willetts [12] were the first to contrast "circularly polarised light which may be described as plane phased and helically polarised" with a "linearly polarised, helically phased, beam" (fig. 1.3). Thirteen years later, Allen and co-workers [2] identified the correspondence of these two cases to eigenfunctions of spin and orbital angular momentum, respectively. They attributed an orbital angular momentum of  $l\hbar$  per photon to Laguerre-Gaussian modes (section 1.4.2) with an azimuthal mode index  $l$ , which are indeed "helically phased" (fig. 1.5).

That the angular momentum of light beams can be specified "per photon" is due to the proportionality of the angular momentum density and the energy density in light beams [2]. In monochromatic light beams of frequency  $\nu$ , the energy density can be expressed as the energy per photon,  $h\nu$ , times the photon density. Division of the angular momentum density by the photon density then yields the angular momentum per photon.

Apart from identifying the orbital angular momentum in Laguerre-Gaussian modes, Allen *et al.* also proposed a way of measuring it [2]. In analogy to Beth's experiment, the proposed experiment reverses the handedness of the phase fronts by passing the beam through a cylindrical-lens  $\pi$  mode converter [13]. In this process, twice the orbital angular momentum originally contained within the beam is transferred to the mode converter, which therefore experiences a torque (fig. 1.4).

To date, this proposed experiment has not been performed. In particular the alignment of the beam with respect to the mode converter proved to be too difficult: if the beam hits the mode converter off-centre or skew, then, either in this position of the mode converter or after it has rotated due to the torque, the direction of the axis of the beam after the mode converter is changed. The beam gains a momentum component normal to the original direction of propagation which is mirrored by an equal and opposite momentum transferred off-centre

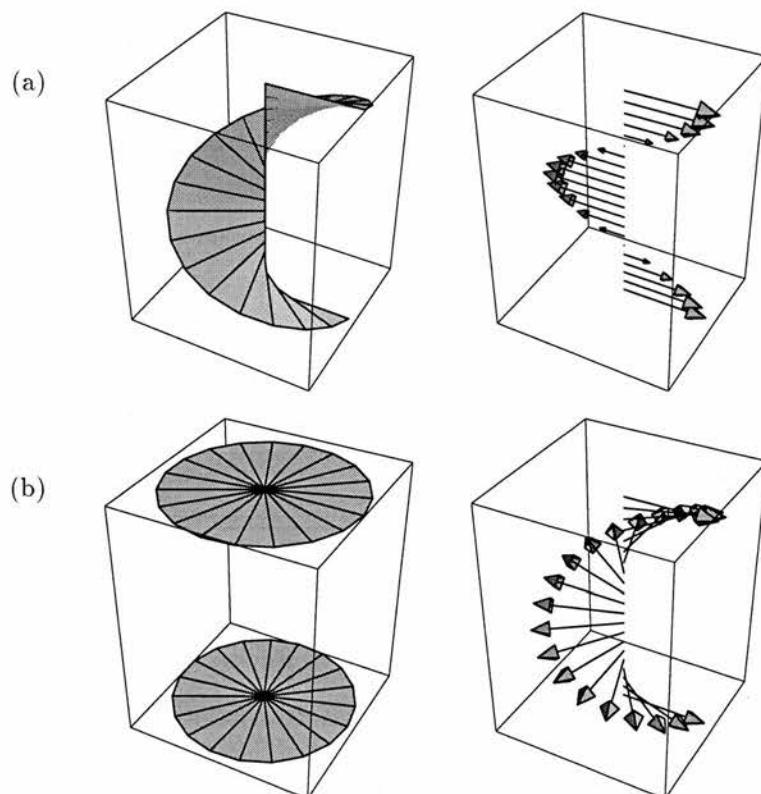


Figure 1.3: Comparison of (a) “linearly polarised, helically phased” and (b) “plane phased and helically polarised” light, following ref. [12]. The graphs on the left are plots of phase fronts, the graphs on the right show the direction of the electric field as a function of the displacement in the direction of propagation. All graphs are for beams propagating in the vertical direction. The displayed vertical range corresponds to one wavelength of the beam.

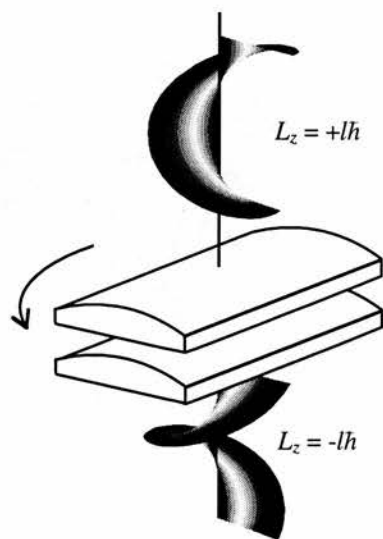


Figure 1.4: Schematic of a proposed experiment for the measurement of the mechanical torque exerted by a light beam with orbital angular momentum, as suggested in ref. [2]. In analogy to Beth's experiment (fig. 1.2), this experiment uses a cylindrical-lens mode converter to reverse the sign of the orbital angular momentum in the beam, causing rotation of the mode converter.

to the mode converter. This results in a large unwanted torque on the mode converter [14].

An alternative demonstration of the orbital angular momentum contained within a light beam with helical phase fronts was performed in 1995 by He *et al.* [15]. In this experiment, partial absorption of a light beam by a microscopic particle provided the mechanism for transferring the *total* angular momentum from the beam to the particle, which rotated under illumination. Shortly afterwards, quantitative measurements were performed in similar experimental setups by comparing the rotation due to spin with that due to orbital angular momentum [16, 17].

### 1.4.2 Laguerre-Gaussian (LG) modes

Laguerre-Gaussian (LG) modes play an important role in the field of orbital angular momentum of light. Because of their azimuthal phase structure of the form  $l\phi$ , which corresponds to helical phase fronts (figures 1.5 and 1.6), Laguerre-Gaussian modes are eigenfunctions of the quantum-mechanical orbital angular momentum operator  $\hat{L}_z = \frac{\hbar}{i} \frac{\partial}{\partial \phi}$  [2]. The corresponding eigenvalues of  $l\hbar$  are the orbital angular momentum content per photon. The number  $l$  is used to describe Laguerre-Gaussian modes and referred to as the azimuthal mode index.

In most calculations that involve the orbital angular momentum of light, the simplest case involves a pure eigenmode of the orbital angular momentum operator. Because LG modes form a complete orthogonal basis set [18], like the better-known Hermite-Gaussian (HG) modes, the analysis in terms of LG modes can be easily generalised to arbitrary light beams<sup>2</sup>. Section 6.3 is an example of this type of analysis.

Laguerre-Gaussian modes are structurally invariant, i.e. apart from a change in size their cross-sections remain unchanged on propagation. LG intensity cross-sections consist of  $p + 1$  concentric rings, whereby the innermost ring is

<sup>2</sup>The family of Bessel beams [19, 20] seems to be another complete orthogonal set of orbital angular momentum eigenmodes. As such, however, they are less popular than the Laguerre-Gaussian modes; in fact, the author is unaware of any uses of Bessel beams as a complete set of orbital angular momentum eigenfunctions in the literature.

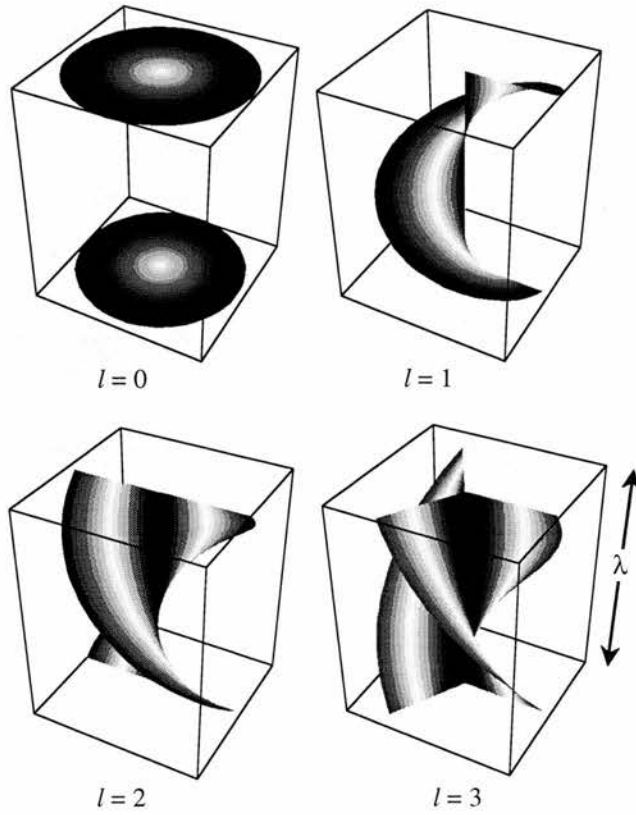


Figure 1.5: Phase fronts of collimated Laguerre-Gaussian modes, with the radial intensity structure for  $p = 0$  superimposed. Together with the phase term  $\exp(ikz)$ , the azimuthal phase term of the form  $\exp(-il\phi)$  gives rise to helical phase fronts. The azimuthal mode index  $l$  determines the number of intertwined helices that the phase front comprises. Please note that the well-known *fusilli* (fig. 1.6) provide an excellent model of the phase fronts in a collimated  $\text{LG}_0^3$  mode.

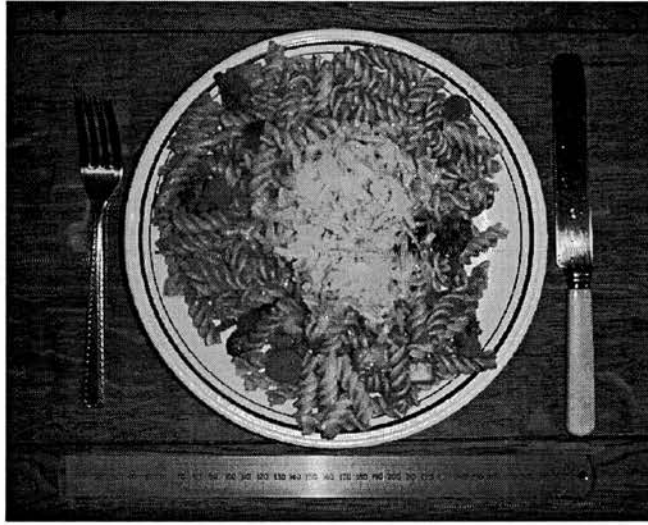


Figure 1.6: *Fusilli*, commonly known as *pasta spirals* or *pasta twists*, provide an excellent model of the phase fronts in a collimated Laguerre-Gaussian mode. Usually *fusilli* comprise *three* intertwined helices, and hence correspond to an azimuthal mode index  $l = 3$ .

filled-in if the azimuthal mode index  $l = 0$  (fig. 1.7).  $p$  is called the radial mode index. LG modes are often denoted  $\text{LG}_p^l$ .

The mode function<sup>3</sup> corresponding to a LG mode with indices  $l$  and  $p$  with its beam waist in the plane  $z = 0$  is [18]

$$\begin{aligned} e_{\text{LG}_p^l}(r, \phi, z) &= C \frac{1}{w(z)} \left( \frac{r\sqrt{2}}{w(z)} \right)^{|l|} L_p^{|l|} \left( \frac{2r^2}{w^2(z)} \right) \exp\left( \frac{-r^2}{w^2(z)} \right) \\ &\quad \times \exp\left( \frac{-ikr^2 z}{2(z^2 + z_R^2)} \right) \exp(-il\phi) \exp(-ikz) \end{aligned}$$

<sup>3</sup>The (physical) electric and magnetic field,  $\mathbf{E}$  and  $\mathbf{B}$ , can be described in terms of one (complex) electric field,  $\mathbf{e}$ :

$$\mathbf{E}(\mathbf{r}, t) = (\mathbf{e}(\mathbf{r}) \exp(-i\omega t) + \text{c.c.})/2 \quad (1.24)$$

$$\mathbf{B}(\mathbf{r}, t) = (\mathbf{b}(\mathbf{r}) \exp(-i\omega t) + \text{c.c.})/2 \quad (1.25)$$

where

$$\mathbf{b}(\mathbf{r}) = \frac{1}{i\omega} \nabla \times \mathbf{e}(\mathbf{r}). \quad (1.26)$$

In a polarised light beam propagating in the  $z$  direction, the  $x$  and  $y$  components of  $\mathbf{e}$  are proportional to each other, and therefore both can be written as proportional to a scalar field  $e_{xy}(\mathbf{r})$ . In the case of laser modes this scalar field is referred to as the *mode function*.

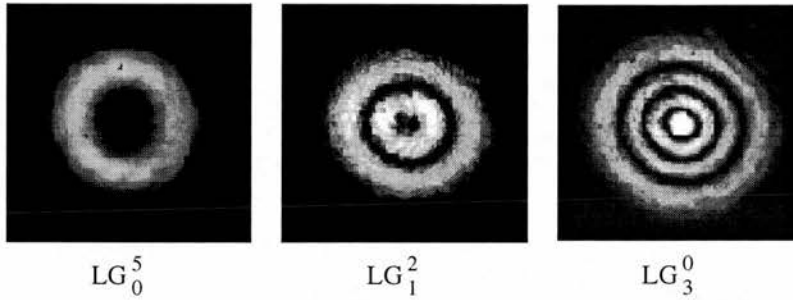


Figure 1.7: Experimental intensity cross-sections of some Laguerre-Gaussian modes  $LG_p^l$ .  $p + 1$  is the number of rings in the intensity profile. If  $l = 0$ , the innermost ring is a filled-in disc.

$$\times \exp\left(i(2p + |l| + 1) \arctan\left(\frac{z}{z_R}\right)\right). \quad (1.27)$$

In this equation,  $C$  is a normalisation constant,  $z_R$  is the Rayleigh range,  $w(z) = w_0 \sqrt{1 + (\lambda z / (\pi w_0^2))^2}$  is the radius at which the Gaussian terms falls to  $1/e$  of its on-axis value, and  $w_0 = w(0)$  is called the beam waist.  $L_p^l$  is an associated Laguerre polynomial.

The reason for the popularity of Laguerre-Gaussian modes is probably not merely to be found in their significance as orbital angular momentum eigenfunctions, but also in the relative simplicity with which they can be generated. Pure Laguerre-Gaussian modes can, for example, be generated either directly in a special laser cavity [21, 22] or, with perhaps less difficulty, from lasers that emit the standard Hermite-Gaussian laser modes. The cylindrical-lens mode converter [13] (fig. 1.8) can convert higher-order Hermite-Gaussian modes into corresponding pure Laguerre-Gaussian modes. The conversion efficiency of this process is limited only by imperfections in the mode converter and reflection losses [23] (see also chapter 2).

Another technique that claims to generate Laguerre-Gaussian modes, in which a fundamental Gaussian laser beam is shone on a spiral phase plate, either real [24, 25, 26, 27] or in the form of a hologram [28, 29, 30], generates not pure Laguerre-Gaussian modes but superpositions thereof. As all the constituent Laguerre-Gaussian modes have the same azimuthal mode index  $l$ , such superpositions are also orbital angular momentum eigenfunctions and can

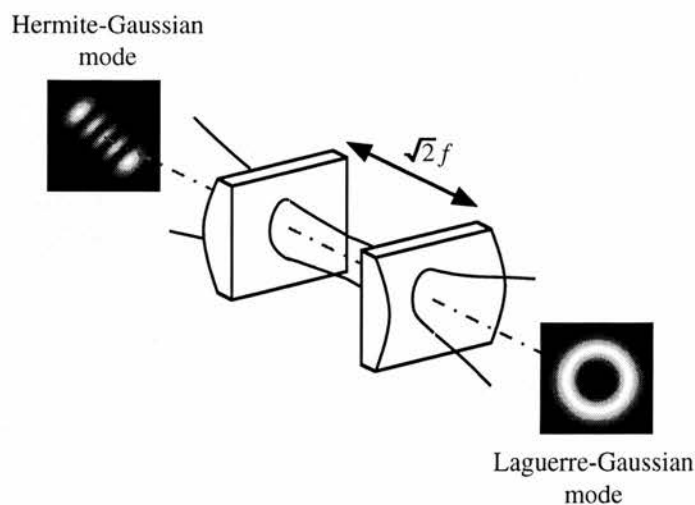


Figure 1.8: Schematic of a cylindrical-lens mode converter and example of calculated beam profiles (see also appendix A). Hermite-Gaussian modes of all orders can be converted into corresponding Laguerre-Gaussian modes, and vice versa. Both the input and output modes have their beam waist positioned in the plane half way between the two cylindrical lenses of focal length  $f$ , with a beam waist size of  $w_0 = \sqrt{(1 + 1/\sqrt{2})f\lambda/\pi}$ .

as such be used in experiments directly, for example in experiments involving the transfer of the orbital angular momentum to small particles [15, 31] and in non-linear interactions [32, 33]. Alternatively superpositions of LG modes with different  $p$  indices can be turned into pure LG modes through “filtering” in a separate cavity [34].

## Chapter 2

# Misaligned cylindrical-lens mode converters

### 2.1 Introduction

The cylindrical-lens mode converter [13] (fig. 2.1; see also section 1.4.2) is based on a pair of cylindrical lenses and converts Hermite-Gaussian modes of all orders into corresponding Laguerre-Gaussian modes. Unlike the spiral phase plate and the holographic converter, this method can, in principle, produce pure Laguerre-Gaussian modes. In this chapter the performance of the cylindrical-lens mode converter is studied for various imperfections in the assembly or use of the mode converter.

To convert a pure Hermite-Gaussian mode into a pure Laguerre-Gaussian mode using a cylindrical-lens mode converter, the focal length of the cylindrical lenses has to be related to their separation  $d$  by

$$f = d/\sqrt{2}. \quad (2.1)$$

The input beam has to be focused to the mid-point of the lenses with a beam waist of

$$w_0 = \sqrt{(1 + 1/\sqrt{2})f\lambda/\pi}. \quad (2.2)$$

In principle, any Hermite-Gaussian mode with indices  $m$  and  $n$  (denoted as  $\text{HG}_{m,n}$ ), aligned at  $45^\circ$  to the principal axis of the lens, will then be converted

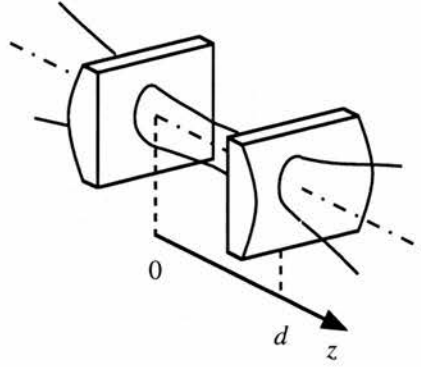


Figure 2.1: Cylindrical lens mode converter for converting between Laguerre-Gaussian and Hermite-Gaussian modes. The separation of the two cylindrical lenses, both of focal length  $f$ , is  $d = \sqrt{2}f$ . Both the input and output modes have a beam waist  $w_0 = \sqrt{(1 + 1/\sqrt{2})f\lambda/\pi}$ .

into a Laguerre-Gaussian mode with mode indices [31]

$$l = m - n, \quad p = \min(m, n) \quad (2.3)$$

and with the same beam waist. For example, a  $\text{HG}_{1,0}$  mode, aligned at  $45^\circ$  to the axes of the lenses, can be expressed as two, in-phase,  $\text{HG}_{1,0}$  and  $\text{HG}_{0,1}$  modes aligned with the principal axes of the lenses. The separation of the cylindrical lenses is made such that these two orthogonal modes undergo Gouy phase shifts that differ by  $90^\circ$ . After the lenses, their superposition is a Laguerre-Gaussian mode with  $l = 1$  and  $p = 0$  (denoted as  $\text{LG}_p^l$ ).

## 2.2 Modelling of the mode spectrum of a misaligned mode converter

The program described in appendix A has been used to model light passing through the mode converter. Figure 2.2 shows intensity cross-sections through the beam between the lenses of a mode converter for an incoming  $\text{LG}_1^3$  mode. A decomposition of the numerically calculated output beam shows that over 99.9% of the transmitted beam resides in a Hermite-Gaussian  $\text{HG}_{4,1}$  mode. This result, which is close to the theoretical conversion efficiency of 100%, demonstrates the

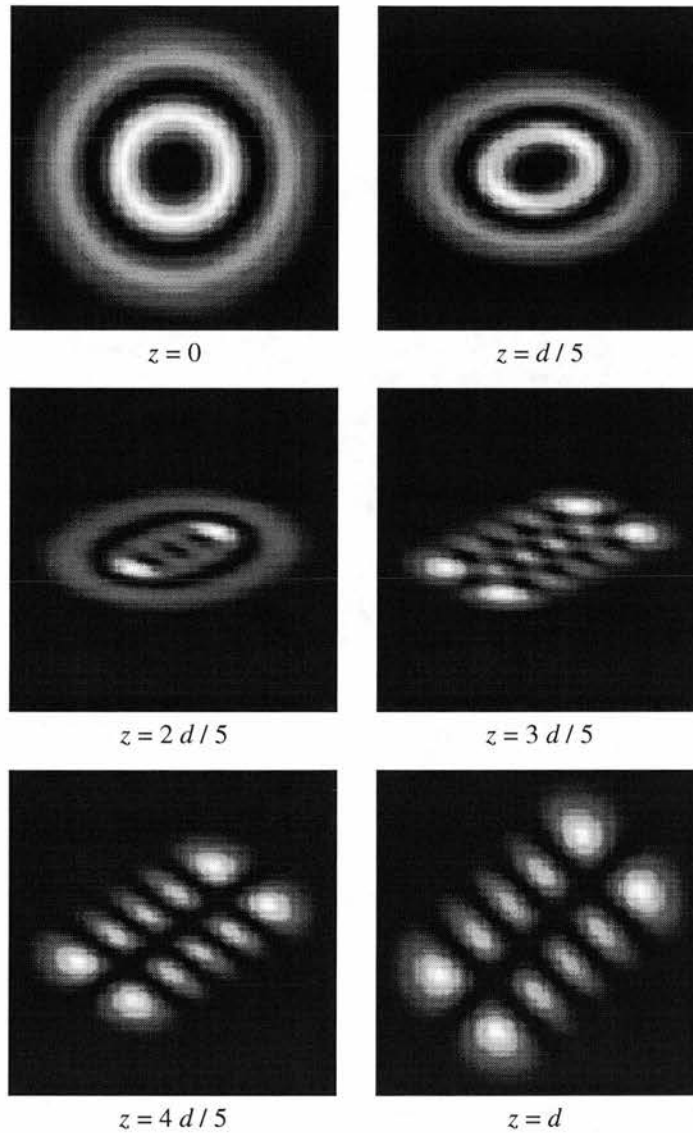


Figure 2.2: Modelled intensity distributions in various planes between the two cylindrical lenses of a (perfectly aligned) cylindrical-lens mode converter (figure 2.1). The incoming Laguerre-Gaussian mode with indices  $l = 3$  and  $p = 1$  is converted into a Hermite-Gaussian mode with indices  $m = 4$  and  $n = 1$ .  $z$  is the distance after the first cylindrical lens,  $d$  is the separation of the cylindrical lenses.

efficiency of the numerical model. Incorporation of the spherical aberration of the cylindrical lenses into the model does not significantly alter the fraction of the power that resides within the  $\text{HG}_{4,1}$  mode - not surprisingly, as the cylindrical lenses are being used at extremely low aperture corresponding to an  $F$  number of approximately  $f/200$ .

An ideal cylindrical lens mode converter can produce Laguerre-Gaussian modes with 100% efficiency. However, a question remains as to how this figure is compromised by manufacturing limitations of the cylindrical lenses and by incorrect mode matching. To address this point the performance of the mode converter for input modes  $\text{HG}_{4,0}$  and  $\text{HG}_{2,1}$  to produce  $\text{LG}_0^4$  and  $\text{LG}_1^1$  Laguerre-Gaussian modes, respectively, has been modelled. The mode converter in the model is based on cylindrical lenses with focal lengths of  $f_{\text{ideal}} = 50\text{mm}$ , the wavelength of  $633\text{nm}$  requires an input beam waist of  $w_{\text{ideal}} = 130\mu\text{m}$ .

Figures 2.3 and 2.5 show the calculated mode decomposition for errors in the focal lengths of the cylindrical lenses of up to  $\pm 20\%$ , which should be compared to a typical manufacturing tolerance of  $\pm 5\%$ . Figures 2.4 and 2.6 show the calculated mode decomposition for errors in mode matching of the input mode, i.e. incorrect focusing of the input beam. For errors of  $\pm 5\%$  in either focal length or beam focusing the mode composition shows that over 97% of the energy is contained in the principal mode.

Superpositions of Laguerre-Gaussian modes with a range of mode indices need not necessarily be structurally stable, so the beam profile changes form upon propagation [35]. As an example a  $\text{HG}_{2,0}$  mode incident on a mode converter with a 10% error in the focal length of the cylindrical lenses was modelled. The intensity distribution of the generated beam in several planes after the mode converter and subsequent focussing lens is shown in figure 2.7. After a propagation distance of only 20mm the two screw-phase dislocations within the nominal  $l = 2$  Laguerre-Gaussian mode are clearly separated (compare also figures A.2 and A.3 in appendix A). It can also be seen that this separation is maintained when the beam is subsequently refocussed. Dislocation splittings of this kind are problematic in areas where a single intensity minimum is required. Such areas include the use of Laguerre-Gaussian modes in optical tweezers [36], optical spanners [17], and atom guiding [37]. Similar behaviour involving the

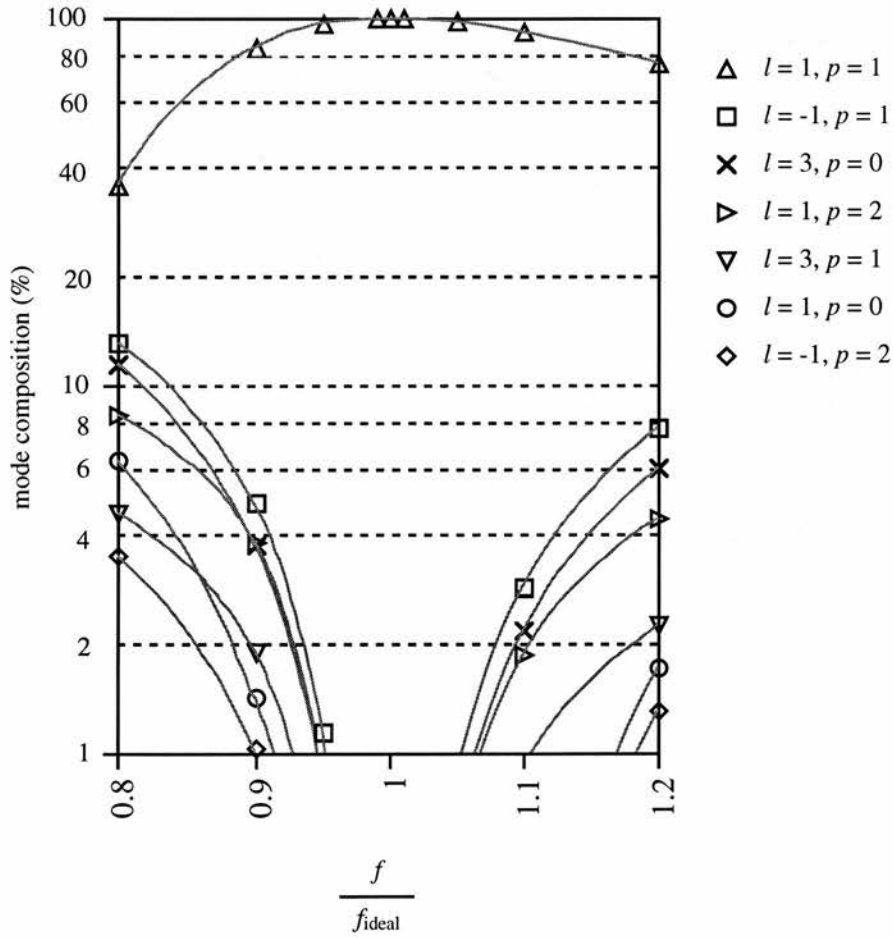


Figure 2.3: Output beam composition in terms of Laguerre-Gaussian modes for an input Hermite-Gaussian  $HG_{2,1}$  mode as a function of the focal length,  $f$ , of the cylindrical lenses that make up the mode converter.

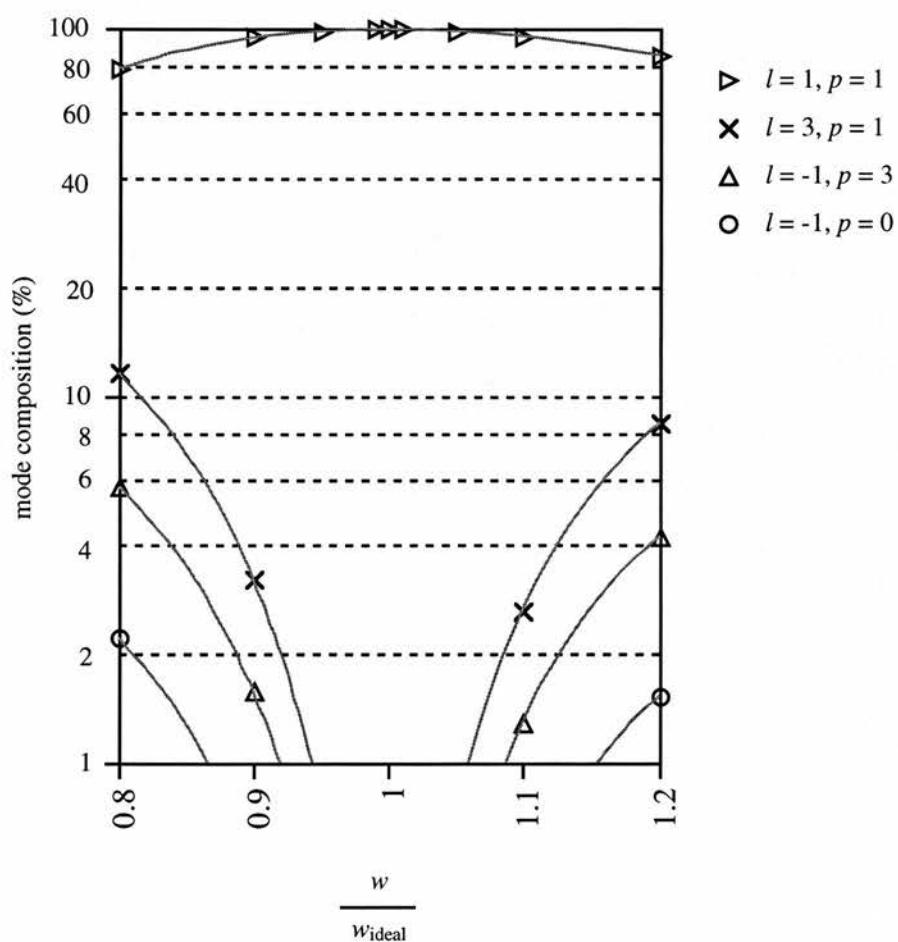


Figure 2.4: Output beam composition in terms of Laguerre-Gaussian modes for an input Hermite-Gaussian  $HG_{2,1}$  mode with a beam waist  $w$ .

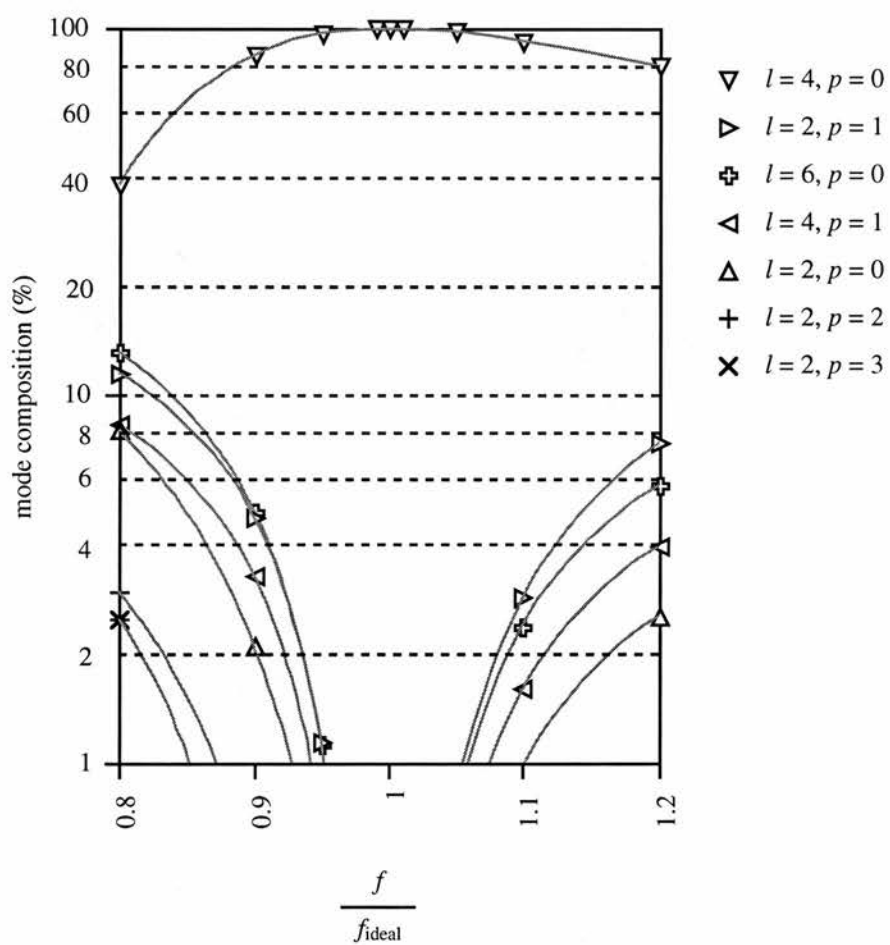


Figure 2.5: Output beam composition in terms of Laguerre-Gaussian modes for an input Hermite-Gaussian  $HG_{4,0}$  mode as a function of the focal length,  $f$ , of the cylindrical lenses that make up the mode converter.

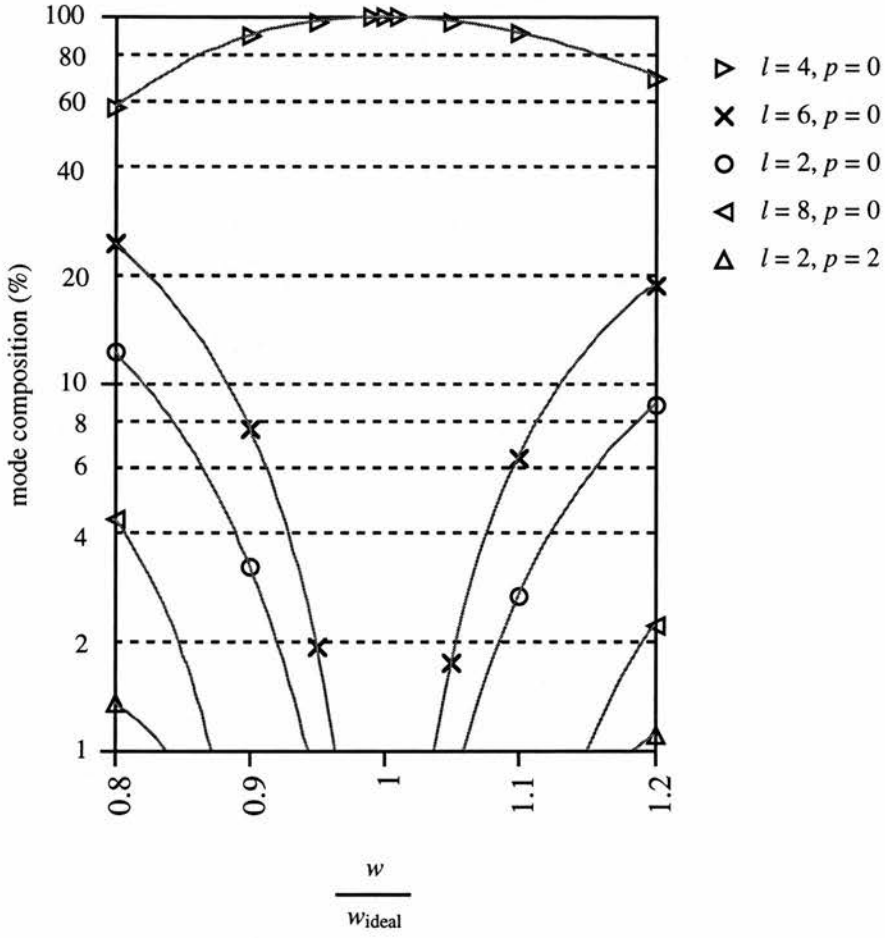


Figure 2.6: Output beam composition in terms of Laguerre-Gaussian modes for an input Hermite-Gaussian  $HG_{4,0}$  mode with a beam waist  $w$ .

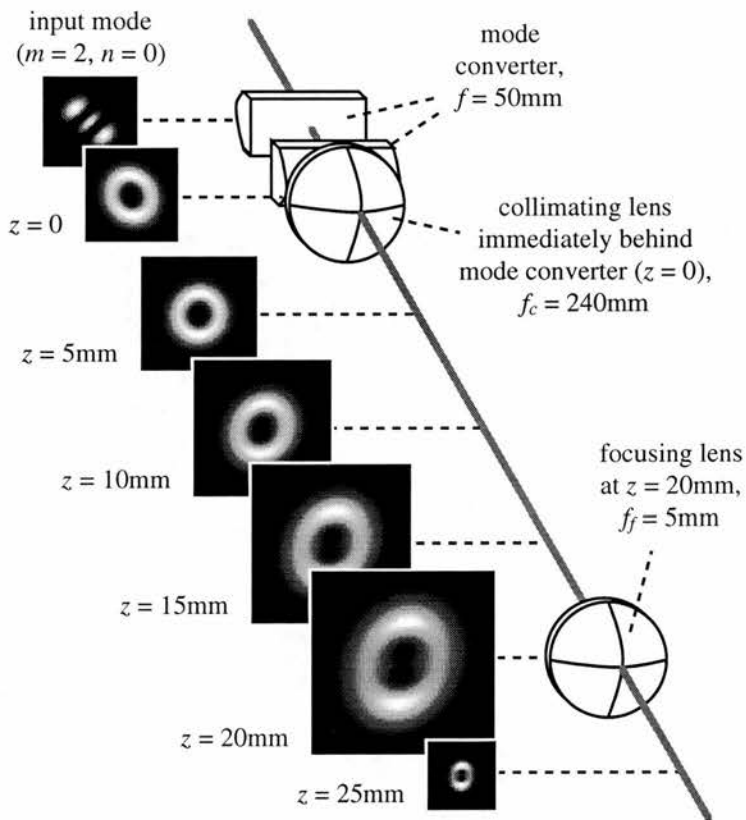


Figure 2.7: Propagation of the beam produced from an input  $\text{HG}_{2,0}$  mode by a poorly specified mode converter. Note the formation of a double intensity null.

splitting and combination of screw phase dislocations has been reported earlier [38].

The work described in this chapter has been published in ref. [23].

## Chapter 3

# Propeller beams

### 3.1 Introduction

“Elliptical Gaussian light beams with general astigmatism” have been studied 30 years ago [39]. Such a beam results from the passage of an elliptical Gaussian beam through a cylindrical lens, which can be rotated about the optical axis with respect to the direction of the elliptical cross-section of the light beam.

In this chapter it is shown that such beam possess orbital angular momentum. The mechanism by which the angular momentum is transferred to the beam is the same as in the cylindrical-lens converter [13] for converting Hermite-Gaussian modes into Laguerre-Gaussian modes. An analysis of the shape of the phase fronts suggests the “nickname” *propeller beams* for elliptical Gaussian beams with general astigmatism.

### 3.2 Orbital angular momentum content of propeller beams

When a light beam, propagating in the  $z$  direction, is passed through a thin lens it acquires an additional phase factor  $\Phi_{\text{lens}}(x, y)$ . The cross-section of the complex electric field, as defined in equation (1.24), immediately behind the lens,  $e'(x, y)$ , is given in terms of the complex electric field immediately in front

of the lens,  $e(x, y)$ , by

$$e'(x, y) = e(x, y) \exp(i\Phi_{\text{lens}}(x, y)). \quad (3.1)$$

The associated change in the  $z$  component of the orbital angular momentum per unit length in the  $z$  direction,  $L_z$ , for monochromatic light of frequency  $\omega$  is given by [40]

$$L_z = -\frac{\epsilon_0}{2\omega} \iint \left( x \frac{\partial \Phi_{\text{lens}}}{\partial y} - y \frac{\partial \Phi_{\text{lens}}}{\partial x} \right) |e(x, y)|^2 dx dy. \quad (3.2)$$

For a cylindrical lens of focal length  $f$ , inserted at an angle to the  $x$ -axis, the phase factor introduced for light of wave number  $k$  is given by

$$\begin{aligned} \Phi_{\text{lens}}(x, y) &= -\frac{k}{2f} (x \sin \alpha + y \cos \alpha)^2 \\ &= -\frac{k}{2f} (x^2 \sin^2 \alpha + y^2 \cos^2 \alpha + 2xy \sin \alpha \cos \alpha), \end{aligned} \quad (3.3)$$

so that

$$L_z = \frac{\epsilon_0 k}{4\omega f} \iint ((x^2 - y^2) \sin 2\alpha + 2xy \cos 2\alpha) |e(x, y)|^2 dx dy. \quad (3.4)$$

If the intensity cross section  $|e(x, y)|^2$  of the light field falling onto the lens is symmetric about the  $x$  and  $y$  axes, then by symmetry the term  $2xy \cos 2\alpha$  integrates to zero and the expression for  $L_z$  simplifies to

$$L_z = \frac{\epsilon_0 k}{4\omega f} \iint ((x^2 - y^2) \sin 2\alpha) |e(x, y)|^2 dx dy. \quad (3.5)$$

The axes can always be chosen such that this is the case for Hermite-Gaussian modes of any order and elliptical Gaussian beams.

An elliptical Gaussian beam aligned with the  $x$  and  $y$  axes has an intensity distribution that can be written as

$$|e(x, y)|^2 \propto \frac{2}{\pi} \frac{1}{w_x w_y} \exp\left(-\frac{2x^2}{w_x^2}\right) \exp\left(-\frac{2y^2}{w_y^2}\right), \quad (3.6)$$

where  $w_x$  and  $w_y$  are the distances at which the Gaussian term drops to  $1/e$  of its on axis value in the  $x$  and  $y$  directions, respectively. It is straightforward to show for such a beam that the ratio of the change in orbital angular momentum per unit length on passing through a cylindrical lens aligned at an angle  $\alpha$  to the  $x$ -axis and the energy per unit length in the beam,  $U = (\epsilon_0/2) \iint |e|^2 dx dy$ , is given by

$$\frac{L_z}{U} = \frac{w_x^2 - w_y^2}{8cf} \sin(2\alpha). \quad (3.7)$$

This implies that the corresponding change in orbital angular momentum *per photon*,  $\delta L_z$ , is

$$\delta L_z = \frac{k}{8f} (w_x^2 - w_y^2) \sin(2\alpha) \hbar. \quad (3.8)$$

For highly elliptical beams a few millimetres in size, at optical wavelengths, this can easily exceed  $1,000\hbar$  per photon. Only the  $F$  number and aperture of the cylindrical lens limits the amount of orbital angular momentum that can be transferred.

The orbital angular momentum density in a light beam,  $l_z(x, y, z)$ , is given by [13]

$$l_z(x, y, z) = -\frac{\epsilon_0}{2\omega} \frac{\partial \arg e}{\partial \phi} |e|^2, \quad (3.9)$$

where  $\phi$  is the azimuthal position within the beam. This is, of course, the integrand of the previous expression for  $L_z$ . For a Laguerre-Gaussian mode,  $\arg e$  is simply  $l\phi$ ; therefore the ratio of the orbital angular momentum density,  $l_z(x, y, z)$ , divided by the energy density,  $u(x, y, z) = (\epsilon_0/2)|e|^2$ , in a Laguerre-Gaussian mode is simply

$$\frac{l_z(x, y, z)}{u(x, y, z)} = \frac{l}{\omega} \quad (3.10)$$

and therefore independent of position within the beam.

This is not the case for propeller beams. Looking at the generation of a propeller beam by shining a collimated elliptical Gaussian beam onto a cylindrical lens, the relative phase of the field immediately behind the cylindrical lens is that introduced by the lens and is given by

$$\arg e = \Phi_{\text{lens}}. \quad (3.11)$$

The partial derivative of this phase with respect to the azimuthal angle turns out to be

$$\begin{aligned} \frac{\partial \arg e}{\partial \phi} &= \frac{\partial \Phi_{\text{lens}}}{\partial \phi} = x \frac{\partial \Phi_{\text{lens}}}{\partial y} - y \frac{\partial \Phi_{\text{lens}}}{\partial x} \\ &= -\frac{k}{f} (x \sin \alpha + y \cos \alpha)(x \cos \alpha - y \sin \alpha), \end{aligned} \quad (3.12)$$

and the ratio of the orbital angular momentum density and the energy density is

$$\frac{l_z(x, y, z)}{u(x, y, z)} = \frac{k}{\omega f} (x \sin \alpha + y \cos \alpha)(x \cos \alpha - y \sin \alpha). \quad (3.13)$$

It is helpful to define a new pair of axes,  $x'$  and  $y'$ , which are aligned with the principal axes of the cylindrical lens, such that  $x' = x \cos \alpha - y \sin \alpha$  and  $y' = x \sin \alpha + y \cos \alpha$ . Then

$$\frac{l_z(x, y, z)}{u(x, y, z)} = \frac{kx'y'}{\omega f}. \quad (3.14)$$

It can be seen that in the case of the astigmatically focussed elliptical Gaussian beam, the ratio of orbital angular momentum density and energy density varies across the beam and is zero on the axis. It is worth noting that, unlike Laguerre-Gaussian modes, propeller beams have an on-axis intensity. This does not, however, mean that they possess a non-zero on-axis orbital angular momentum density; according to equation (3.14), the on-axis orbital angular momentum density in propeller beams is zero.

Any beam with a non-circularly symmetric intensity distribution can exchange orbital angular momentum with a cylindrical lens. For example, a high-order Hermite-Gaussian beam with its peak intensity off-axis could be used. The off-axis peak intensity would lead to even greater transfer of orbital angular momentum than for an elliptical Gaussian beam.

### 3.3 Phase structure of propeller beams

The origin of the orbital angular momentum of light beams lies in their azimuthal phase structure [2, 41]. The phase structure of Laguerre-Gaussian modes has been examined experimentally by observing the interference pattern between the Laguerre-Gaussian beam and a plane wave of the same frequency [42]. In this section a similar experiment to observe the phase structure of propeller beams is described<sup>1</sup> and the results interpreted in the context of the orbital angular momentum of the light beam.

The experimental arrangement is detailed in figure 3.1. The output from a polarised He-Ne laser is expanded and coupled into a Mach-Zehnder interferometer. One arm of the interferometer contains a beam telescope adjusted to give a collimated, large diameter beam to act as the phase reference. The other arm contains two cylindrical lenses positioned to produce an elliptical beam

---

<sup>1</sup>In studies of lens aberrations, similar interference patterns have already been observed many decades ago [43, 44].

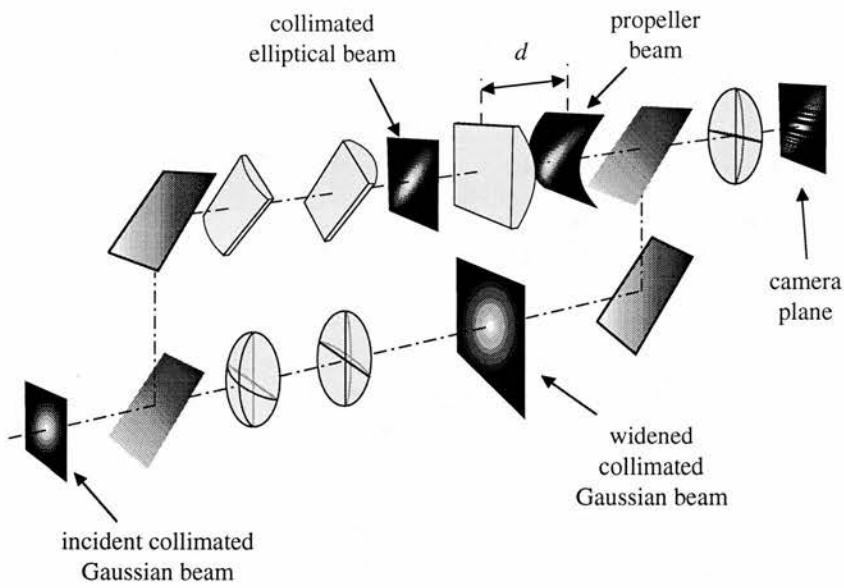


Figure 3.1: Experimental arrangement for examining the phase structure of propeller beams. The cross-section through the propeller beam a distance  $d$  behind the last cylindrical lens in the upper arm of the interferometer is imaged onto the camera, together with a plane reference wave.

with beam waists of approximately 2mm and 0.2mm, coincident with a third cylindrical lens of focal length  $f = 200\text{mm}$ . This third lens is aligned at an angle of  $45^\circ$  with respect to the major axis of the elliptical beam and in our experiment is calculated to impart an orbital angular momentum of approximately  $25\hbar$  per photon to the transmitted beam. Reduction of the focal length of the third lens, and/or increasing the dimensions of the incident beam, causes significantly larger amounts of orbital angular momentum to be transferred to the beam; however, the interference fringes then become too close to be resolved. A plane a distance  $d$  behind the third lens is imaged on a camera which records the interference pattern between the elliptical beam and the collimated reference beam.

Figure 3.2 shows the phase and intensity profile of the elliptical Gaussian beam at various positions behind the third lens. Immediately behind the lens the phase structure of the beam maps out the contour lines of the optical thickness of the lens, and hence straight line interference fringes are observed parallel to its principal axis. In the vicinity of the focal plane, the shape of the fringes is hyperbolic. From these interferograms it is possible to deduce the form of the wave front. Figures 3.3 and 3.4 show schematic representations of the intensity and phase structure and associated orbital momentum density vectors, which result in a non-zero orbital angular momentum in the beam.

The work described in this chapter has been published in ref. [45].

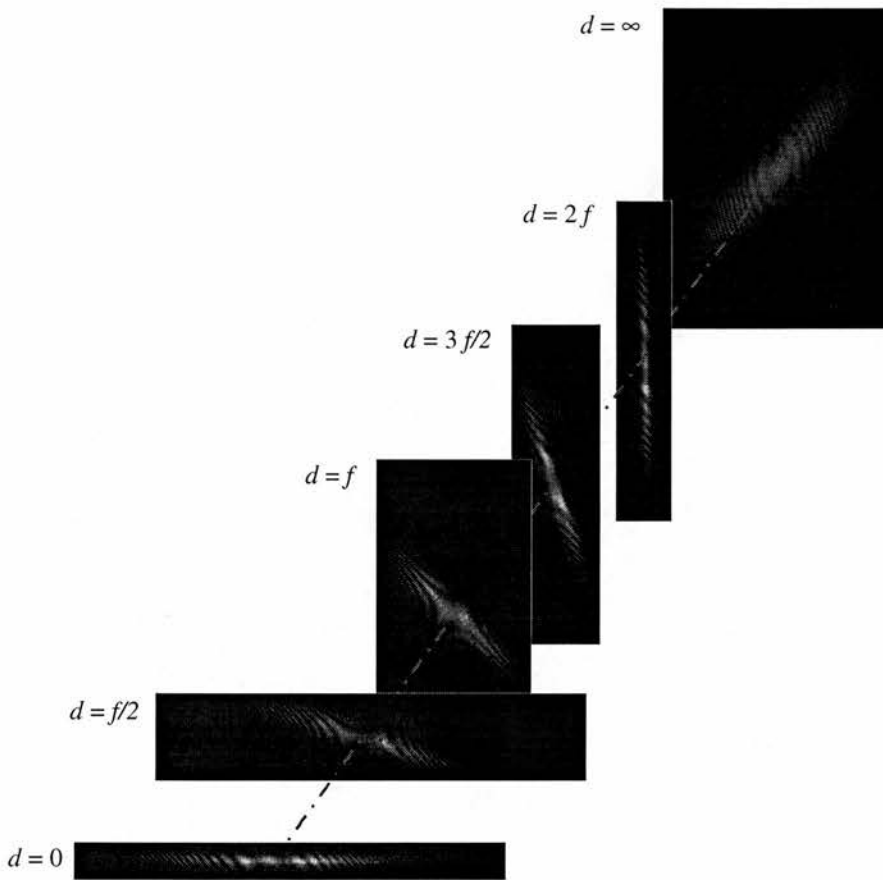


Figure 3.2: Interferograms of a propeller beam and a plane wave.  $d$  is the distance of the propeller beam behind the cylindrical lens of focal length  $f = 200\text{mm}$ .

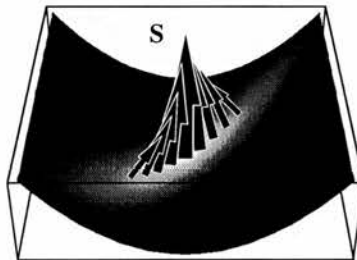


Figure 3.3: Phase front with superimposed intensity distribution of a propeller beam for  $d = 0$ . Orbital angular momentum density vectors are shown for some points in the beam.

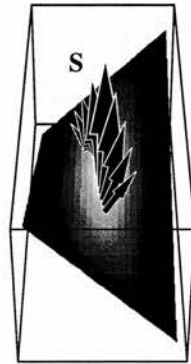


Figure 3.4: Phase front with superimposed intensity distribution and some orbital momentum density vectors for a propeller beam at position  $d = f$ .

## Chapter 4

# Frequency doubling of LG modes

### 4.1 Introduction

In certain media the polarisation is not proportional to the electric field that induced it. The peaks of an electro-magnetic wave propagating through such a non-linear medium are distorted by the electric field due to the polarisation; a frequency analysis reveals the existence of harmonics [46]. The strongest harmonic field is often the second harmonic, which corresponds to twice the optical frequency of the fundamental.

This simple electro-magnetic model of second-harmonic generation can alternatively be described in the photon picture: two photons with the fundamental frequency merge to give one photon at the second-harmonic frequency. The doubling of the optical frequency implies conservation of energy within the two electro-magnetic fields, i.e. no energy is transferred to the non-linear material. Due to the doubling of the wave number, which is a result of the phase-matching condition for efficient second-harmonic generation [46], momentum is also conserved within the two electro-magnetic fields.

The question remains as to what happens to the angular momentum. The spin associated with circular polarisation is not conserved within the two beams:

a light beam cannot carry a spin angular momentum of  $2\hbar$  per photon [47]<sup>1</sup>.

The earliest example of experimental frequency doubling of laser beams with orbital angular momentum was described in ref. [32]. In this experiment a second-harmonic beam with an additional screw-phase dislocation resulted. Although orbital angular momentum was not mentioned explicitly, this result is compatible with conservation of the orbital angular momentum within the light beams. The work described in this chapter examines the fate of the orbital angular momentum of Laguerre-Gaussian modes when they are frequency doubled and discusses the second-harmonic beams.

## 4.2 Frequency doubling of LG modes with $p = 0$

Experimental frequency-doubling of Laguerre-Gaussian modes with radial index  $p = 0$  was first reported in ref. [47]. LG modes with  $p = 0$  have a single-annular-ring intensity distribution. They frequency-double to give a pure Laguerre-Gaussian mode with the same radial mode index  $p' = 0$ , but with an azimuthal index of

$$l' = 2l. \quad (4.1)$$

This result can easily be verified mathematically. At the beam waist,  $z = 0$ , the amplitude of a Laguerre-Gaussian mode, equation (1.27), simplifies to

$$e_{\text{LG}_p^l}(r, \phi, z = 0) \propto \exp\left(-\frac{r^2}{w_0^2}\right) \exp(-il\phi) (-1)^p (r\sqrt{2}/w_0)^l L_p^l(2r^2/w_0^2). \quad (4.2)$$

For  $p = 0$ , the associated Laguerre polynomial  $L_p^l(x)$  takes on the value 1; therefore the expression for the amplitude cross-section at the beam waist for a Laguerre-Gaussian mode with radial mode index  $p = 0$  is of the form

$$e_{\text{LG}_0^l}(r, \phi, z = 0) \propto \exp\left(-\frac{r^2}{w_0^2}\right) \exp(-il\phi) (r\sqrt{2}/w_0)^l. \quad (4.3)$$

The amplitude of the second harmonic field that is generated at one point is proportional to the square of the incident fundamental field there [46]. When

---

<sup>1</sup>To the best of my knowledge, the question of what happens to the spin angular momentum has not been addressed in detail. Possible explanations are that angular momentum associated with the polarisation of the fundamental beam is exchanged with the non-linear crystal and/or with the orbital angular momentum of either of the light beams.

a  $\text{LG}_0^l$  mode is frequency-doubled in a thin crystal positioned at the beam waist, the amplitude of the second harmonic beam in that plane is consequently proportional to the amplitude of the fundamental beam there. The square of the LG mode function given in equation (4.3) is

$$\begin{aligned} \left(\epsilon_{\text{LG}_0^l}(r, \phi, z = 0)\right)^2 &\propto \exp\left(-2\frac{r^2}{w_0^2}\right)\exp(-i2l\phi)(r\sqrt{2}/w_0)^{2l} \\ &= \exp\left(-\frac{r^2}{(w_0/\sqrt{2})^2}\right)\exp(-i(2l)\phi)(r\sqrt{2}/w_0)^{(2l)}, \end{aligned} \quad (4.4)$$

which is again a LG mode function with mode indices  $p' = 0$  and  $l' = 2l$ . In addition, the beam waist size is reduced according to

$$w'_0 = w_0/\sqrt{2}. \quad (4.5)$$

As the orbital angular momentum per photon in a LG mode is proportional to its azimuthal mode index  $l$ , equation (4.1) corresponds to a doubling of the angular momentum per photon in the process of second harmonic generation. However, in the photon picture, second harmonic generation turns two photons with the fundamental frequency,  $\omega$ , into one photon with the second-harmonic frequency,  $2\omega$ . Therefore the doubling of the azimuthal mode index, equation (4.1), expresses the conservation of the orbital angular momentum within the light beam. This implies that no orbital angular momentum is exchanged with the non-linear material.

In this earlier work on frequency-doubling of LG beams, ref. [47], the azimuthal phase structure of the frequency-doubled beam was not measured directly. It was instead assumed that the second harmonic beam is a Laguerre-Gaussian mode again, and the consistency of this assumption demonstrated by conversion of the second harmonic mode into the corresponding Hermite-Gaussian mode by means of a cylindrical lens mode converter [13] (fig. 4.1).

### 4.3 Frequency doubling of LG modes with $p > 0$

The experimental arrangement for the generation of frequency-doubled LG modes and subsequent analysis of their intensity and phase structure, is shown in fig. 4.2. An intra-cavity cross wire is used to generate a Hermite-Gaussian

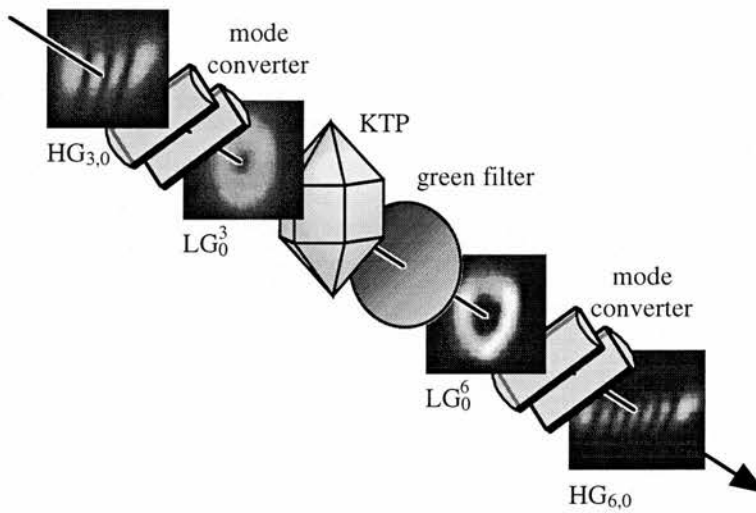


Figure 4.1: Schematic setup and example of modes occurring in the frequency-doubling experiment described in ref. [47]. The beam on the left of the non-linear KTP crystal is pure infra-red, the fundamental wavelength. The filter just behind the KTP crystal filters out that fundamental wavelength, so that only the second harmonic remains.

mode with chosen indices  $m$  and  $n$  from a diode-pumped Nd:YAG laser operating at 1064nm and producing a linearly polarised output power of about 100mW. The Hermite-Gaussian mode is then converted into a corresponding Laguerre-Gaussian mode by means of a cylindrical lens mode converter [13]. The LG mode is subsequently frequency doubled in a KTP crystal of 10mm length, angled-tuned to give phase matching for the second harmonic at 532nm. The efficiency of the process is maximised by focussing the incident beam such that its Rayleigh range is comparable to the length of the crystal [48]. In the configuration shown in fig. 4.2, the second-harmonic beam is selected by a line filter and its azimuthal structure is examined in a mode analyser. The mode analyser shown in fig. 4.3 is a slightly modified version of the configuration described in ref. [49]. It uses a Dove prism in one arm of a Mach-Zehnder interferometer to flip the phase and intensity structure of the beam in this arm in one direction, for example the vertical direction in fig. 4.3. This process also reverses the handedness of this beam. To prevent a difference in the expansion on propagation of the beams passing through the two arms of the interferometer, and a concomitant diminution of the area of overlap behind the interferometer and decrease in the visibility of interference fringes, the other arm contains a glass cylinder of the same optical thickness as the Dove prism. The two beams are made to interfere in a plane behind the interferometer.

Figures 4.4 and 4.5 show the zones of constructive and destructive interference in this plane for input beams with an azimuthal phase term of the form  $\exp(il\phi)$ . In the case of an input beam with a ring-shaped intensity distribution it is desirable but usually very difficult to make the angle of interference between the beams,  $\alpha$ , equal to zero; the corresponding interference pattern then consists of  $2l$  interference maxima uniformly spaced around the ring (fig. 4.6). In the more frequent case of the beams interfering at a non-zero angle the interference pattern becomes a mixture of the “petal pattern” corresponding to the case of a vanishing angle and the straight-line fringes corresponding to two plane waves interfering at an angle. One possible recipe for determining the number  $l$  in the azimuthal phase term  $\exp(il\phi)$  of the input beam from the output of the mode analyser is the following: divide the interference pattern along a line through the centre of the interferogram across the fringes into two halves, as shown in

fig. 4.7; the number of fringes in the two halves then differs by  $2l$ .

Figure 4.8 shows the interferograms obtained for a variety of fundamental Laguerre-Gaussian beams and their second harmonic counterparts. As in the case  $p = 0$  [47], these results confirm that the azimuthal index  $l$  of the beam is doubled in the second harmonic process; in both cases the doubling of the azimuthal mode index corresponds to the conservation of orbital angular momentum within the beams.

The setup in fig. 4.2 could be altered to allow the investigation of the propagation characteristics of the second-harmonic beam. This was done by removing the mode analyser from the setup and placing the camera in the beam. The images thus obtained revealed a slight ellipticity in the beam cross-sections (figures 4.9 and 4.10). This ellipticity is probably due to a slight misalignment either of the cylindrical lenses comprising the mode converter with respect to each other or of the mode converter with respect to the beam. Corrected radial profiles for the fundamental and second harmonic beams were obtained by scaling the images to make them symmetrical and averaging the profiles over 80 azimuths. These profiles were then fitted to the predicted field distributions of a Laguerre-Gaussian and its square respectively, with the amplitude and beam diameter as the fit variables. Figures 4.9 and 4.10 show that the corrected experimental profiles are in good agreement with those predicted.

Figure 4.11 shows both the observed and the theoretical intensity distributions of a frequency-doubled Laguerre-Gaussian mode for a variety of distances from the beam waist. The theoretical intensity distributions were calculated using an algorithm based on a plane-wave decomposition of the light field [50]. The figure shows that the beam, although not structurally stable, shows similar intensity distributions at the beam waist and in the far field. Beams of this type are called self-Fourier beams and are special cases of self-imaging beams.

For a monochromatic beam the far field amplitude distribution is simply the Fourier transform of the distribution at the beam waist. When the Fourier transform of the square of a LG mode function with indices  $l_\omega$  and  $p_\omega$  at the beam waist is taken, it is found that the resulting distribution can be described as a superposition of a number of Laguerre-Gaussian modes, all with the same Rayleigh range and azimuthal index  $l_{2\omega} = 2l_\omega$ , but with the radial mode indices

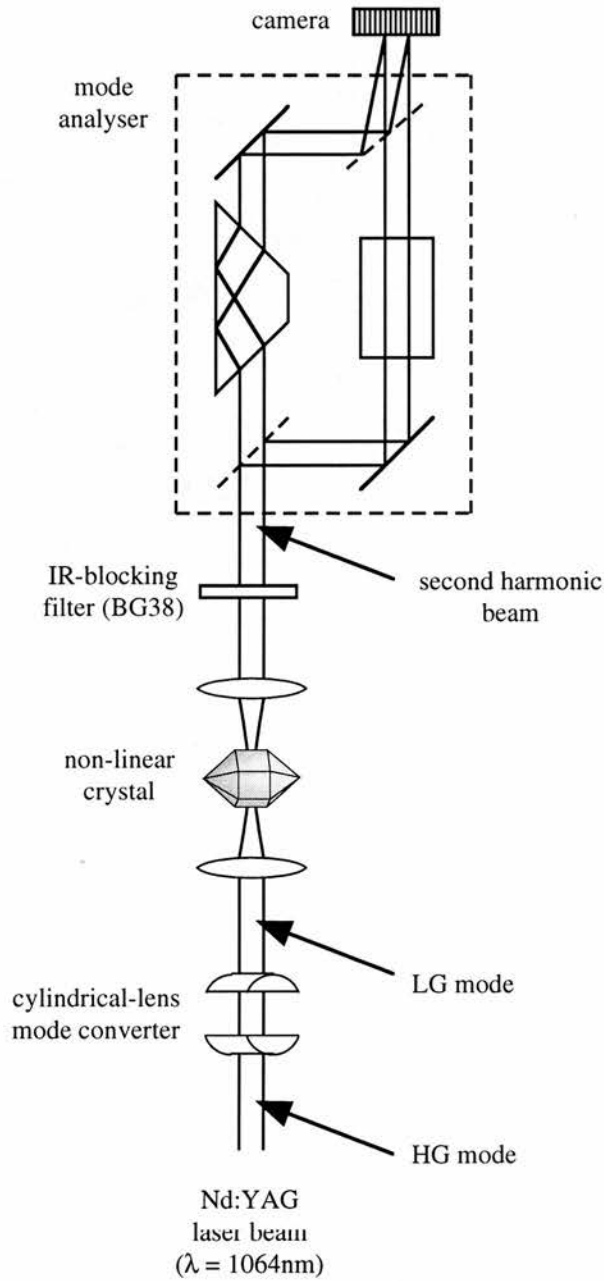


Figure 4.2: Experimental setup for the generation and analysis of frequency-doubled Laguerre-Gaussian modes. The mode analyser allows the examination of the azimuthal phase structure of the beam (see also fig. 4.3).

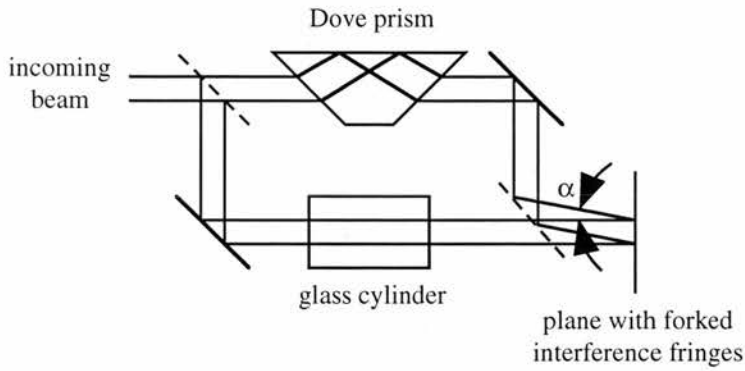


Figure 4.3: Setup for the determination of the azimuthal structure of the incoming light beam. This “mode analyser” allows the incoming light beam to be interfered at an angle  $\alpha$  with its own mirror image.

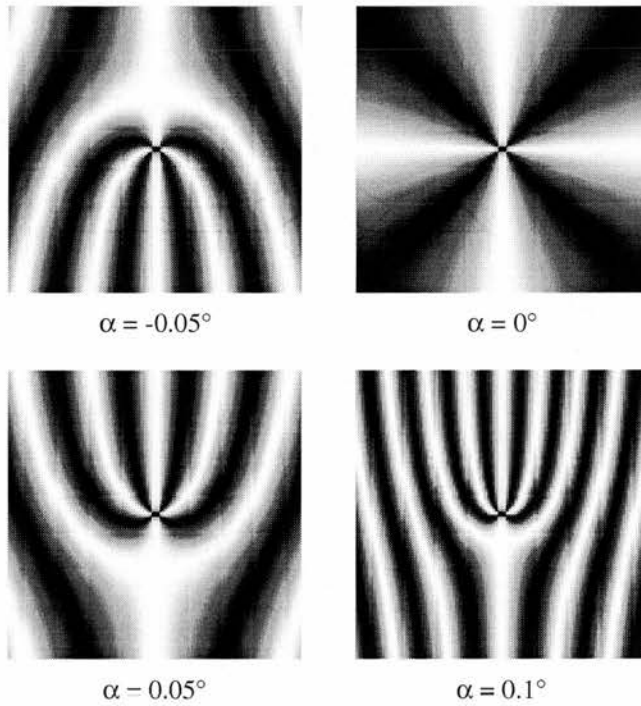


Figure 4.4: Examples of zones of constructive (bright) and destructive (dark) interference in the output from a mode analyser as a function of the intersection angle  $\alpha$  (fig. 4.3). The plots correspond to an input beam of wavelength  $\lambda = 532\text{nm}$  with an azimuthal phase factor  $\exp(i2\phi)$ . The plots represent an area of  $2\text{mm} \times 2\text{mm}$ .

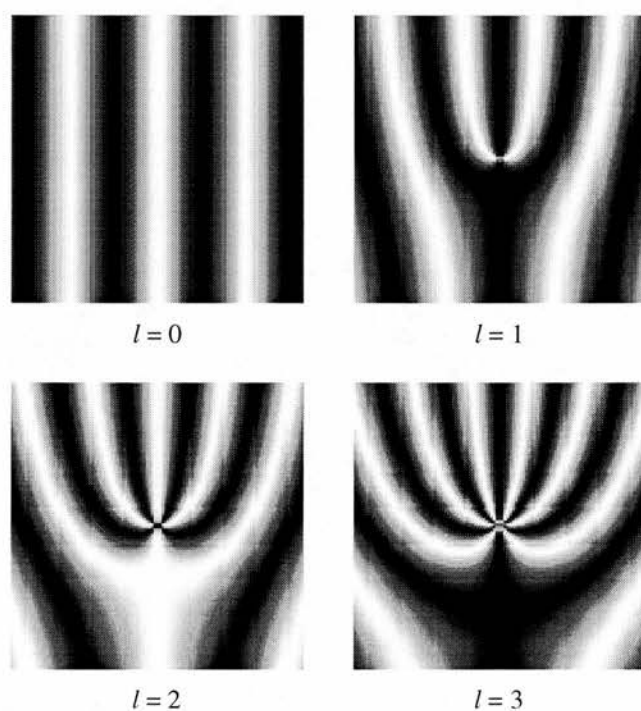


Figure 4.5: Examples of zones of constructive (bright) and destructive (dark) interference in the output from a mode analyser (fig. 4.3) as a function of the azimuthal index  $l$  of the input beam. The wavelength of the input beam is  $\lambda = 532\text{nm}$ . The plots are calculated for an intersection angle  $\alpha = 0.05^\circ$  and each represent an area of  $2\text{mm} \times 2\text{mm}$ .

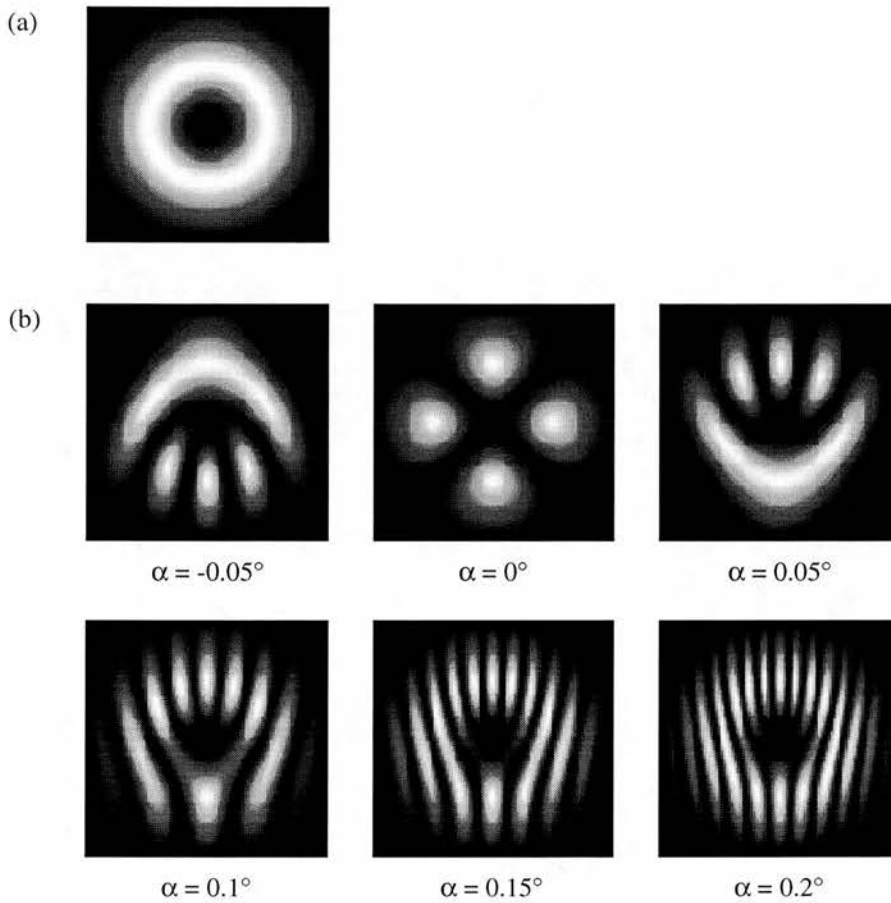


Figure 4.6: Analysis of the azimuthal phase structure of a  $LG_0^2$  mode. (a) shows the intensity cross-section of the LG mode; (b) shows the output from a mode analyser for various intersection angles  $\alpha$ . The plots are calculated for a light wavelength  $\lambda = 532\text{nm}$  and each represent an area of  $2\text{mm} \times 2\text{mm}$ .

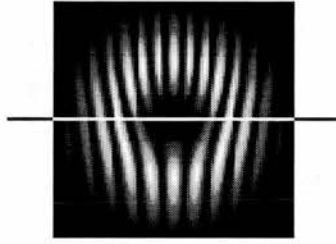


Figure 4.7: Recipe for the extraction of the azimuthal index  $l$  of the input beam from the output of a mode analyser. The difference in the number of fringes in the two halves of the interferogram is  $2l$ .

taking on the different values  $p_{2\omega} \in \{0, 2, 4, \dots, 2p_\omega - 2, 2p_\omega\}$ . In chapter 5 it is shown that such a combination of Laguerre-Gaussian modes constitutes a self-imaging beam.

The work described in this section was published in ref. [51].

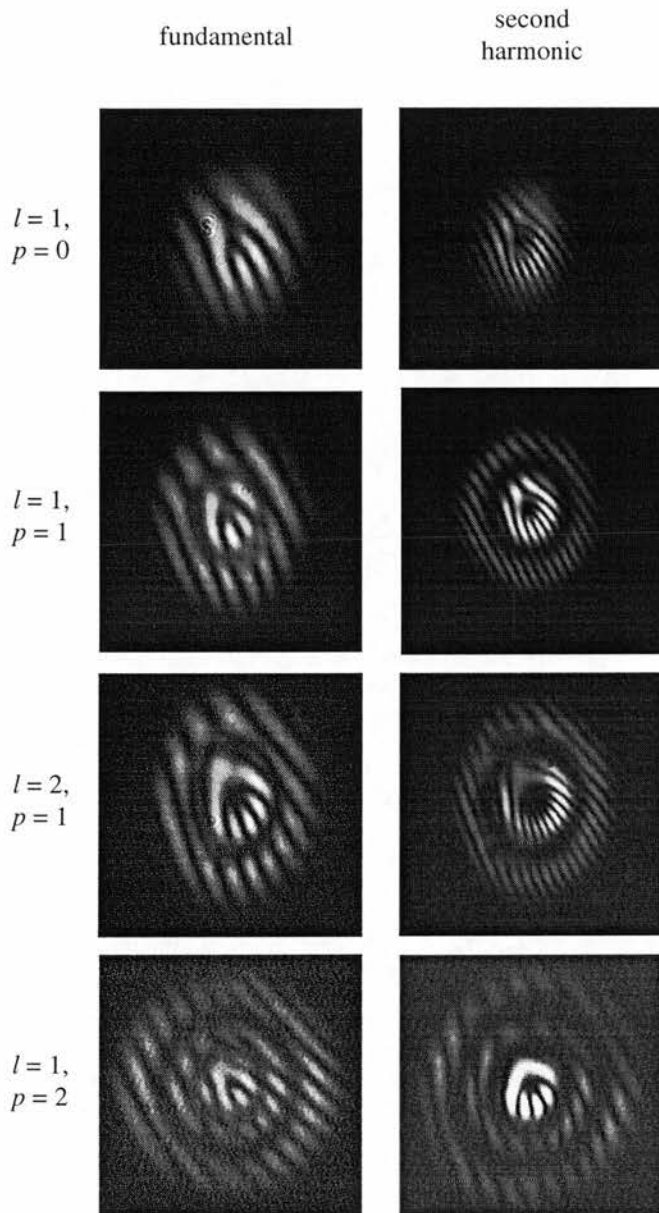


Figure 4.8: Mode analyser output for a variety of Laguerre-Gaussian beams and their second harmonic counterparts.

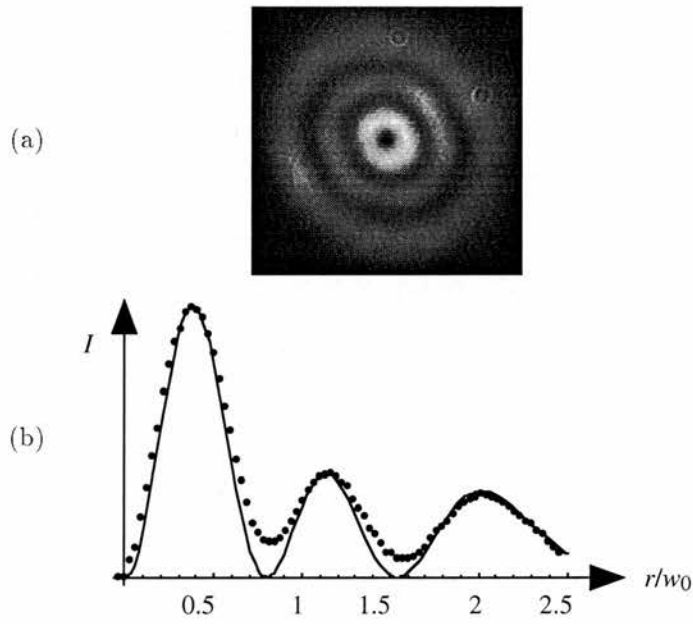


Figure 4.9: Cross-section of a fundamental Laguerre-Gaussian mode with indices  $l = 1$  and  $p = 2$  (a) and the corresponding corrected radial intensity profile (b). The points represent values that were extracted from the observed cross-section, the solid line is the theoretical radial intensity distribution of the Laguerre-Gaussian mode.

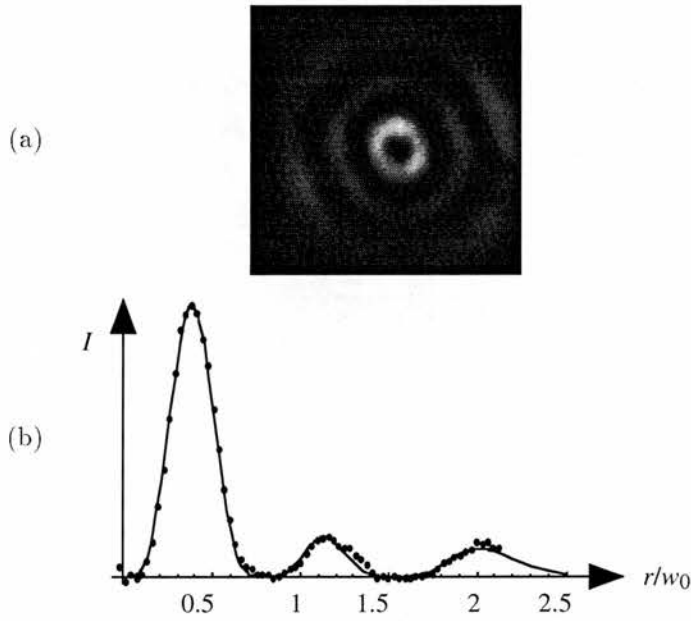


Figure 4.10: Cross-section of the second harmonic of the Laguerre-Gaussian mode in fig. 4.9 (a) and the corresponding corrected radial intensity profile (b). The points represent values that were extracted from the observed cross-section; the solid line is the theoretical radial intensity distribution of the second harmonic of a LG mode with mode indices  $l = 1$  and  $p = 2$ .

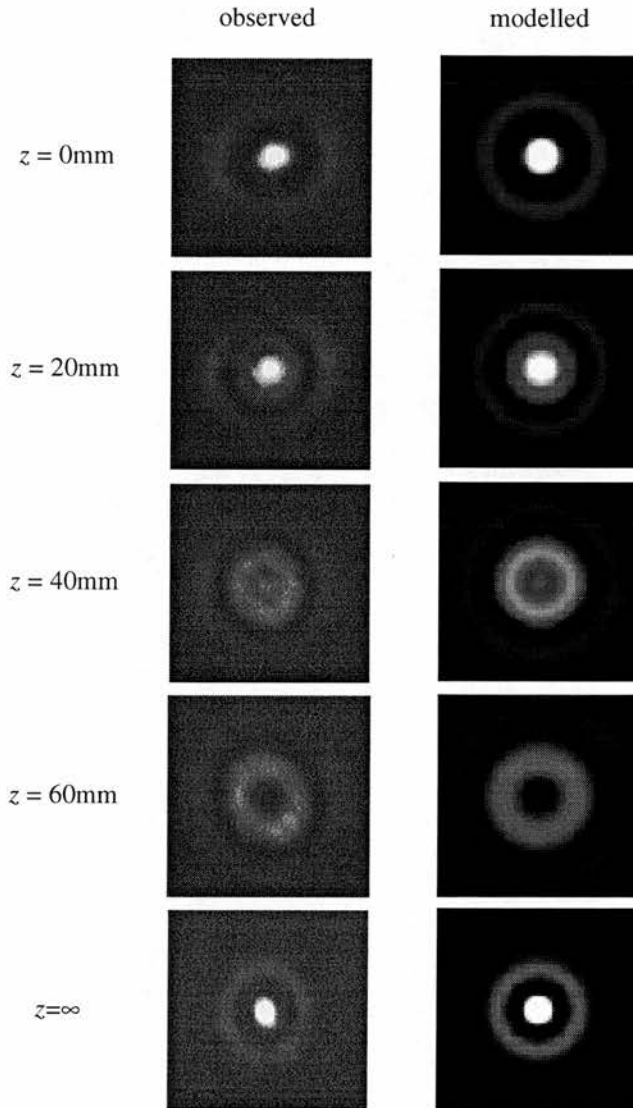


Figure 4.11: Observed and modelled intensity distribution of a frequency-doubled Laguerre-Gaussian mode as it propagates from the beam waist ( $z = 0$ ). The mode indices of the fundamental mode were  $l = 0$  and  $p = 1$ , its Rayleigh range was  $z_R = 112\text{mm}$ .

## Chapter 5

# Self-imaging beams and the Guoy phase

### 5.1 Introduction

Structurally stable beams, i.e. beams with intensity cross-sections that, neglecting radial scaling, are invariant on propagation, are special solutions of the paraxial Helmholtz equation. Examples of this class of beam are the well-known Hermite-Gaussian (HG) and Laguerre-Gaussian (LG) laser modes (section 1.4.2).

Any monochromatic paraxial optical beam can be expanded in terms of HG or LG mode functions with arbitrary (but common) choices of waist location and Rayleigh range  $z_R$  [18]. On propagation, the radial size, the radius of curvature of the phase front and the plane-wave phase shift are equal for every component of such an expansion; yet their superposition is not necessarily structurally invariant. This is due to a subtle but sometimes important added phase shift through the waist region [18] known as the Guoy phase shift,  $\psi_G$ , which affects each HG or LG component individually and is dependent on the indices  $l$  and  $p$  of the corresponding mode function. In the equation for the mode function of a LG mode, equation (1.27), the Guoy phase appears in the form

$$\psi_G = (2p + |l| + 1) \arctan \frac{z}{z_R}. \quad (5.1)$$

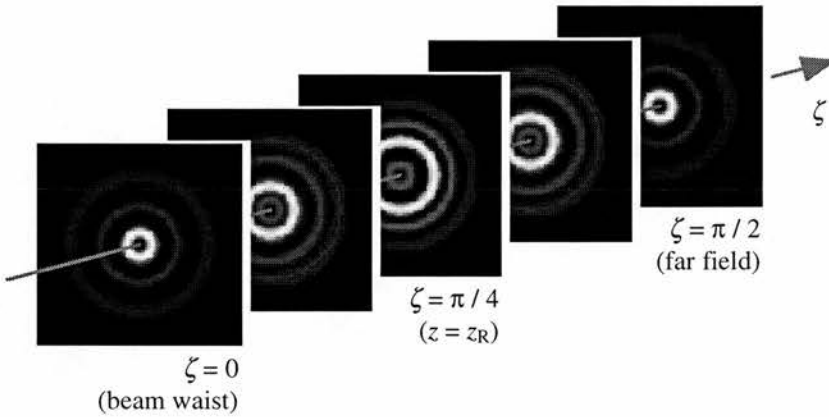


Figure 5.1: Example of a self-imaging beam. This second harmonic of a Laguerre-Gaussian mode with mode indices  $l = 1$  and  $p = 2$  can be written as a superposition of LG modes with indices  $l = 2$  and  $p = 0, p = 2$ , and  $p = 4$ , respectively [51];  $z_R$  is the Rayleigh range of the Laguerre-Gaussian components of the beam; beam widening has been ignored for simplicity.

In this chapter the Guoy phase of the individual components in superpositions of LG modes is utilized in the construction of self-imaging beams, spiral-type beams and structurally stable beams. The choice of LG modes rather than HG modes as the basis set greatly simplifies the treatment of beams with similar but rotated intensity cross-sections.

## 5.2 Self-imaging superpositions of LG modes

Beams that exhibit a number of similar intensity cross-sections are known as self-imaging beams (for a review of the extensive literature see, for example, ref. [52]). Figure 5.1 gives an example of a self-imaging beam; this beam is a superposition of LG modes of the type that was encountered in the preceding chapter in the form of the second harmonic of LG modes with radial indices  $p > 0$ . The propagation distance is not given in terms of  $z$  but  $\zeta$ , which is defined as

$$\zeta = \arctan \frac{z}{z_R}. \tag{5.2}$$

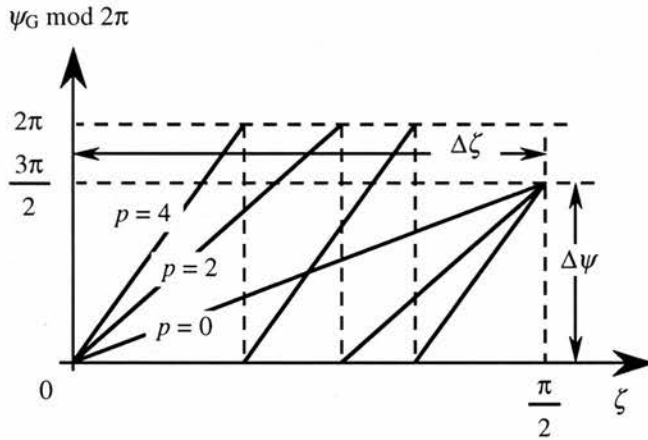


Figure 5.2: Plot of the Guoy phases (modulo  $2\pi$ ) of the components of the beam in fig. 5.1. The Guoy phase of the component with the indices  $l = 2$  and  $p = 0$  completes three quarters of a full  $2\pi$  cycle, those of the components with  $p = 2$  and  $p = 4$  (both have the same azimuthal mode index  $l = 2$ ) complete one and two additional full cycles, respectively.

When measured in terms of this variable, the planes of similar intensity distributions of the beams that are to be constructed in this section are equidistant. In terms of  $\zeta$ , expression (5.1) for the Guoy phase has the form

$$\psi_G(\zeta) = (2p + |l| + 1)\zeta. \quad (5.3)$$

Figure 5.2 shows a plot of the Guoy phase terms of the three LG components of the beam from fig. 5.1. It can be seen that they are the same for all three components only at the beam waist and in the far field, thus giving similar intensity distributions in the corresponding planes.

The separation  $\Delta\zeta$  between planes with similar intensity cross-sections as well as the phase offset  $\Delta\psi$  between the corresponding amplitude cross-sections (see fig. 5.2) can both be chosen arbitrarily. This imposes a condition on the Guoy phases of the constituent LG modes of the beam, which states that for each constituent mode there exists an integer  $n$  such that

$$\psi_G(\zeta + \Delta\zeta) = \psi_G(\zeta) + n \cdot 2\pi + \Delta\psi. \quad (5.4)$$

In addition to being similar, cross-sections can be rotated with respect to each other. An LG mode has an azimuthal phase term of the form  $\exp(il\phi)$ ,

which, on rotation through an angle  $\Delta\phi$ , becomes  $\exp(il\phi)\cdot\exp(il\Delta\phi)$ . Therefore a rotation through an angle  $\Delta\phi$  phase-shifts an LG mode by  $\psi_R(\Delta\phi) = l \cdot \Delta\phi$ . Consequently the condition on each component of a superposition of LG modes for it to have a periodicity of  $\Delta\zeta$ , after which the amplitude cross-section is rotated by an angle  $\Delta\phi$ , is

$$\psi_G(\zeta + \Delta\zeta) = \psi_G(\zeta) + \psi_R(\Delta\phi) + n \cdot 2\pi + \Delta\psi, \quad n \in \{0, \pm 1, \pm 2, \dots\}. \quad (5.5)$$

On substitution of the expressions for the Guoy phase (equation (5.3)) and  $\psi_R$ , this becomes a condition on the mode indices  $l$  and  $p$  of the constituent modes and simplifies to

$$(2p + |l| + 1)\Delta\zeta = l \cdot \Delta\phi + n \cdot 2\pi + \Delta\psi, \quad n \in \{0, \pm 1, \pm 2, \dots\}. \quad (5.6)$$

This condition constitutes a criterion for the selection of LG modes, any superposition of which will result in a beam with an amplitude cross-section recurring with periodicity  $\Delta\zeta$ , rotated by an angle  $\Delta\phi$ , and phase-offset by  $\Delta\psi$ .

In the preceding chapter the second harmonics of LG modes with radial indices  $p > 0$  were expressed as superpositions of LG modes. It was found that the constituent LG modes all have the same azimuthal index  $l = 2l_\omega$ , where  $l_\omega$  is an integer, and radial indices  $p \in \{0, 2, 4, 6, \dots\}$ . It is straightforward to show that for each superposition of this type a value of  $\Delta\psi$  can be found such that the indices of all the constituent LG modes satisfy condition (5.6) with  $\Delta\zeta = \pi/2$  and  $\Delta\phi = 0$ . Consequently the intensity cross-section of such beams in the far field is similar to that at the beam waist, as stated in chapter 4.

It is interesting to note that for any superposition of three (or less) LG modes with mode indices  $l_i$  and  $p_i$ , there exist values for  $\Delta\zeta$ ,  $\Delta\phi$ , and  $\Delta\psi$  such that condition (5.6) is satisfied by all three modes. Therefore any superposition of three LG modes can be interpreted as a self-imaging beam. It should be noted that the solution for the period  $\Delta\zeta$  might turn out to be greater than  $\pi$ , which in terms of  $z$  corresponds to a non-physical separation of  $\Delta z > \infty$  between neighbouring similar cross-sections.

Figure 5.3 illustrates the propagation of the periodic beam

$$\text{LG}_2^{-4}(r, \phi, z) + \text{LG}_1^{-10}(r, \phi, z) + \text{LG}_3^{-14}(r, \phi, z) + \text{LG}_2^{-20}(r, \phi, z). \quad (5.7)$$

It has been constructed with the help of table 5.1, which lists some of the possible combinations of indices  $l$  and  $p$  of LG modes which can be superimposed

$n$	$p$	$l$
...		
-2	0	32
	1	34
	2	36
	...	...
-1	0	16
	1	18
	2	20
	...	...
0	0	0
	1	2
	2	4
	...	...
1	2	-4
	5	-2
	8	0
	9	2
	10	4
	...	...
2	1	-10
	4	-8
	...	...
3	0	-16
	3	-14
	...	...
4	2	-20
	5	-18
	...	...
...		

Table 5.1: Some combinations of indices of LG modes that add up to form periodic beams with beam parameters  $\Delta\zeta = \pi/8$ ,  $\Delta\phi = \pi/4$ , and  $\Delta\psi = \pi/8$ .

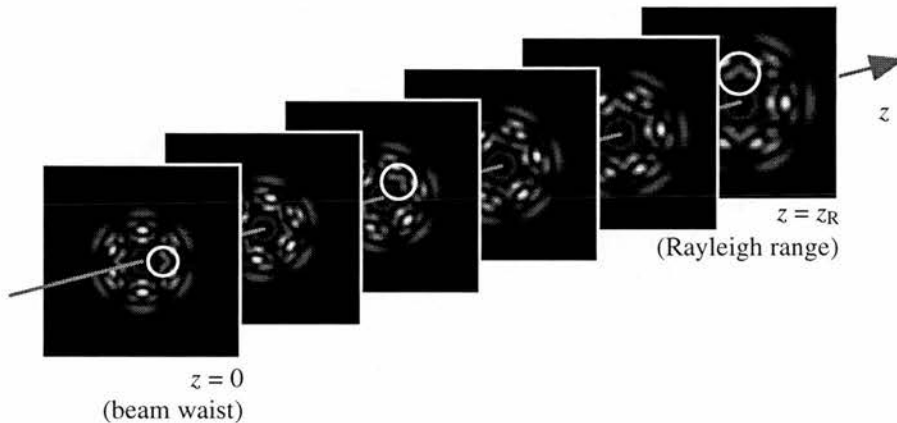


Figure 5.3: Simulated propagation of a rotating self-imaging beam. A feature common to some similar planes is marked.

arbitrarily to give a periodic beam with the following parameters:  $\Delta\zeta = \pi/8$  (first repetition of the amplitude distribution at the beam waist occurs half way between  $\zeta = 0$  (beam waist) and  $\zeta = \pi/4$  (Rayleigh range));  $\Delta\phi = \pi/4$  (cross-sections a distance apart are rotated by  $45^\circ$  with respect to each other); and  $\Delta\psi = \pi/8$ . Substituting these values into equation (5.6) gives the condition  $2p = 2l - |l| + 16n$ ,  $n \in \{0, \pm 1, \pm 2, \dots\}$  on the indices  $l$  and  $p$  of the constituent modes for this family of periodic beams. Note that expression (5.7) is a superposition of modes associated with a variety of values of  $n$  ( $n = 1, 2, 3, 4$ ), as the presence of only one value of  $n$  results in a different class of beam which is discussed in the following section.

### 5.3 Spiral-type beams

An interesting limiting case is  $\Delta\zeta \rightarrow 0$ . Here the planes of similar intensity cross-sections move so close together that the intensity cross-sections of the resulting beam are, on propagation, invariant in all respects other than constant rotation and change in radial size. Beams of this type are known as spiral-type beams [53, 54, 55]. For these beams, as the phase is a continuous function,  $n$  must be zero, and the rotation angle  $\Delta\phi$  and the phase offset  $\Delta\psi$  must approach zero as  $\Delta\zeta$  approaches zero. The ratios  $\delta\phi = \Delta\phi/\Delta\zeta$  and  $\delta\psi = \Delta\psi/\Delta\zeta$ , however,

can be finite. When written in terms of these ratios the condition on the mode indices reads

$$2p + |l| + 1 = l \cdot \delta\phi + \delta\psi. \quad (5.8)$$

Note that values of  $\delta\phi$  and  $\delta\psi$  can be found for any superposition of two (or less) LG modes, which therefore represents a spiral-type beam.

In ref. [53], equation (5.8) is derived directly from the wave equation. This study of superpositions of LG modes in terms of the Guoy phase not only offers an alternative, possibly more intuitive derivation, it also links spiral-type beams into the framework of self-imaging beams.

## 5.4 Structurally stable beams

Spiral-type beams with a rotation rate of

$$\delta\phi = 0 \quad (5.9)$$

are structurally stable beams. Substitution of equation (5.9) into the condition for spiral-type beams, equation (5.8), yields the condition on the mode indices of LG components that constitute structurally stable beams. This condition reads

$$2p + |l| + 1 = \delta\psi. \quad (5.10)$$

This condition can be easily understood as implying the same Guoy-phase dependence  $\psi_G(\zeta) = \delta\psi \cdot \zeta$  for every constituent mode. This is equivalent to all the constituent modes having the same mode order [13]

$$N = 2p + |l| = \delta\psi - 1. \quad (5.11)$$

Table 5.2 lists some possible combinations of indices of LG modes for a number of values of the mode order  $N$ . Obviously, condition (5.10) is satisfied by any single Laguerre-Gaussian mode. It is also satisfied by any single Hermite-Gaussian mode<sup>1</sup>. Further examples of structurally stable beams that are constructed according to the condition specified in equation (5.10) can be found in ref. [57].

<sup>1</sup>This can be seen from equations (8)-(11) in ref. [56].

$N$	$p$	$l$
0	0	0
1	0	$\pm 1$
2	0	$\pm 2$
	1	0
3	0	$\pm 3$
	1	$\pm 1$
4	0	$\pm 4$
	1	$\pm 2$
	2	0
...		

Table 5.2: Some combinations of indices of LG modes that add up to form different classes of structurally stable beams, corresponding to different values of the mode order  $N$ . For example, structurally stable beams corresponding to a value of  $N = 3$  can be any superposition of LG modes with the following mode indices:  $p = 0$  and  $l = +3$ ,  $p = 0$  and  $l = -3$ ,  $p = 1$  and  $l = +1$ ,  $p = 1$  and  $l = -1$ .

## 5.5 Self-imaging superpositions of other beams

Constructions similar to the one in this chapter can be performed using other families of beams. In particular, Hermite-Gaussian modes, which have a Guoy phase term similar to that of LG modes, can be used to construct self-imaging beams; however, the extension to rotated amplitude patterns is perhaps less obvious. As an alternative to the Guoy phase, the plane-wave phase  $k_z \cdot z$  can be used in superpositions of beams with different values of  $k_z$ , i.e. with different wavelengths, but otherwise identical phases and identical beam expansion. In a recent publication [58], this approach was used to construct spiral-type superpositions of Bessel beams, which are known as Helicon waves [59].

The work described in this chapter has been published in ref. [35].

## Chapter 6

# Rotational Doppler effect

### 6.1 Translational Doppler effect

An observer determines the frequency of a monochromatic light beam by measuring the time  $T$  after which the beam has gone through one phase cycle. The beam as a whole is then in exactly the same state as before. Its frequency,  $\nu$ , is  $\nu = 1/T$ .

Consider a light beam *in the laboratory frame of reference*. An observer travelling in the same direction as the light beam would be seen to encounter the phase fronts with a cycle time  $T'$  that is longer than that for an observer at rest; obviously, an observer travelling almost at the same speed as the phase fronts would be seen to encounter the phase fronts at comparatively very long intervals. Generally, in the laboratory frame the speed  $u$  of the phase fronts in a light beam relative to an observer is related to the wavelength  $\lambda$  of the beam and the cycle time  $T'$  with which the observer is seen in the laboratory frame to encounter the phase fronts through

$$u = \frac{\lambda}{T'} = \lambda\nu'. \quad (6.1)$$

With the wave number  $k = 2\pi/\lambda$ , the frequency  $\nu'$  of the encounters between the phase fronts and the observer can be written as

$$\nu' = \frac{k}{2\pi}u. \quad (6.2)$$

For an observer moving with speed  $v$  in the opposite direction of the phase fronts

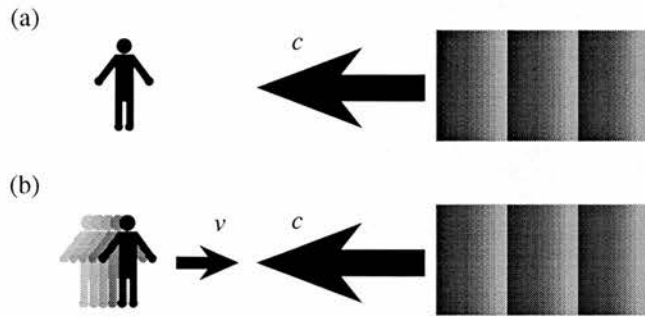


Figure 6.1: Illustration of the (translational) Doppler shift. (a) A light beam is moving with speed  $c$  towards an observer at rest. (b) In the laboratory frame, the relative speed between the light beam and an observer moving with speed  $v$  in the opposite direction is  $c + v$ .

(fig. 6.1), and therefore with a speed  $u = c + v$  relative to the phase fronts, this becomes

$$\nu' = \frac{k}{2\pi}(c + v) = \nu + \Delta\nu, \quad (6.3)$$

where

$$\nu = \frac{k}{2\pi}c \quad (6.4)$$

and

$$\Delta\nu = \frac{k}{2\pi}v. \quad (6.5)$$

Please note that a relative speed  $u > c$  between observer and light beam, *measured in the laboratory frame*, is not in contradiction with Special Relativity.

It turns out<sup>1</sup> that the frequency shift that the observer would measure is also described, to first order, by equation (6.5). This frequency shift is therefore referred to as *first-order* or *non-relativistic*<sup>2</sup> Doppler shift.

<sup>1</sup>Equation (6.5) represents the terms up to order  $(v/c)^1$  in a power series expansion of the accurate, relativistic formula for the Doppler-shifted frequency [4] in the frame of reference of the observer,

$$\nu' = \nu \frac{\sqrt{1 - (v/c)^2}}{1 - v/c}. \quad (6.6)$$

<sup>2</sup>The first-order Doppler shift describes well the frequency shift measured by any observer moving at a slow, non-relativistic, speed  $v$ .

Note that the momentum per photon in a light beam is  $\delta P = \hbar k$  [60], so the non-relativistic Doppler shift of a light beam can be written as

$$\Delta\nu = \frac{\delta P \cdot v}{2\pi\hbar}. \quad (6.7)$$

It is therefore proportional to both the momentum per photon in the beam,  $\delta P$ , and the relative speed between beam and observer,  $v$ .

If more than one wavelength is present in the beam, each Fourier component of the beam is shifted individually according to equations (6.5) or (6.7).

## 6.2 Rotational Doppler effect for circularly polarised light

Instead of the translational movement of the phase fronts, one can consider the rotation of the electric field vector at any point in a circularly polarised light beam. The rotation frequency,  $f$ , is one full clockwise ( $\sigma = -1$ ) or anti-clockwise ( $\sigma = +1$ ) rotation per optical cycle time  $T$ , so  $f = 1/(\sigma T) = \nu/\sigma$ , where  $\nu$  is the optical frequency of the beam and  $\sigma = \pm 1$  corresponds to right/left-handed circular polarisation. Additional uniform rotation of the field about the direction of propagation with frequency  $F$  with respect to the observer (fig. 6.2) adds directly to the original rotation frequency  $f$  of the electric field vectors, so that their new frequency is  $f' = f + F$ . As before, the observer sees the field return to its original state, i.e. perform one optical cycle, after one rotation of the field. Therefore the optical frequency of the rotated beam becomes  $\nu' = \sigma f' = \nu + \Delta\nu$ , where

$$\Delta\nu = \sigma F. \quad (6.8)$$

The similarity between this frequency shift and the Doppler shift was first fully appreciated by Garetz [61], who consequently referred to it as *angular Doppler shift*.

In a separate family of papers (ref. [62] and references therein), the interaction of polarised light and rotating wave plates is analysed either as an evolving Berry phase [63] or in terms of an energy exchange between the light and the wave plate [62]. This energy exchange is due to the spin angular momentum

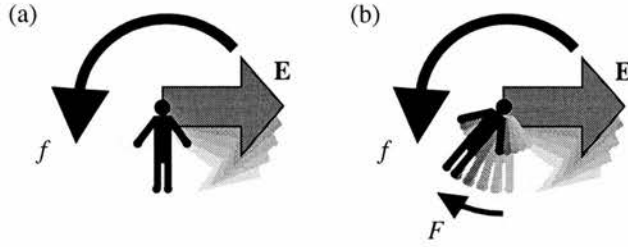


Figure 6.2: Illustration of the rotational Doppler shift of a circularly polarised light beam. (a) An observer at rest sees the electric and magnetic field vectors,  $\mathbf{E}$  and  $\mathbf{B}$ , rotate with angular frequency  $f = \nu/\sigma$ , where  $\sigma = \pm 1$  for right/left-handed circular polarisation. (b) An observer rotating with angular frequency  $-F$  sees the field vectors rotate with angular frequency  $f' = f + F$ .

content of circularly polarised light: as a half-wave plate reverses the handedness of the circular polarisation and thereby the sign of the spin angular momentum,  $\mathbf{s}$ , in the beam, it experiences a torque  $\mathbf{T} = d\mathbf{s}/dt$ . When the wave plate rotates with this torque, the light beam produces work and therefore loses energy.

The spin angular momentum per photon associated with circularly polarised light is  $\delta S = \sigma\hbar$ , where  $\sigma = \pm 1$  for right/left-handed circular polarisation, pointing in the direction of propagation. Utilising this, and also using the angular velocity  $\omega = 2\pi F$ , the shift in frequency of a rotating circularly polarised light beam, equation (6.8), can be written in the form

$$\Delta\nu = \frac{\delta S \cdot \omega}{2\pi\hbar}. \quad (6.9)$$

In the case of a rotating light beam with arbitrary (elliptical) polarisation, the electric field vectors can be decomposed into their circularly polarised components of opposite handedness<sup>3</sup>. The frequencies of these components are then shifted individually by the rotation of the beam, according to equation (6.8).

<sup>3</sup>Transverse fields can be described either by their Cartesian components,  $e_x$  and  $e_y$ , or by the (complex) amplitude of their left/right-hand circular polarisation components,  $e_l$  and  $e_r$ . The two descriptions are related through the following set of equations:

$$\begin{aligned} \mathbf{E} &= \begin{pmatrix} E_x \\ E_y \end{pmatrix} = \begin{pmatrix} e_x \\ e_y \end{pmatrix} + \text{c.c.} = \left( e_x \begin{pmatrix} 1 \\ 0 \end{pmatrix} + e_y \begin{pmatrix} 0 \\ 1 \end{pmatrix} \right) + \text{c.c.} \\ &= \left( e_r \begin{pmatrix} 1 \\ i \end{pmatrix} + e_l \begin{pmatrix} 1 \\ -i \end{pmatrix} \right) + \text{c.c.} \end{aligned} \quad (6.10)$$

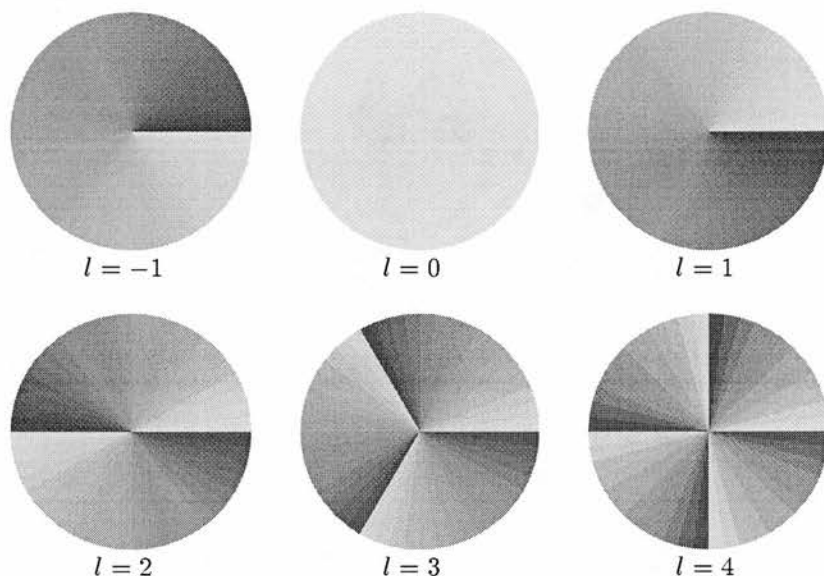


Figure 6.3: Gray-scale representations of phase cross-sections of the form  $\exp(il\phi)$ . Light gray corresponds to phase 0, dark gray corresponds to phase  $2\pi$ . Note that the connecting line between areas with phase 0 and phase  $2\pi$  does not represent a phase discontinuity. However, the phase distributions corresponding to values  $l \neq 0$  contain a phase singularity in the centre, where the phase simultaneously takes on all possible values between 0 and  $2\pi$ .

### 6.3 Rotational Doppler effect for light beams with helical phase fronts

In section 1.4, some analogies between circularly polarised light and light beams with an azimuthal phase dependence of the form  $l\phi$  are mentioned. In this section another analogy between the two cases is exploited: the time evolution of both can be described as a uniform rotation about the direction of propagation.

Figure 6.3 shows a schematic representations of phase cross-sections of the form  $l\phi$ . During one optical cycle, the phase pattern rotates through  $1/l$  of a

Solving for  $e_l$  and  $e_r$  gives

$$e_l = (e_x + ie_y)/2 \quad (6.11)$$

$$e_r = (e_x - ie_y)/2. \quad (6.12)$$

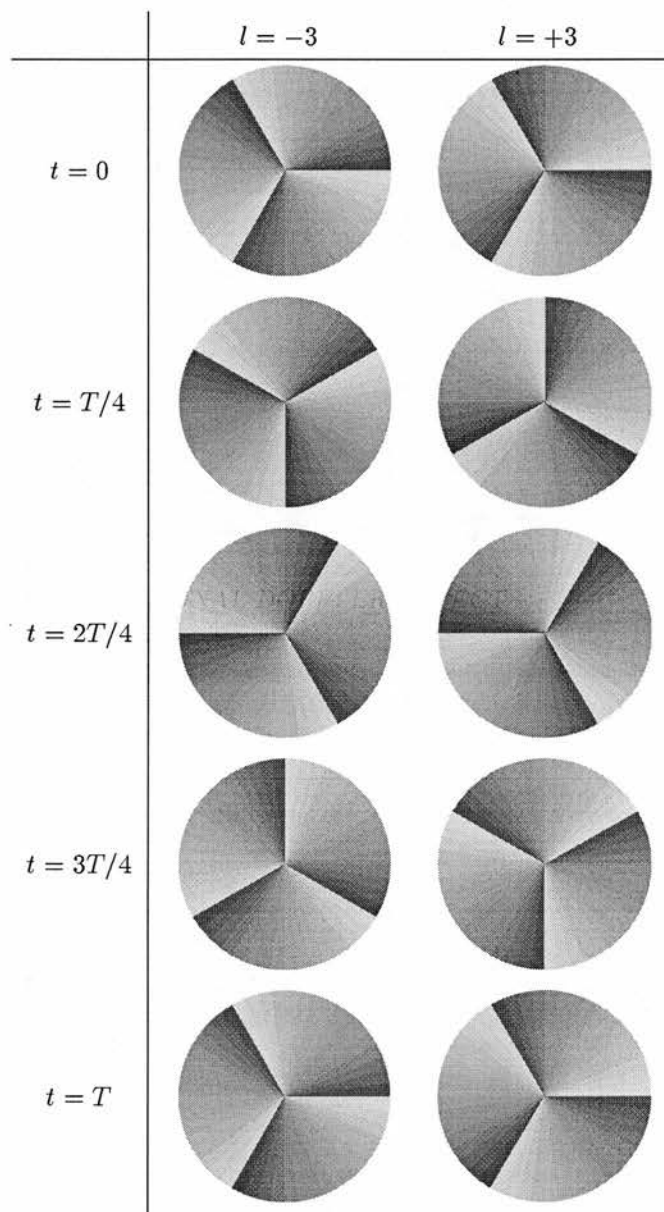


Figure 6.4: Time evolution of phase cross-sections through light beams with an azimuthal phase dependence of the form  $l\phi$ , for  $l = -3$  (left) and  $l = +3$  (right).  $T$  is the time period of the beams. During one phase cycle, a beam with  $l = -3$  performs  $1/3$  of a full anti-clockwise rotation, a beam with  $l = +3$  performs  $1/3$  of a full clockwise rotation.

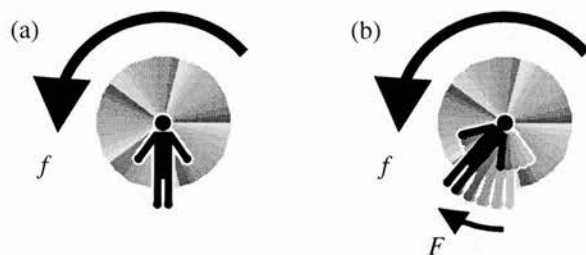


Figure 6.5: Rotational Doppler shift of a scalar beam with an azimuthal phase factor of the form  $\exp(il\phi)$ . (a) An observer at rest sees the cross-section through the electric field of the beam rotate at an angular frequency that is proportional to the optical frequency of the beam. (b) Additional rotation of the beam relative to the observer shifts the optical frequency as measured by the observer.

full rotation (fig. 6.4).

Additional rotation of the phase pattern with frequency  $F$  causes the beam to rotate with rotational frequency  $f' = f + F$  (fig. 6.5). As before, the phase passes through  $l$  complete cycles during each full rotation of the beam. Consequently, uniform beam rotation with frequency  $f'$  corresponds to an optical frequency of  $\nu' = lf' = lf + lF = \nu + \Delta\nu$ , which differs from the optical frequency of a beam that is not subject to additional rotation by

$$\Delta\nu = lF. \quad (6.13)$$

This idea can be illustrated with the help of a pasta twist (fig. 1.6), a good model of the phase fronts in a beam with a phase cross-section of the form  $l\phi$  with  $l = 3$ . The number of arms of a pasta twist, that is moving uniformly in the direction of its central axis, which pass through a point per unit time corresponds to the number of phase fronts of a propagating beam per unit time and therefore its optical frequency. The other way to pass a number of arms of the pasta twist through a point is, of course, to rotate the pasta twist about its central axis. On each rotation, all three arms of the pasta twist pass through the point; uniform rotation with frequency  $F$  therefore passes arms through the point with frequency  $3F$ . For the corresponding light beam, this translates into a shift of its optical frequency by the same amount.

As mentioned in section 1.4, light beams with an azimuthal phase factor of

the form  $\exp(il\phi)$  carry an orbital angular momentum per photon of  $\delta L = l\hbar$  [2]. This allows the frequency shift (6.13) to be written in the form

$$\Delta\nu = \frac{\delta L \cdot \omega}{2\pi\hbar}, \quad (6.14)$$

where the angular velocity  $\omega = 2\pi F$  has been used again instead of the rotational frequency  $F$ . Please note that this equation represents the analog of equations (6.7) and (6.9) for the case of orbital angular momentum.

This frequency shift due to the rotation of the phase and intensity structure of a light beam is not without precedent. Nienhuis [64] predicted that a rotating  $\pi$  mode converter, which changes the sense of the orbital angular momentum of the beam passing through it, would shift the frequency of the beam. The lens configuration that constitutes a  $\pi$  mode converter flips the beam in one direction which is given by the axes of the cylindrical lenses. When such a device is rotated, the phase and intensity structure of the transmitted beam also rotates. Therefore Nienhuis' frequency shift is simply an example of the rotational Doppler shift described in this section. The so-called *azimuthal Doppler shift* [65] experienced by an atom or ion moving in a field with a phase structure of the form  $\exp(il\phi)$ , is also thought to be an example of this rotational Doppler shift [66].

In the case of the rotation of the phase and intensity structure of an arbitrary light beam, its amplitude cross-section can be decomposed in terms of Laguerre-Gaussian modes, which form a complete basis set (see section 1.4.2). As Laguerre-Gaussian modes have a phase structure of the form  $\exp(il\phi)$ , where  $l$  is the azimuthal mode index, each Laguerre-Gaussian component is frequency-shifted individually in proportion to its azimuthal mode index,  $l$ .

### 6.3.1 Experiment

Nienhuis' predicted "Doppler effect induced by rotating lenses" [64] was derived for a Laguerre-Gaussian beam passing through a rotating  $\pi$  converter, a configuration of cylindrical lenses that reverses the handedness of all the Laguerre-Gaussian components in a beam passing through it. The same can be achieved using a Dove prism [60] instead of the configuration of cylindrical lenses. Rotation of the cylindrical lenses or of the Dove prism through an angle  $\alpha$  about the

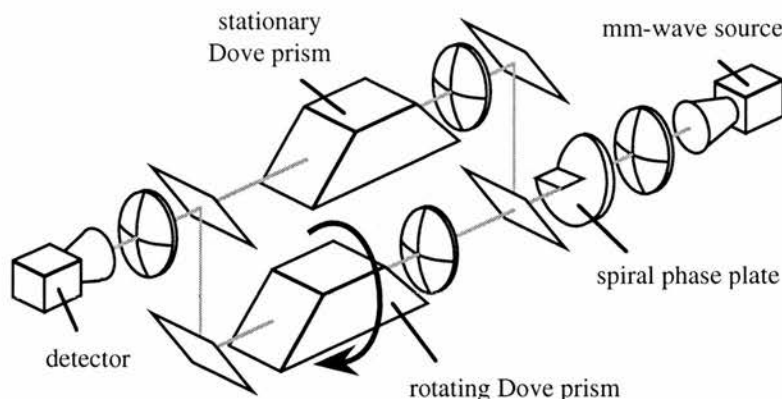


Figure 6.6: Experimental setup for the observation of the rotational Doppler shift for light with an azimuthal phase structure of the form  $l\phi$ .

optical axis causes the transmitted beam to rotate through an angle  $2\alpha$ . Consequently, uniform rotation of the cylindrical lenses or Dove prism with frequency  $F/2$  causes the transmitted beam to rotate with frequency  $F$ . While the phase and intensity structure of a beam is rotated by a Dove prism, the polarisation state of the beam remains sufficiently unchanged to be ignored for the purposes of this experiment<sup>4</sup> [67].

To rotate the transmitted beam without any associated translation or angular deviation, the axis of the Dove prism must be aligned to within a fraction of the wavelength of the light. This requirement is extremely challenging in the optical regime, but is easy to satisfy in the mm-wave regime, in which the experiment was performed. The mm-wave-optical components such as lenses and prisms used in the experiment were fabricated from high-density polyethylene (HDPE) [68].

The light source used in the experiment was an Indium Phosphide Gunn diode oscillating at 94GHz [69]. An impedance-matched feed horn launched a monochromatic Gaussian beam into free space. The required  $l\phi$  phase dependence was introduced into the beam by passing it through a spiral phase plate [25], the optical thickness of which varied linearly with azimuthal angle  $\phi$ .

The beam was then passed through a Mach-Zehnder interferometer with a

<sup>4</sup>A polarisation analysis shows that if the prism is rotated between parallel polarisers the transmitted intensity does not vary by more than 15%.

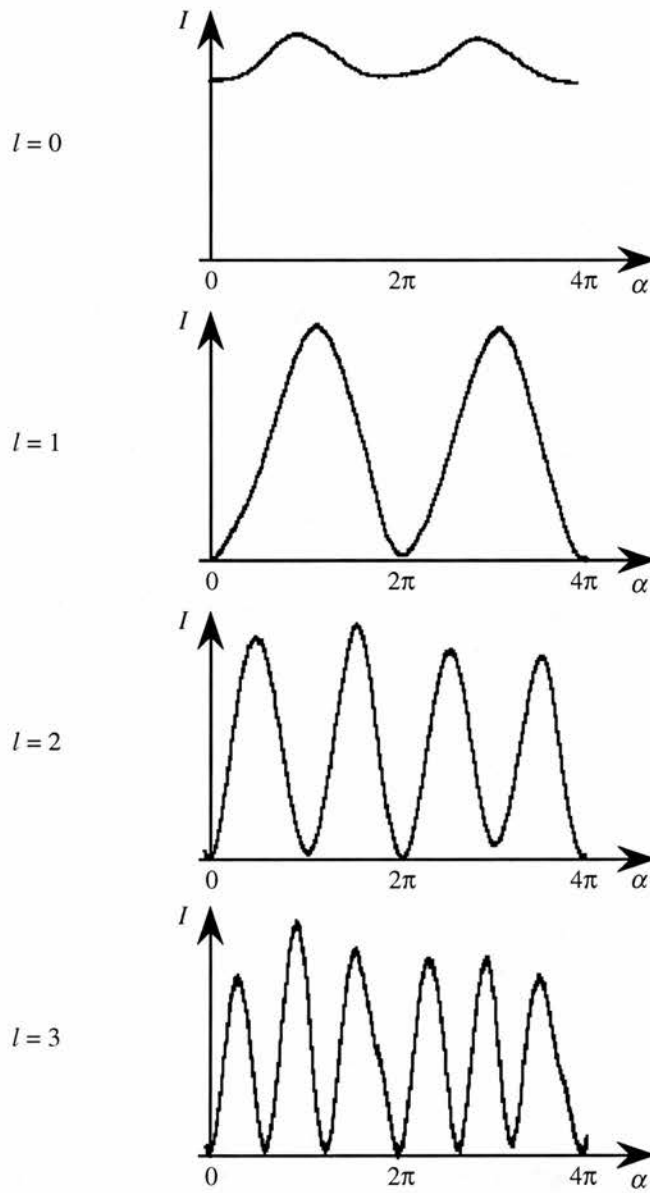


Figure 6.7: Interference between two beams with an azimuthal phase factor of the form  $\exp(il\phi)$ , one rotating and the other one at rest.  $\alpha$  denotes the rotation angle of the former beam. The curves have been plotted over one revolution of the Dove prism used to rotate the beam, which corresponds to two revolutions of the beam. The amplitude modulation in the observed difference frequency, particularly evident for  $l = 0$ , arises from the small change in polarisation as the beams traverse the Dove prisms [67].

Dove prism in each arm, one rotating, the other one at rest (fig. 6.6). The non-rotating Dove prism ensured that the beams in both arms had the same helicity at the output, which resulted in the interference between the two beams after recombination to be uniform across the whole aperture. This allowed the superposition of the two beams to be focussed onto a single detector and their interference to be recorded as a function of the rotation angle of the rotating Dove prism.

Figure 6.7 shows the interference at the output of the interferometer as a function of the rotation angle of one Dove prism. The curves can be interpreted as beating between two beams with optical frequencies that differ by  $\Delta\nu = lF$ , where  $F$  is the rotation frequency of the beam that has been passed through the rotating Dove prism, and therefore present a verification<sup>5</sup> of the rotational Doppler shift for light beams with helical phase fronts.

The work described in this section has been published in ref. [26].

## 6.4 Rotational Doppler effect for general light beams

The previous sections are concerned with the uniform rotation of the polarisation and the uniform rotation of the field structure of a light beam. It was found that a frequency shift results in the case of uniform rotation of a spin eigenstate or an orbital angular momentum eigenstate. In this section the rotation of simultaneous eigenstates of spin and orbital angular momentum is examined. The question arises whether the effect on the frequency spectrum will be a frequency splitting, one combined frequency shift, or something else. This section is the last in this series of sections on rotational Doppler shifts, as it discusses the effect of uniform rotation of an arbitrary monochromatic light beam on its frequency spectrum. This theory of the rotational Doppler effect for general

---

<sup>5</sup>In a strict sense it is merely the *modulus* of the phase difference between the two light beams, as a function of the rotation angle of the rotating Dove prism, that can be inferred from the interferograms in fig. 6.7. That uniform rotation of a Dove prism can indeed lead to a shift in the frequency of a light beam passing through it is demonstrated more directly in the experiment in the following section. This implies that the phase of a light beam passing through a Dove prism is indeed linearly dependent on the rotation angle of the Dove prism.

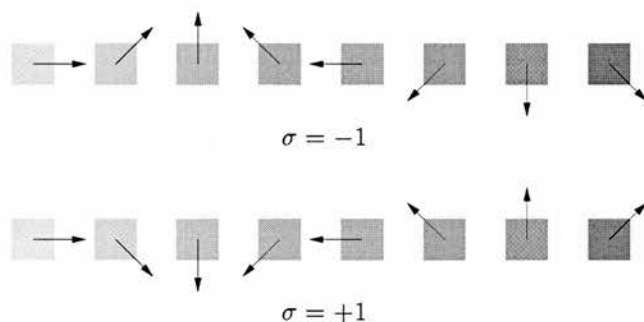


Figure 6.8: Correspondence between the gray-scale representation of the phase and the direction of the electric field vector at time  $t = 0$ . The cases  $\sigma = \pm 1$  are those of right/left-hand circularly polarised light, respectively.

light beams also offers a rare example of intuitive understanding of the way in which spin and orbital angular momentum act together.

In the last section, phase cross-sections with an azimuthal dependence of the form  $l\phi$  were studied. Fig. 6.3 shows a representation of phase cross-sections of this type. In order to include polarisation into this treatment, it is useful to study cross-sections of the electric field. Using fig. 6.8, which relates absolute phase to the absolute direction of the electric field at the same point for left-handed ( $\sigma = -1$ ) and right-handed ( $\sigma = +1$ ) circular polarisation, the electric field associated with phase cross-sections can be visualized (fig. 6.9). Note that, although the underlying phase pattern has an  $l$ -fold rotational symmetry, the pattern formed by the electric field has an  $(l + \sigma)$ -fold rotational symmetry<sup>6</sup>.

It is possible to relate these field cross-sections to “exotic” polarisation states. For example, superposition of two Laguerre-Gaussian beams with the parameters  $l = 1, \sigma = -1$  and  $l = -1, \sigma = 1$  with different relative phases can create Laguerre-Gaussian beams in *radial* [70] and *azimuthal* [71] polarisation states.

Fig. 6.10 shows the time evolution during one optical cycle of the phase and electric field pattern for a circularly polarised light beam with an azimuthal phase dependence of the form  $l\phi$ , with  $l = 2$  and  $\sigma = 1$ . It can be seen that,

<sup>6</sup>This situation might be familiar from the following children’s game: one of two similar coins is rolled along the edge of the other, stationary, coin. While the moving coin performs one rotation with respect to the coin at rest, it performs two rotations around its own axis.

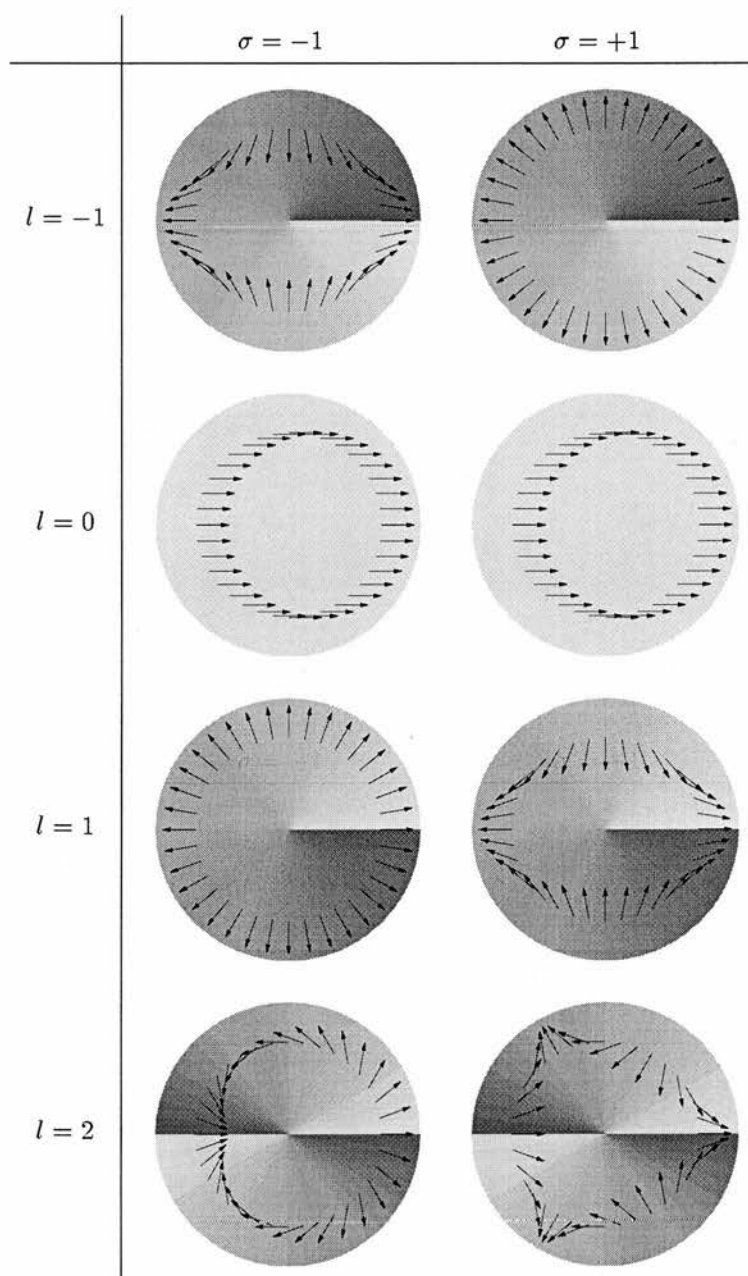


Figure 6.9: Gray-scale representations of phase cross-sections of the form  $\exp(il\phi)$  (see Fig. 6.3), with superimposed electric field vectors for left- ( $\sigma = -1$ ) and right-handed ( $\sigma = +1$ ) circularly polarised light.

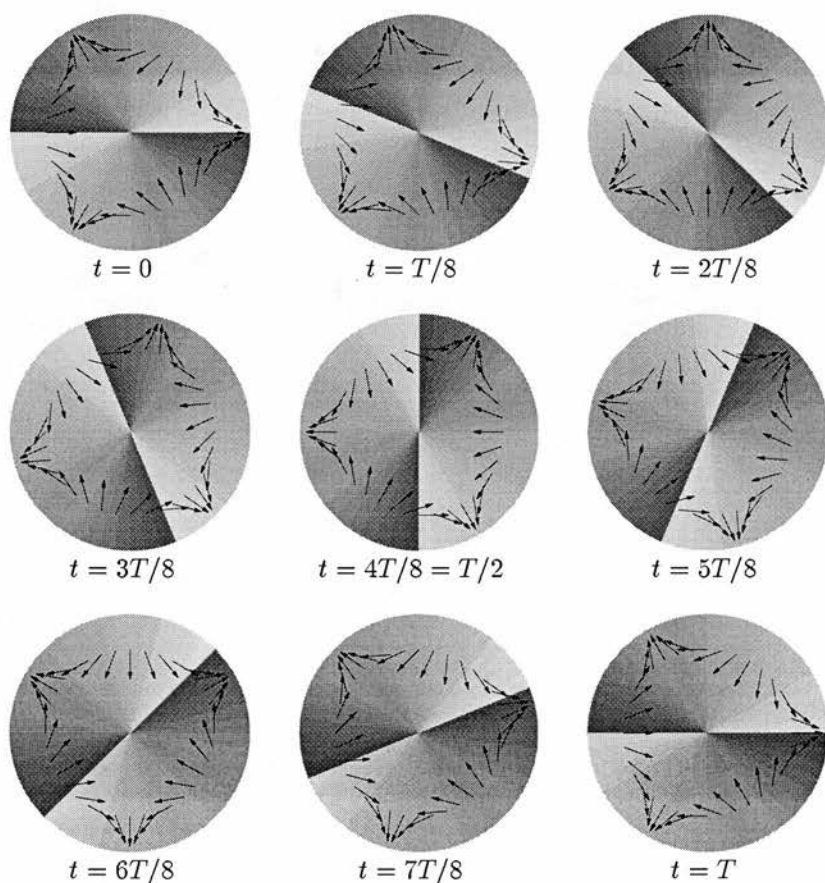


Figure 6.10: Time evolution over one optical cycle of period  $T$  of the cross-section through the electric field in a circularly polarised light beam with an azimuthal phase dependence of the form  $l\phi$  with parameters  $l = 2$  and  $\sigma = 1$ . Note that, while the phase pattern performs  $1/l$  of a full rotation, the electric field distribution performs  $1/(l + \sigma)$  of a full rotation.

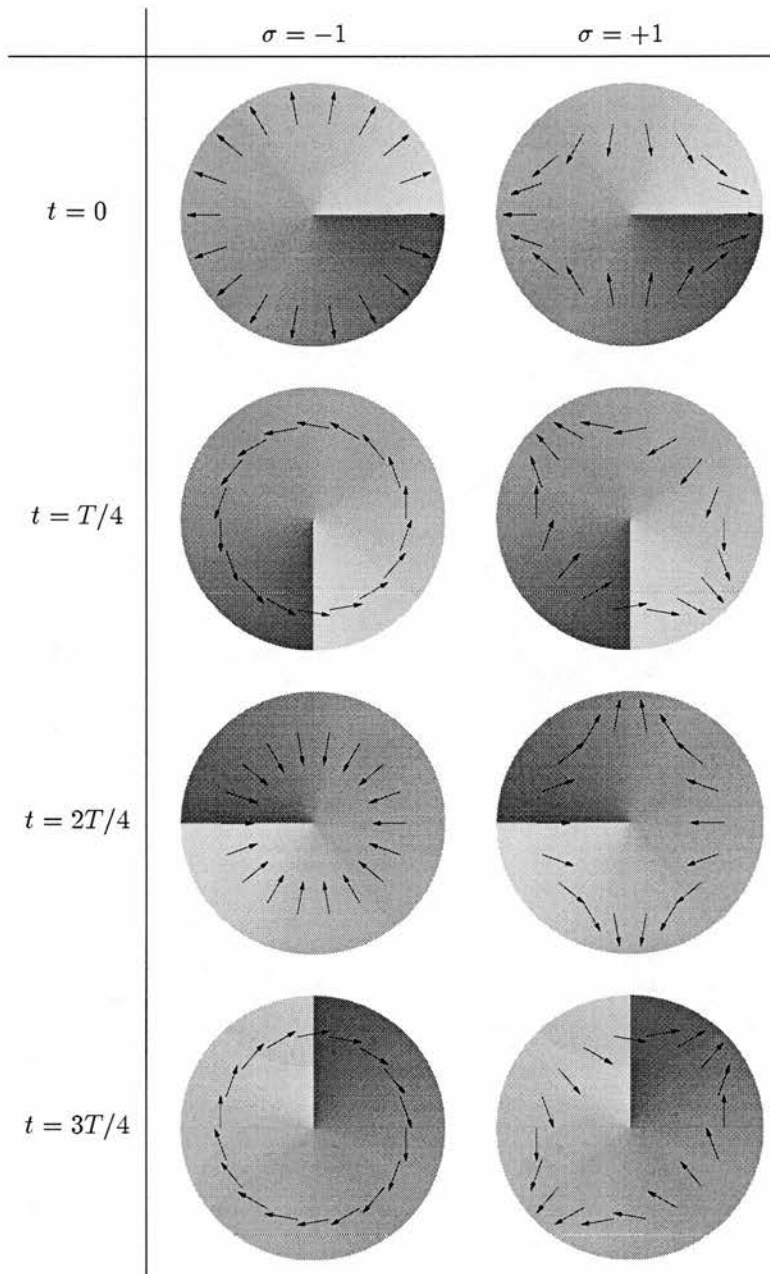


Figure 6.11: Comparison of the time evolution over one optical cycle of an electric field cross-section through left- ( $\sigma = -1$ ) and right-handed ( $\sigma = +1$ ) circularly polarised light beams with an azimuthal phase dependence of the form  $l\phi$  for  $l = 1$ .

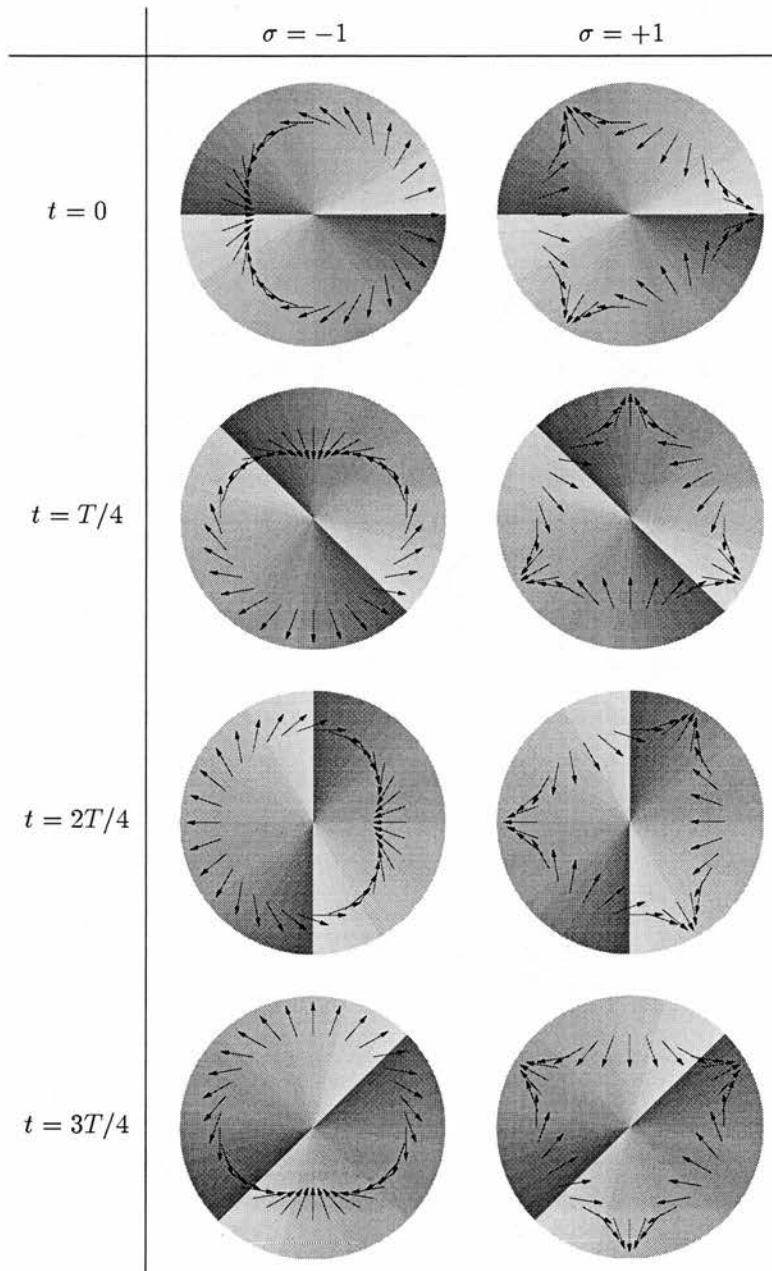


Figure 6.12: Comparison of the time evolution over one optical cycle of an electric field cross-section through left- ( $\sigma = -1$ ) and right-handed ( $\sigma = +1$ ) circularly polarised light beams with an azimuthal phase dependence of the form  $l\phi$  for  $l = 2$ .

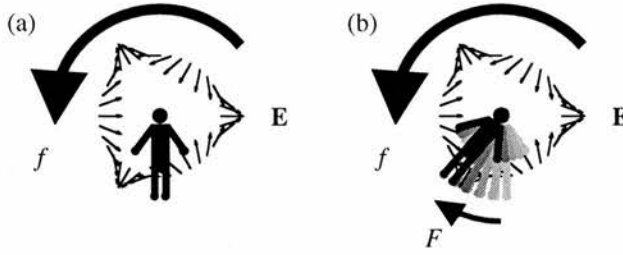


Figure 6.13: Rotational Doppler shift of a circularly polarised beam with an azimuthal phase factor of the form  $\exp(il\phi)$ . (a) An observer at rest sees the cross-section through the electric field of the beam rotate at frequency  $f = \nu/(l + \sigma)$ . (b) Additional rotation of the beam relative to the observer shifts the frequency measured by the observer.

for any fixed position in the pattern, the phase and corresponding field vector go through one full cycle. At the same time, the pattern formed by the phase rotates through  $1/2$  rotation, while the pattern formed by all the electric field vectors along the circle rotates through  $1/3$  rotation. In general, during one optical cycle the phase pattern rotates through  $1/l$  of a full rotation while the electric field pattern rotates through  $1/(l + \sigma)$  of a full rotation (fig. 6.11 and fig. 6.12). Vice versa, during a full rotation of such a beam with respect to an observer, which implies rotation of the electric field structure and not merely the phase structure, the field vectors and corresponding phase go through  $(l + \sigma)$  full phase cycles. Uniform rotation of such a light beam at rotation frequency  $F$  with respect to an observer (fig. 6.13) therefore imparts a frequency shift

$$\Delta\nu = (l + \sigma)F \quad (6.15)$$

to the beam. This rotational Doppler shift of simultaneous eigenfunctions of both the spin and the orbital angular momentum operator is the sum of the rotational Doppler shifts (6.8) and (6.13). It is, of course, also the sum of the equivalent equations (6.9) and (6.14), and as such can be written as

$$\Delta\nu = \frac{\delta J \cdot \omega}{2\pi\hbar}, \quad (6.16)$$

where  $\delta J = \delta S + \delta L$  is the sum of spin and orbital angular momentum, and therefore total angular momentum<sup>7</sup>, per photon in the beam. As before,  $\omega =$

<sup>7</sup>Please note that  $\delta J = \hbar j = \hbar\sigma + \hbar l$  is not the eigenvalue of the total angular momentum

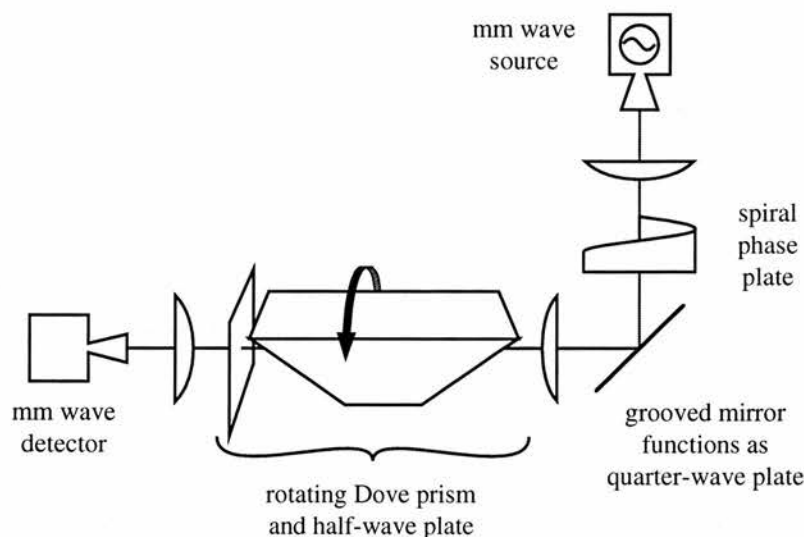


Figure 6.14: Experimental set-up for the measurement of the rotational frequency shift for light with spin and orbital angular momentum. The source is frequency-locked to a frequency counter, which is referenced to another frequency counter that measures the frequency at the detector.

$2\pi F$  is the angular velocity of the rotation of the beam with respect to the observer. This equation is completely analogous to equations (6.7), (6.9) and (6.14).

Every monochromatic light beam can be described as a superposition of circularly polarised Laguerre-Gaussian modes, simultaneous eigenfunctions of spin and orbital angular momentum. Upon uniform rotation, every circularly polarised LG component is shifted individually according to equation (6.15). The rotational Doppler shift will therefore produce a “fan” of frequencies described by the original optical frequency,  $\nu$ , plus integer multiples of the rotation frequency,  $F$ . If a monochromatic light beam of frequency  $\nu$  is rotated at frequency  $F$ , its frequency spectrum can contain any frequency

$$\nu_j = \nu + jF, \quad j \in \{0, \pm 1, \pm 2, \dots\}. \quad (6.17)$$

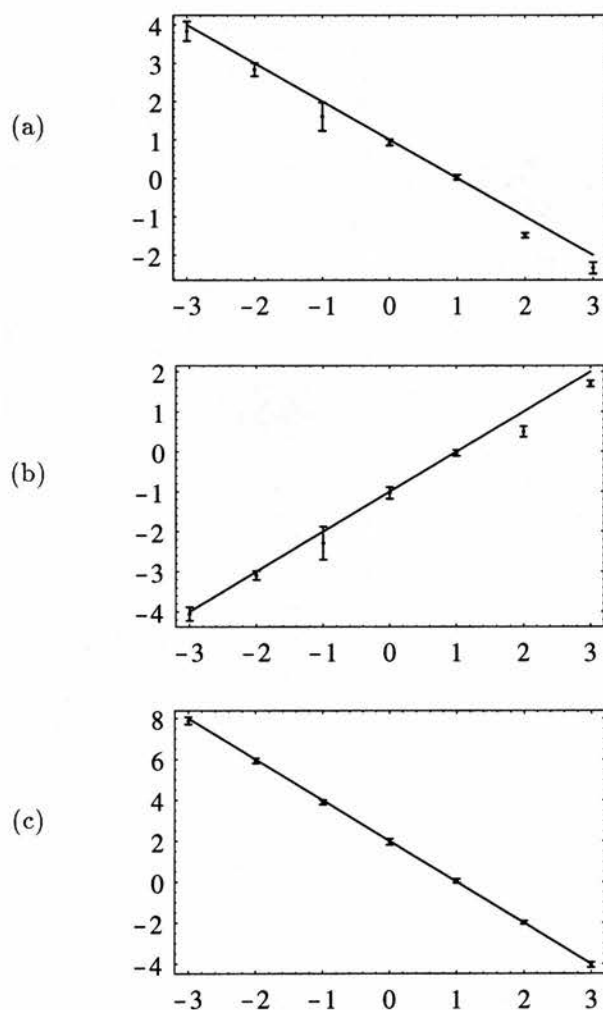


Figure 6.15: Frequency shift  $\Delta\nu$  in Hz (vertical axis) vs azimuthal mode index  $l$  (horizontal axis) for  $\sigma = -1$ . The frequency shift is between (a) clockwise rotation at frequency  $F = -1\text{Hz}$  and no rotation ( $F = 0$ ), (b) anti-clockwise rotation ( $F = 1\text{Hz}$ ) and no rotation, (c) clockwise and anti-clockwise rotation of Dove prism and half-wave plate. The bars correspond to experimental measurements, the solid lines correspond to the theoretical result  $\Delta\nu = (l + \sigma)F$ .

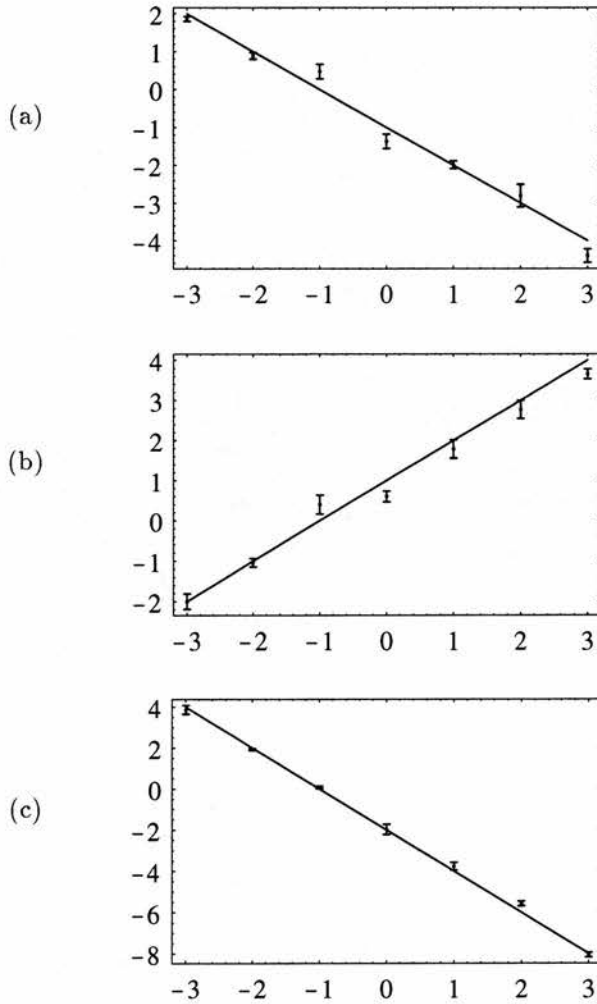


Figure 6.16: Frequency shift  $\Delta\nu$  in Hz (vertical axis) vs azimuthal mode index  $l$  (horizontal axis) for  $\sigma = +1$ . The frequency shift is between (a) clockwise rotation at frequency  $F = -1$  Hz and no rotation ( $F = 0$ ), (b) anti-clockwise rotation ( $F = 1$  Hz) and no rotation, (c) clockwise and anti-clockwise rotation of Dove prism and half-wave plate. The bars correspond to experimental measurements, the solid lines correspond to the theoretical result  $\Delta\nu = (l + \sigma)F$ .

### 6.4.1 Experiment

An experiment was performed to measure the rotational Doppler shift, equation (6.15). The setup is outlined in fig. 6.14. The collimated output from a Gunn diode source oscillating at  $\nu = 94\text{GHz}$ , which corresponds to a wavelength of  $\lambda = 3\text{mm}$ , was passed through a spiral phase plate [25], which imposed an azimuthal phase structure of the form  $\exp(il\phi)$  on the linearly polarised beam. The beam was circularly polarised by reflection from a mirror with  $\lambda/8$  deep grooves, which acted as quarter-wave plate [72]. The beam was then passed through a Dove prism and half-wave plate, both of which were rotating about the beam axis with frequency  $F/2$ . The effect of the rotating Dove prism on the the phase cross-section of the beam was a mirror reversal and rotation with frequency  $F$ , the effect of the rotating half-wave plate on the polarisation of the beam was also a mirror reversal and rotation with frequency  $F$ . Therefore the combination of rotating Dove prism and rotating half-wave plate produces a beam that is rotating with all its physical aspects. This rotating beam was focussed into a detector, which was connected to a frequency counter. This frequency counter was sharing an oscillator crystal with another frequency counter, which measured the frequency of the Gunn diode source and supplied the Gunn diode oscillator with a feed-back signal to lock it to a constant frequency.

Figures 6.15 and 6.16 show the measured differences between the frequency of the rotating beam and that of the non-rotating beam. These frequency shifts are in complete agreement with the theoretical predictions, equation (6.15).

The work described in this section was published in ref. [27].

## 6.5 Rotational Doppler effect and translational Doppler effect of a rotating object

The rotational Doppler effect should not be confused with the Doppler effect due to the translational velocity of the surface of rotating objects. Unlike this translational Doppler shift for rotating objects, which is maximal in the plane of rotation, the rotational Doppler shift is maximal in the direction of the angular operator,  $\hat{J}$ .

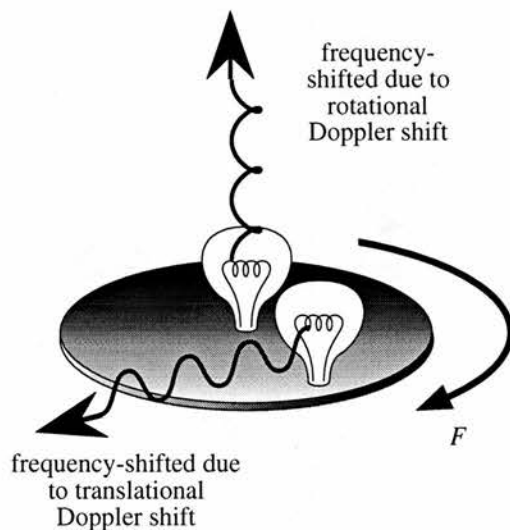


Figure 6.17: Translational and rotational Doppler effects for a rotating light source.

velocity vector where the translational Doppler shift is zero (fig. 6.17).

## Chapter 7

# Sphere of first-order modes

### 7.1 Introduction

In chapters 1 and 6 of this thesis the strong analogies between spin and orbital angular momentum have been demonstrated. By constructing the sphere of first-order modes, an analog of the Poincaré sphere for light beams with orbital angular momentum, this chapter introduces another analogy of this kind.

### 7.2 Poincaré sphere and the sphere of first-order modes

The polarisation state of a monochromatic light beam can be completely characterised in terms of the Stokes parameters [73]

$$p_1 = \frac{I_{0^\circ} - I_{90^\circ}}{I_{0^\circ} + I_{90^\circ}}, \quad (7.1)$$

$$p_2 = \frac{I_{45^\circ} - I_{135^\circ}}{I_{45^\circ} + I_{135^\circ}}, \quad (7.2)$$

$$p_3 = \frac{I_{\text{right}} - I_{\text{left}}}{I_{\text{right}} + I_{\text{left}}}, \quad (7.3)$$

where  $I_{0^\circ}$ ,  $I_{45^\circ}$ ,  $I_{90^\circ}$ , and  $I_{135^\circ}$  are the intensities of the light recorded through various orientations of linear polarisers, and  $I_{\text{right}}$  and  $I_{\text{left}}$  are the intensities of the circularly polarised components in the beam. For a completely polarised

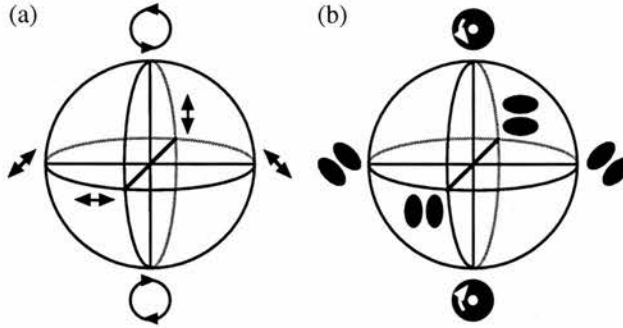


Figure 7.1: Poincaré sphere (a) and sphere of first-order modes (b). Some commonly encountered polarisation states and modes (see fig. 7.2) are indicated.

light beam the squares of the Stokes parameters add up to unity, i.e.

$$p_1^2 + p_2^2 + p_3^2 = 1. \quad (7.4)$$

Consequently, the Stokes parameters are the Cartesian coordinates of a space in which any completely polarised light beam is represented by a point on a sphere with unit radius around the origin. This sphere is known as the Poincaré sphere (fig. 7.1(a)) and has proved to be a useful tool in dealing with transformations of the polarisation state [73].

The north and south poles of the Poincaré sphere represent the spin eigenstates, left- and right-handed circularly polarised light, respectively. Any state of complete polarisation, and therefore any point on the Poincaré sphere, can be described as a superposition of left- and right-handed circular polarisations. For example, linearly polarised light is a superposition of equal intensities of left- and right-handed circularly polarised light; the relative phase of the superposition determines the orientation of the linear polarisation.

An analogous sphere can be constructed for superpositions of left- and right-handed Laguerre-Gaussian modes with azimuthal phase terms of  $\exp(\pm i\phi)$ , respectively, which are orbital angular momentum eigenstates. These Laguerre-Gaussian modes (fig. 7.2) are denoted  $LG_0^{+1}$  and  $LG_0^{-1}$  and possess an orbital angular momentum of  $\pm\hbar$  per photon, respectively (see section 1.4.2). Their superpositions form structurally stable beams ('modes') of mode order  $N = 1$  [74] (see also chapter 5). As therefore every point on the Poincaré-sphere analog cor-

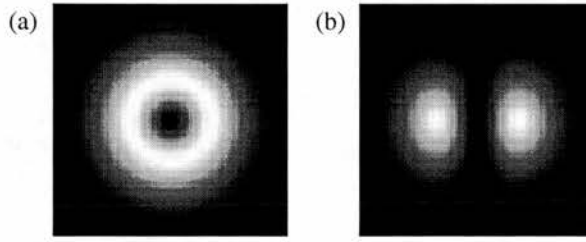


Figure 7.2: Intensity cross-section of  $LG_0^{\pm 1}$  modes (a) and a  $HG_{1,0}$  mode (b). The modes  $LG_0^{-1}$  and  $LG_0^{+1}$  differ only in the handedness of their azimuthal mode structure.

responds to a mode of order one, and also every mode of order one corresponds to a point on the Poincarè-sphere analog, this sphere is referred to as the *sphere of 1st-order modes*. For example, a superposition of equal intensities of left- and right-handed Laguerre-Gaussian modes forms a Hermite-Gaussian mode with indices  $m = 1$  and  $n = 0$ , denoted  $HG_{1,0}$ , which is of order  $N = m + n = 1$  [13]. The relative phase of the superposition determines the orientation of the mode.

In analogy to the Stokes parameters, a set of parameters,  $o_1, o_2, o_3$ , can be defined for the newly proposed sphere. These are

$$o_1 = \frac{I_{HG_{1,0}^{0^\circ}} - I_{HG_{1,0}^{90^\circ}}}{I_{HG_{1,0}^{0^\circ}} + I_{HG_{1,0}^{90^\circ}}}, \quad (7.5)$$

$$o_2 = \frac{I_{HG_{1,0}^{45^\circ}} - I_{HG_{1,0}^{135^\circ}}}{I_{HG_{1,0}^{45^\circ}} + I_{HG_{1,0}^{135^\circ}}}, \quad (7.6)$$

$$o_3 = \frac{I_{LG_0^1} - I_{LG_0^{-1}}}{I_{LG_0^1} + I_{LG_0^{-1}}}, \quad (7.7)$$

where  $I_{HG_{1,0}^\alpha}$  stands for the intensity of the Hermite-Gaussian  $m = 1, n = 0$  mode at angle  $\alpha$  present in the beam, and  $I_{LG_0^{\pm 1}}$  stands for the intensities of the Laguerre-Gaussian  $l = \pm 1, p = 0$  modes in the beam. Writing all the intensities as the square of the moduli of the corresponding mode functions, and expanding all the mode functions in terms of Laguerre-Gaussian  $l = \pm 1, p = 0$  mode functions [13], it can be shown that

$$o_1^2 + o_2^2 + o_3^2 = 1. \quad (7.8)$$

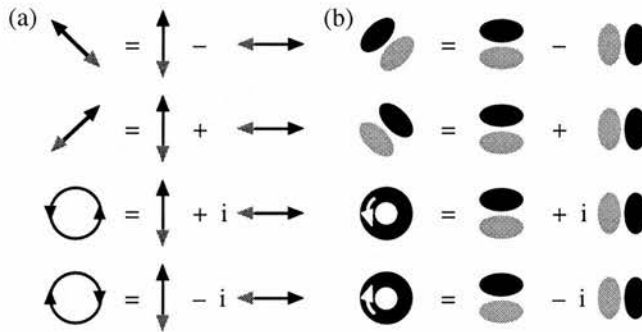


Figure 7.3: Decompositions of various polarisation states and first-order modes in terms of orthogonal linear polarisation states (a), and orthogonal Hermite-Gaussian  $m = 1$ ,  $n = 0$  modes (b), respectively. The black and grey shading indicates the relative phase of the components.

### 7.3 Wave plates and mode converters

Starting with left-hand circularly polarised light, a quarter-wave plate transforms the light to a linear polarisation at  $45^\circ$  to the axis of the wave plate. On the Poincaré sphere, this is represented by a move from the north pole to a point on the equator, the longitude of which depends on the orientation of the linear polarisation [63]. Rotation of the wave plate through an angle  $\alpha$  advances the longitude of the transformation by an angle  $2\alpha$ . Similarly, a half-wave plate transforms from left-handed to right-handed circular polarisation. This is represented by a move from pole to pole along a great circle, the longitude of which depends on the rotation angle of the wave plate [63]. This can be seen by considering the half-wave plate as two identical quarter-wave plates: as before, the state after the first wave plate is represented on the equator and its longitude depends on the rotational alignment of the fast axis of the wave plate. Rotation of the wave plate through an angle  $\alpha$  advances the longitude of the trajectory taken during the transformation by  $2\alpha$ .

In a similar fashion to a birefringent wave plate, which controls the relative phase between two linear polarisations at  $90^\circ$  to each other, the relative phase of two Hermite-Gaussian  $m = 1$ ,  $n = 0$  modes at  $90^\circ$  to each other (fig. 7.3) can be controlled using an arrangement of cylindrical lenses. Beijersbergen

*et al.* [13] detailed the design and operation of cylindrical lens mode converters that utilise changes in relative Guoy phase to transform Hermite-Gaussian into Laguerre-Gaussian modes and vice versa. Both “ $\pi$  converters” and “ $\pi/2$  converters” exist which perform tasks analogous to half-wave and quarter-wave plates, respectively. The analogy is best appreciated by considering both the wave plates and the cylindrical lenses as means of introducing phase shifts between two orthogonal components of the beam.

## 7.4 Evolving geometric phase

In 1979 Garetz and Arnold [75] demonstrated that a frequency shift results when circularly polarised light is transmitted through a rotating half-wave plate. The shift is equal to twice the rotational frequency of the wave plate. Although simply explained as a rotational Doppler shift for light with spin angular momentum (see chapter 6), a similar experiment was also performed and explained in terms of a dynamic geometric (or Berry) phase by Simon *et al.* [63]. In their experiment, a combination of wave plates was used to transform the polarisation state of the light around a closed loop on the Poincaré sphere. The resulting geometric phase shift was equal to half the solid angle enclosed by the loop and in addition to the constant phase shift due to the optical thickness of the components. Uniform rotation of one of the wave plates gave a constant rate of change of the enclosed solid angle, resulting in a frequency shift of the light beam.

Recently a similar experiment was performed with light beams containing orbital angular momentum [26] (see section 6.3). On transmission through a rotating  $\pi$  converter, the frequency of a  $\text{LG}_0^{\pm 1}$  mode is shifted by twice the rotation frequency of the  $\pi$  converter. The mode transformation in the  $\pi$  converter can be interpreted as a geometric-phase effect [74]; the frequency shift that occurs on transmission through a rotating  $\pi$  converter can be interpreted as this geometric phase evolving in time.

Figure 7.4 illustrates the equivalence of the geometric phase shift for light beams containing either spin or orbital angular momentum after transmission through two half-wave plates or two  $\pi$  converters, respectively. In both cases,

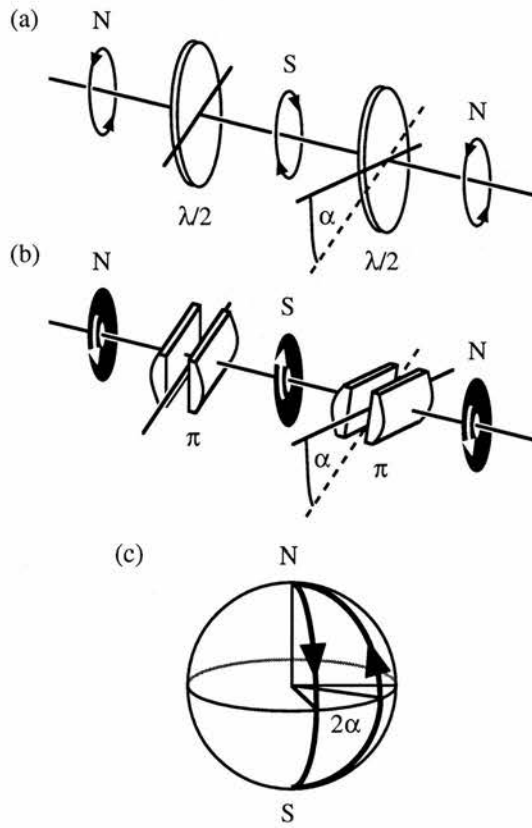


Figure 7.4: Generation of evolving geometric phases for light beams containing spin (a) and orbital angular momentum (b), respectively. (c) shows the respective path taken on the Poincaré sphere or sphere of first-order modes.

the geometric phase shift is equal to half the solid angle enclosed by the loop on the surface of the respective spheres. Therefore, for a change in the angular orientation between the two optical components of  $\alpha$ , the resulting geometric phase shift is  $2\alpha$ . Thus, in both cases, the frequency of the light beam is shifted by twice the rotation frequency of the optical component.

The work described in this chapter has been published in ref. [76].

## Chapter 8

# Fractal resonator modes

### 8.1 Self-similar fractals and multiple reduction copy machines

Self-similarity is not only one of the fundamental design principles of the natural world, encountered in objects as different as ferns and clouds [77, 78]; it is also the basis of important applications such as fractal image compression [79]. An example of a self-similar shape is any output of a so-called multiple reduction copy machine (MRCM) [80], a (fictitious) photo-copier that places a number of reduced copies of the input page at different positions on the output page (fig. 8.1). When repeatedly being fed back, the output of the MRCM shown in fig.

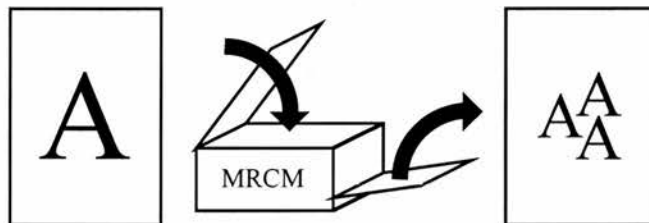


Figure 8.1: Principle of the multiple reduction copy machine (MRCM). In this example, three half-size copies of the image on the input page, centered on the corners of an equilateral triangle, are placed on the output page.

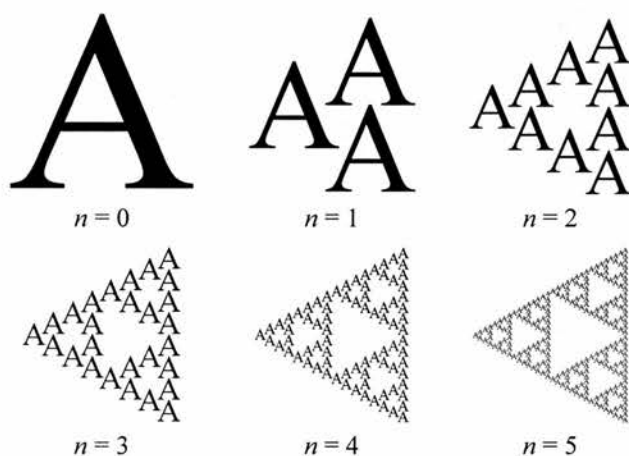


Figure 8.2: Output from the multiple reduction copy machine in fig. 8.1 after  $n$  feedback iterations.

8.1 becomes an increasingly accurate approximation to a fractal known as the Sierpinski gasket (fig. 8.2). Other classical fractals, such as the Cantor set, the Sierpinski carpet, and the Koch curve, are associated with different MRCMs [80].

## 8.2 Previous optical realisations of multiple reduction copy machines

Optical realisations of this “process of successive microscopic refinement” [82] have been reported before. In light-hearted figure 4.27 in ref. [83], a multiple reduction copy machine is sketched as comprising what appear to be simply four pairs of lenses, each of which images the input page onto the same piece of photographic paper, which forms the output. A more serious, and indeed patented, all-optical multiple reduction copy machine with feedback is described in ref. [81] (fig. 8.3). Such a setup might be called a *fractal displayer*, and allows very versatile multiple imaging.

The idea behind this chapter is to treat fractal displayers, from which any incoherent image intensifiers have been removed, as optical resonators. Instead of a number of arms like the fractal displayer in fig. 8.3, in simple cases parallel

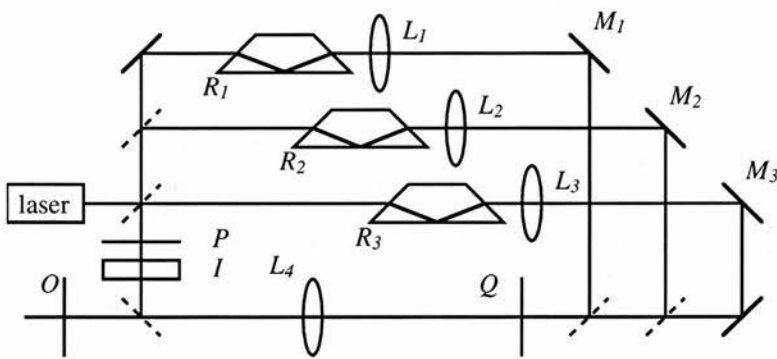


Figure 8.3: All-optical fractal display as described in ref. [81]. The combination of rotation prism  $R_i$ , imaging lens  $L_i$ , and movable mirror  $M_i$  allows the light passing through arm  $i$  to be imaged from plane  $P$  into plane  $Q$ , arbitrarily rotated, magnified and translated, but with its handedness reversed by the imaging process. A lens  $L_4$  images plane  $Q$  back into plane  $P$ , thereby returning the image back to its original handedness and completing the feedback loop. The image in plane  $P$  can also be seen in plane  $O$ . An initial light pulse is provided by a laser, an image intensifier  $I$  compensates for round-trip losses.

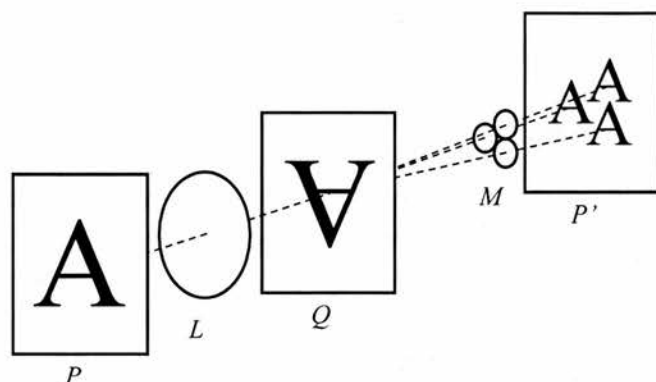


Figure 8.4: Lens configuration for multiple reduction imaging.

lenses can be used for multiple imaging. The action of all those lenses together can be performed by a single hologram. In the following section a ring resonator which contains only a single hologram and no additional lenses, but has a lowest-loss eigenmode which is a diffraction-limited approximation to the so-called Sierpinski gasket fractal, is described. Slightly modified resonators would have eigenmodes which are approximations to other “classic fractals”. Inclusion of a coherent gain medium could turn such resonators into *fractal lasers*.

### 8.3 A resonator with a Sierpinski-gasket eigenmode

Fig. 8.4 shows an analog of the multiple reduction copy machine in fig. 8.1, a lens configuration for multiple reduction imaging of the intensity pattern in a plane  $P$  onto a plane  $P'$ . A lens  $L$  creates a vertically and horizontally flipped image of the intensity pattern at  $P$  in an intermediate plane  $Q$ , which three lenses, collectively marked  $M$  in fig. 8.4, then image three times onto the plane  $P'$ , thereby flipping the individual patterns back into their original orientation.

The image in the plane  $P'$  can be continuously fed back by folding the optical axis with a number of mirrors such that the object plane  $P$  is identical with the image plane  $P'$  (fig. 8.5(a)), thus creating a ring resonator with the tendency to create a fractal intensity distribution in the plane  $P$ .

Without its lowest-loss mode losing its overall shape, the resonator in fig.

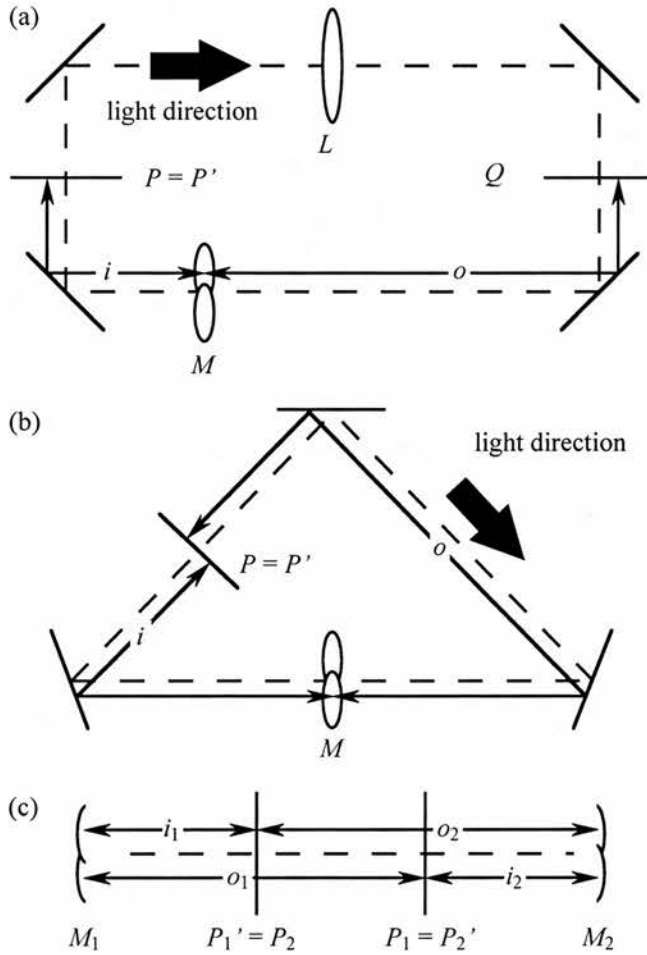


Figure 8.5: Three optical resonators with Sierpinski gasket eigenmodes. (a) represents a folded version of the lens system in fig. 8.4. In (b) the flipping of the cross section in the paper plane, which is performed by the lens  $L$  in (a), is achieved by an odd number of reflections per round-trip. As the eigenmode of the resonator is symmetric in the direction normal to the paper plane, it is not affected by not flipping the cross-section in that direction. (c) outlines a standing-wave design. Each of the two end mirrors  $M_j$  ( $j = 1, 2$ ), both of which are similar combinations of three spherical mirrors, reduces the plane  $P_j$  three times into the corresponding plane  $P'_j$ .

8.5(a) can be simplified. As the lowest-loss mode is symmetric in that direction, the vertical flipping of the light before passing through the three lenses  $M$ , performed by the lens  $L$ , can be dispensed with. The important horizontal flipping is achieved in fig. 8.5(b) by an odd number of reflections off the resonator mirrors, in fig. 8.5(c) by effectively combining two cavities which are anti-symmetric in that direction. Please note that it is the lack of symmetry in the horizontal direction of the Sierpinski gasket, used as example throughout this paper, that necessitates the horizontal flipping of the light; other fractals, such as the Cantor set and the Sierpinski carpet, can arise in resonators even simpler than those shown in fig. 8.5.

### 8.3.1 Numerical calculation of the eigenmodes

This section is devoted to wave-optical simulations of light passing through resonators of the type outlined in fig. 8.5(b) and (c), whereby one round trip through a resonator of type (c) corresponds to two round trips through a resonator of type (b). As the magnitude of the magnification of each of the three imaging processes has to be  $1/2$  in the case of the Sierpinski gasket, so has the magnitude of the ratio of the image distance  $i$  to the object distance  $o$ . The lens equation,  $1/i + 1/o = 1/f$ , implies an object distance of  $o = 3f$  and an image distance of  $i = 3/2f$ , and therefore a resonator length of  $l = o + i = 9/2f$ . A circular aperture of diameter  $d$  in a plane just in front of the three lenses  $M$  provided the mechanism for diffraction loss in the resonator. The specific way in which the three lenses  $M$  were combined is outlined in fig. 8.6. All simulations were performed for light of wavelength  $\lambda = 633\text{nm}$ . An area of  $3\text{mm} \times 3\text{mm}$  of the cross-section of a light beam was represented in the computer by the corresponding amplitude values on a  $2048 \times 2048$  grid. The change in cross-section experienced by a light beam during one round-trip through the resonator was calculated in five stages:

1. Starting with the cross-section in the plane  $P$ , the cross-section in the plane just before the circular aperture was calculated. This was done by propagating the initial cross-section a distance  $o$  through free space, using an algorithm based on a plane wave decomposition of the field [50]. Each mirror flips the cross-section horizontally, so the effects of the two mirrors

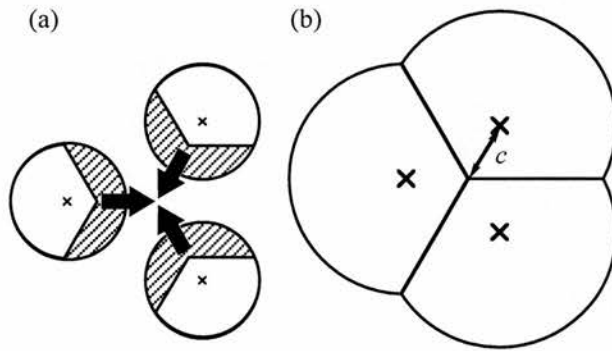


Figure 8.6: Geometry of the combination  $M$  of three lenses. Similar segments (drawn non-shaded in (a)) of three lenses of focal length  $f$  are joined together along the straight edges (b).  $c$  denotes the distance between the centre of the circle and the centres of the individual lenses, marked by crosses.

encountered on this leg of the round trip cancel each other out.

2. The cross-section was truncated according to the circular aperture.
3. The effect of the beam passing through a phase-holographic representation of the combination of three lenses  $M$  was simulated by adding to the local phase of the amplitude distribution the corresponding phase delay induced in the phase hologram.
4. Using the free-space propagation algorithm, the amplitude cross-section a distance  $i$  behind the three lenses  $M$  was calculated.
5. To account for the effect of the mirror encountered on the last leg of the round trip, the cross-section was flipped horizontally. The result is a representation of the beam cross-section in the plane  $P$  after one round trip through the resonator.

Fig. 8.7 shows simulated intensity distributions of a light beam after having passed  $n$  times through the resonator. The vertical direction corresponds to the direction normal to the paper plane in fig. 8.5 (b). The fact that the intensity pattern after  $n = 1$  round trip is flipped vertically when compared to the pattern  $t P'$  in fig. 8.4 is due to the design of the resonator, which, as mentioned earlier, dispenses with the flipping of the beam in that direction. A comparison with fig.

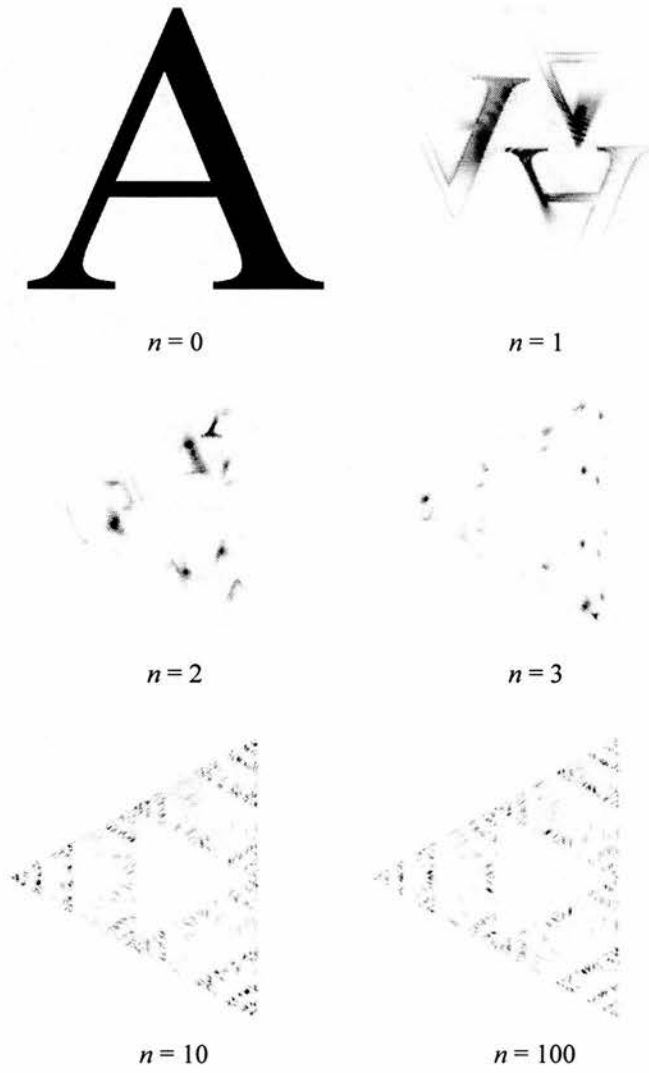


Figure 8.7: Inverted intensity cross-sections in the plane  $P$  after  $n$  round trips through the resonator. The input field corresponds to  $n = 0$ . The figure was calculated for a multiple-imaging element with values  $d = 2\text{mm}$ ,  $c = 0.1\text{mm}$ , and  $f = 5\text{mm}$ .

8.2 shows that the intensity pattern in the plane  $P$  after  $n$  round trips through the resonator differs significantly from the output of the multiple reduction copy machine after  $n$  iterations. Diffraction at the aperture and the shape of the individual lens segments determine the shape and size of each image of every point in the same plane one round trip ago (point spread function). The influence of the tightness of focusing on the size of features in the patterns is illustrated in fig. 8.8, which shows intensity cross-sections after  $n = 100$  round trips through the resonator in the plane  $P$  for different imaging ratios. If losses are ignored, these intensity cross-sections remain essentially unchanged on propagation through the corresponding resonator; they thus represent its lowest-loss mode.

Some properties of the stationary modes due to the finite aperture of the lens segments can be understood in terms of ray optics. Amongst all the rays that pass through a particular lens there is not necessarily one coming from each point in the pattern at  $P$ . This means that the corresponding image of that point would be missing in the intensity pattern at  $P$ . Fig. 8.9 shows cross-sections of the lowest-loss modes of two resonators that differ only in the diameter  $d$  of the aperture. It can be seen that in the mode corresponding to the smaller diameter the corners of the Sierpinski gasket are missing. Another effect arises from some points being passed by more rays than others. As a consequence the intensity varies from point to point. This effect can be seen in Figures 8.7 to 8.9. A mathematical analysis of properties like the scaling behaviour of intensity patterns should therefore treat them as approximations to multifractals, that is fractal sets that have 'shades of grey' associated with them [80].

As a resonator in which lenses (multiply) image one plane onto itself with magnification  $m_1$  with a modulus other than unity, the resonator is necessarily unstable. This is due to the existence of another plane which is imaged onto itself with magnification  $m_2 = 1/m_1$ . Therefore the cross-section in one plane is reduced onto itself, and that in the other plane is magnified. In the case of a single lens the two planes are situated symmetrically on opposite sides of the lens. As it is the loss at the aperture of the lens that balances the constant magnification of the cross-section in one plane, resonators of this type

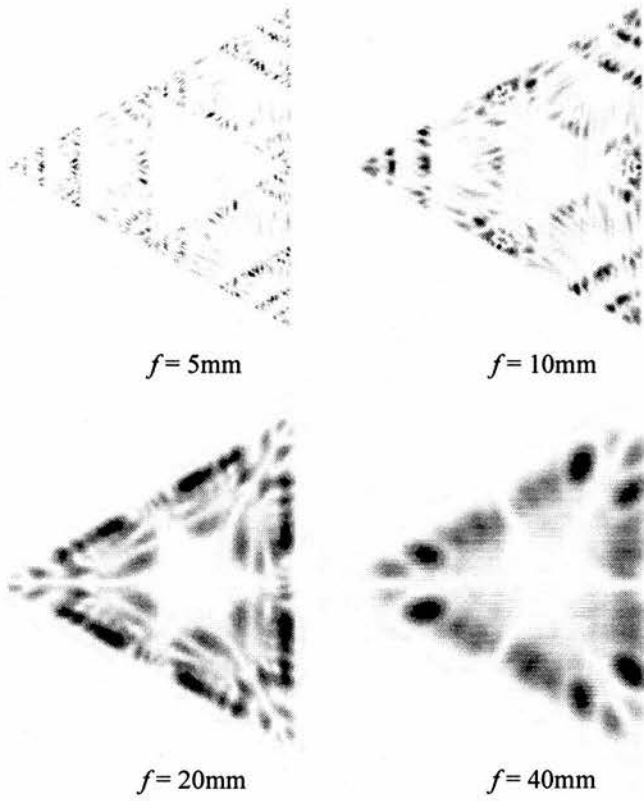


Figure 8.8: Inverted intensity cross-sections in the plane  $P$  after  $n = 100$  round trips through the resonator, calculated for the parameters  $d = 2\text{mm}$ ,  $c = 0.1\text{mm}$ , and different focal lengths  $f$ . As the cavity length  $l$  and the imaging distance  $i$  were chosen accordingly, this corresponds to different imaging ratios.

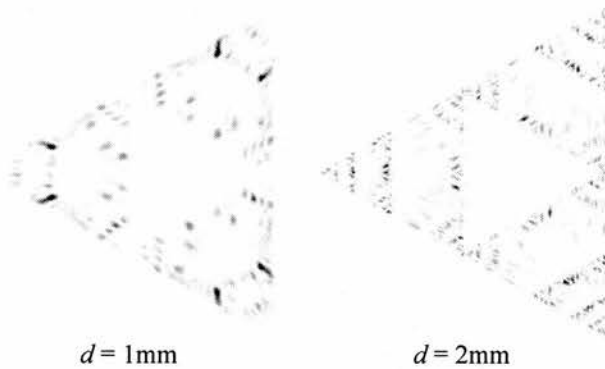


Figure 8.9: Inverted intensity cross-sections of light fields after 100 round trips through resonators with parameters  $c = 0.1\text{mm}$ ,  $f = 5\text{mm}$ , and two different values of the aperture diameter  $d$ . The round-trip loss due to diffraction for these beams is 31.4% ( $d = 1\text{mm}$ ) and 26.6% ( $d = 2\text{mm}$ ).

are necessarily liable to loss and therefore unstable. To illustrate this point, the diffraction loss during one round-trip is given in fig. 8.9. This loss can be further decreased by choosing an appropriate aperture size.

## 8.4 Fractal lasers and atomic resonators

If the round-trip loss in the resonator could be overcome by insertion of an active medium with sufficiently high gain, a laser with *fractal laser modes* would result. Insertion of a field stop at the plane  $P$  could increase the round-trip loss of light travelling around the resonator in the wrong direction and thus decrease pump depletion. Such a laser would provide an interesting object of study from the point of view of fractal optics [84].

The ideas outlined in this chapter could even be applied to atomic optics. Already spherical atomic mirrors continuously re-focussing bouncing atoms [85] can be interpreted as rudimentary atomic resonators. A suitable multiple-imaging mirror instead of the spherical mirror could turn this simple atomic resonator into one that supports fractal modes.

# Appendix A

## Beam propagation program

### A.1 Introduction

The implementation of an algorithm for modelling numerically the propagation of the electric field of any monochromatic beam, given in a plane, through free space into a parallel plane [50] produced an immensely useful computer program. Inclusion of the phase shift induced by thin lenses [86] increased the versatility of the program even further: within the work towards this thesis the program has been used to model the propagation of “propeller beams” (chapter 3), frequency-doubled Laguerre-Gaussian modes (chapter 4), self-imaging beams, spiral-type beams, and structurally stable beams (chapter 5), to numerically find the eigenmodes of cavities with fractal eigenmodes (chapter 8), and to evaluate the performance of the cylindrical-lens mode converter for converting between Hermite-Gaussian and Laguerre-Gaussian modes (chapter 2). The program has also been made available to other researchers in the department, who have used it, among other things, for optimising the design of holograms for the generation of Laguerre-Gaussian modes [30] and for designing a profilometer based on an interferometric measurement of the polarisation of light reflected from a sample [87].

The implementation of the algorithm in the form of a *Mathematica* package allows the program to be used in conjunction with the full versatility of the *Mathematica* programming language [88]. For example, still or animated se-

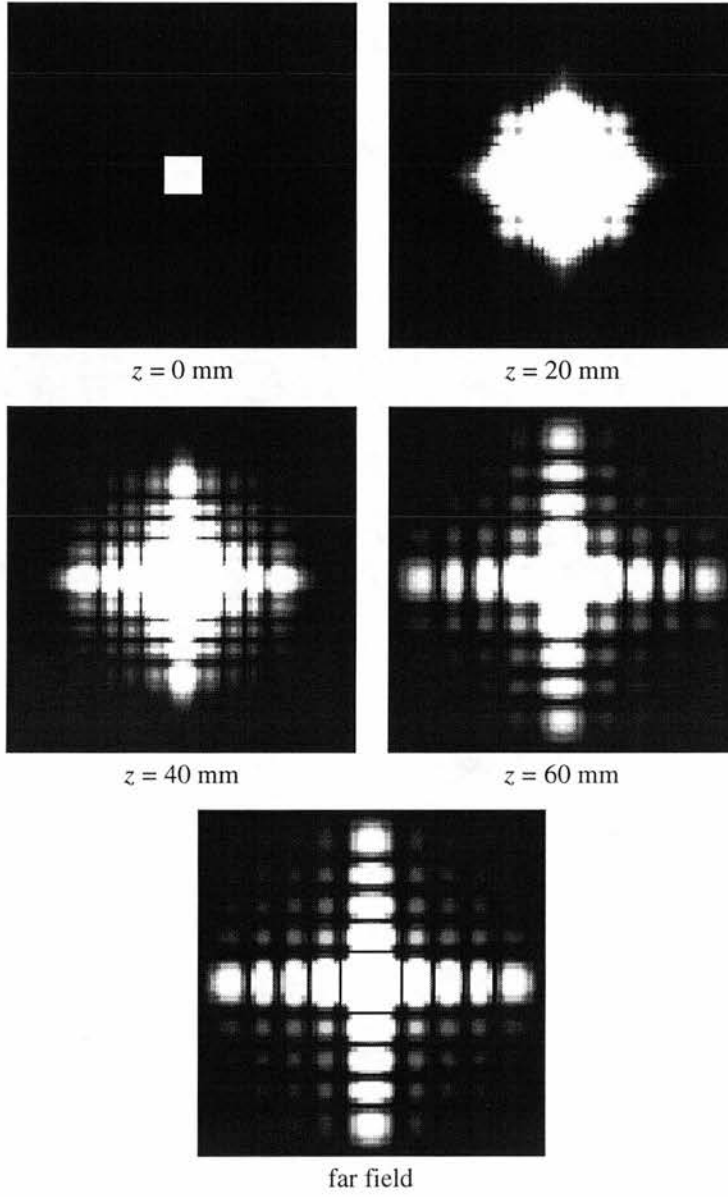


Figure A.1: Modelled intensity distribution, a distance  $z$  behind a plane with a square flat-topped intensity profile.

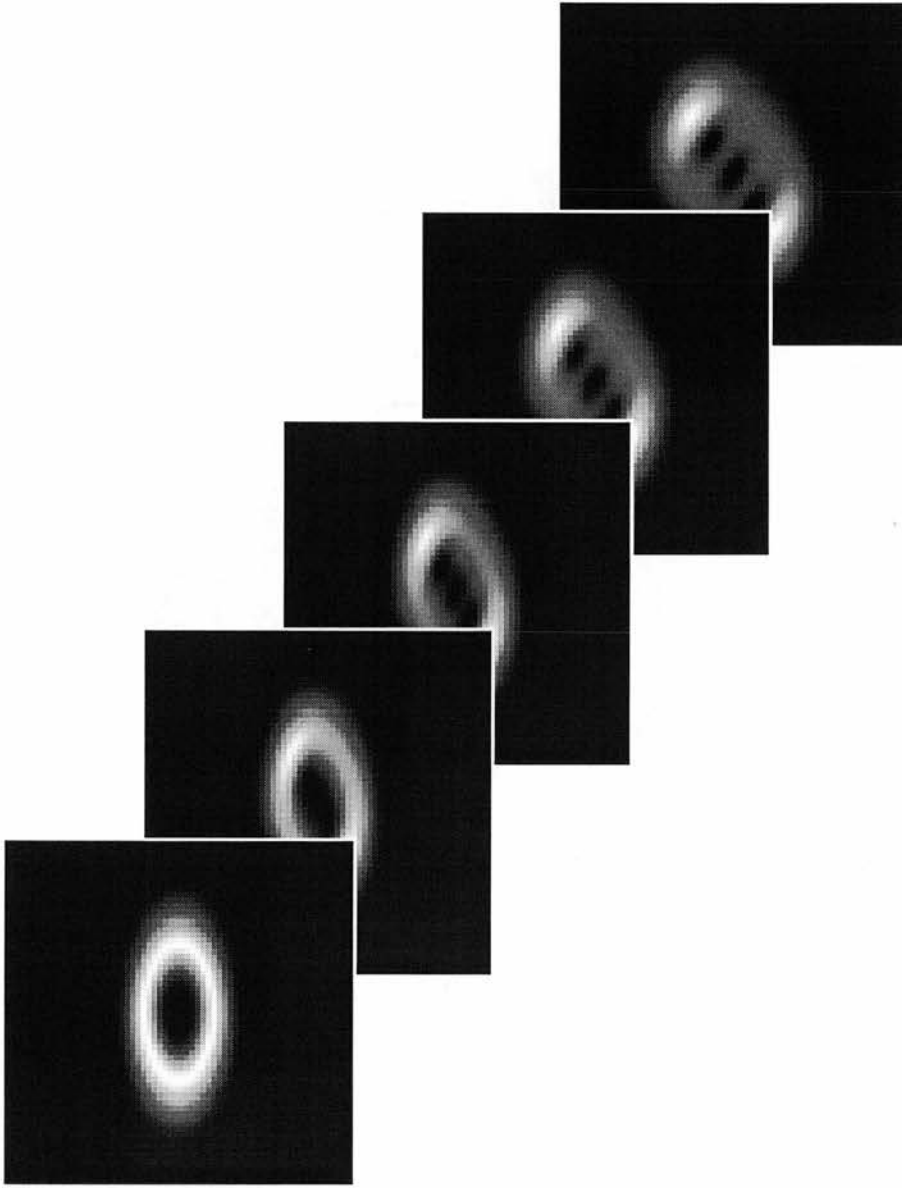


Figure A.2: Modelled propagation of a LG beam that, in the plane of the beam waist, is stretched in the  $y$  direction by a factor of two. The bottom left picture shows the intensity cross-section in the plane of the beam waist, the other pictures are cross-sections in equidistant planes behind the beam waist. As can be seen from fig. A.3, the phase singularity of charge three (i.e. of the form  $\exp(i3\phi)$ ) in the centre of the beam at the beam waist splits into three phase singularities of charge 1.

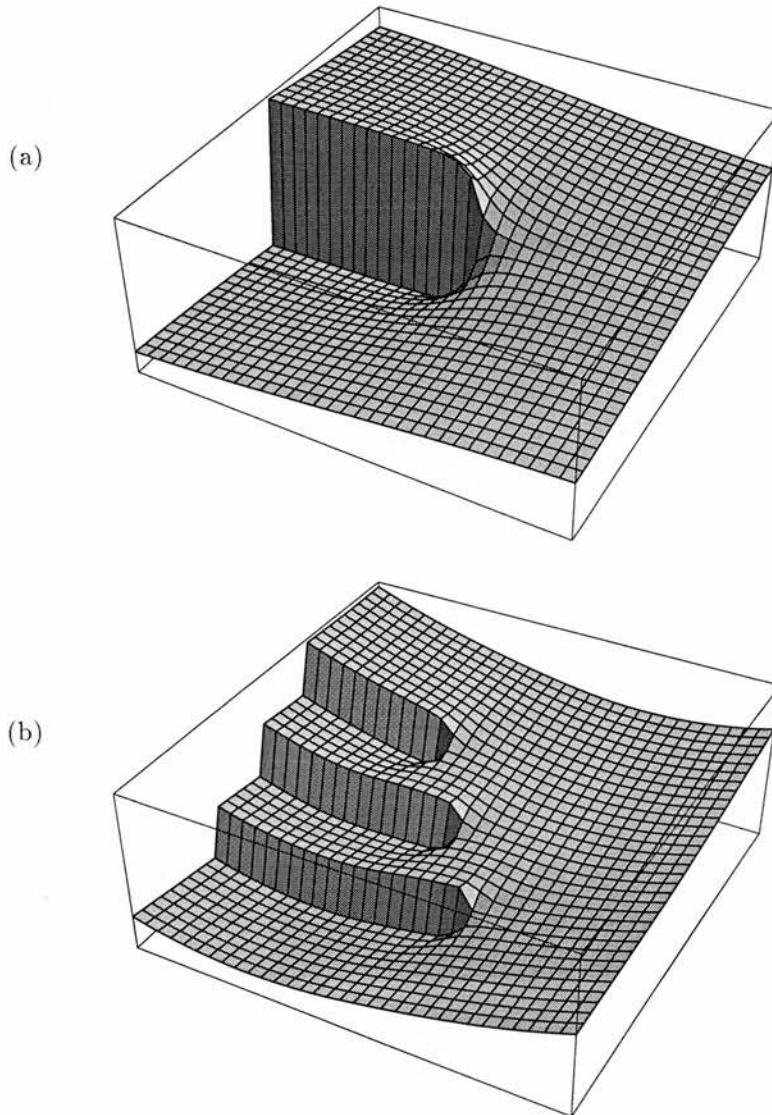


Figure A.3: Phase corresponding to bottom left (a) and the top right (b) beam cross-section in fig. A.2. Whereas the phase step in (a) is of magnitude  $3 \cdot 2\pi$ , the three phase steps in (b) are each of magnitude  $1 \cdot 2\pi$ . The end point of the phase step line in (a) therefore corresponds to a phase singularity of charge 3, those in (b) correspond to phase singularities of charge 1.

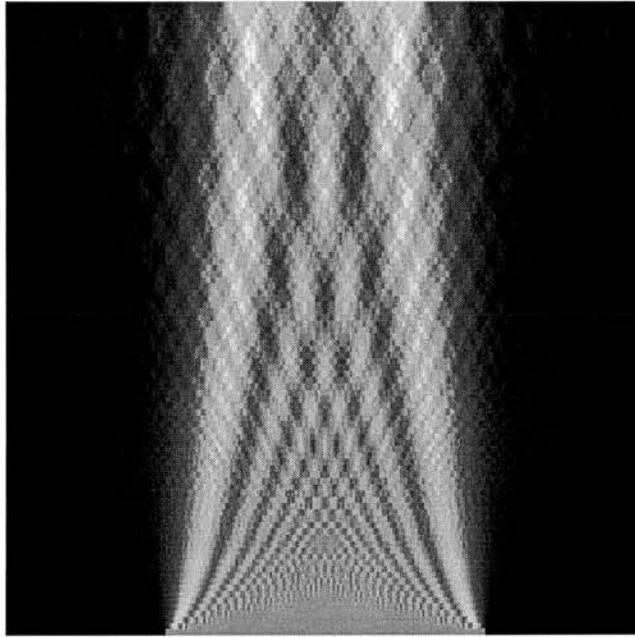


Figure A.4: Modelled intensity distribution after an infinitely long slit. The horizontal direction corresponds to the position across the beam, the vertical axis corresponds to the distance from the slit, which would be at the bottom of the graph. In this example, the extent in the horizontal direction corresponds to a physical width of 2mm, that in the vertical direction to 200mm. The wavelength is  $\lambda = 633\text{nm}$ .

quences of intensity patterns corresponding to consecutive planes can be readily generated (figures A.1 to A.2). In addition, information other than the intensity distribution, like for example the phase distribution (fig. A.3), can easily be extracted from the output of the model (see also fig. A.4).

## A.2 Description of the algorithm

The algorithm comprises four steps:

1. The two-dimensional Fourier transform of the cross-section of the electric field in the start plane,  $z = z_0$ ,

$$\tilde{e}_{z_0}(k_x, k_y) = \text{FT}\{e_{z_0}(x, y)\}(k_x, k_y), \quad (\text{A.1})$$

is calculated. This corresponds to a decomposition into two-dimensional plane waves of the form

$$\tilde{e}_{z_0}(k_x, k_y) \exp(-i(k_x x + k_y y)). \quad (\text{A.2})$$

$k_x$  and  $k_y$  are the corresponding wave numbers.

2. The two-dimensional plane waves identified in the previous step are cross-sections through the three-dimensional plane waves that superimpose to give the three-dimensional field  $e(x, y, z)$ . The  $k_x$  and  $k_y$  components of each three-dimensional plane wave are identical to those of its cross-section in the plane  $z = z_0$ , the  $k_z$  component of the three-dimensional wave is related to its  $k_x$  and  $k_y$  components by the condition

$$k = \frac{2\pi}{\lambda} = \sqrt{k_x^2 + k_y^2 + k_z^2}, \quad (\text{A.3})$$

which specifies that all the plane wave components have the same wavelength. If the coordinate system can be chosen such that

$$k_z > 0 \quad (\text{A.4})$$

for all plane wave components in the beam, then the  $k_z$  of each plane wave component can be calculated as

$$k_z = \sqrt{k^2 - k_x^2 - k_y^2}. \quad (\text{A.5})$$

3. On propagation through a distance  $\Delta z$  in the  $z$  direction, the cross-section through each plane wave changes by a phase  $-k_z \Delta z$ . Consequently, the amplitudes of the two-dimensional plane waves components of the beam cross-section in the plane  $z = z_0 + \Delta z$  are related to those in the plane  $z = z_0$  via

$$\tilde{e}_{z_0+\Delta z}(k_x, k_y) = \tilde{e}_{z_0}(k_x, k_y) \exp\left(-i\sqrt{k^2 - k_x^2 - k_y^2} \Delta z\right). \quad (\text{A.6})$$

4. The electric field in the plane  $z = z_0 + \Delta z$  is the inverse Fourier transform of its two-dimensional plane wave components  $\tilde{e}_{z_0+\Delta z}$ , i.e.

$$\begin{aligned} e_{z_0+\Delta z}(x, y) &= \text{FT}^{-1} \left\{ \text{FT}\{e_{z_0}(x, y)\}(k_x, k_y) \exp\left(-i\sqrt{k^2 - k_x^2 - k_y^2} \Delta z\right) \right\} (x, y). \end{aligned} \quad (\text{A.7})$$

### A.3 Limitations of the beam propagation program

The beam propagation program represents the electric field in a plane as a two-dimensional array of complex values of the electric field, sampled on the crossing points of a rectangular grid across a rectangular area  $A$  in that plane (fig. A.5). A discrete Fourier transform algorithm maps calculates corresponding points in Fourier space (or  $\mathbf{k}$  space), which lie in a rectangular area  $\tilde{A}$  (fig. A.5). If the field is zero outside  $A$ , and if the (continuous) Fourier transform is zero outside the area  $\tilde{A}$ , then the discrete Fourier transform of the two-dimensional array of values of the complex electric field represents the Fourier transform of the electric field, sampled on the crossing points of a rectangular grid across  $\tilde{A}$  [89].

Problems arise when the above conditions are not satisfied. Obviously, this can happen either by components of the beam lying outside the area  $A$ , or by Fourier components of the beam lying outside the corresponding area  $\tilde{A}$ .

When the beam is “loaded” into the program, i.e. when the array of values of the electric field is initially calculated, the area  $A$  must be chosen large enough to cover all of the beam cross-section. Such a ‘cropped beam’ has a different Fourier transform and propagates differently from the full beam.

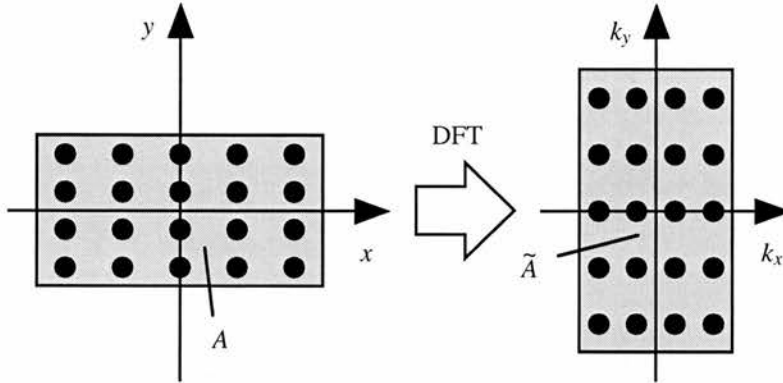


Figure A.5: Area represented by the data array in  $x$ - $y$  space ( $A$ ), and by the discrete Fourier transform (DFT) of the data array in  $k_x$ - $k_y$  space ( $\tilde{A}$ ).

An obvious problem with the condition that the beam cross-section has to be confined to an area happens on propagation of the beam, when parts of the beam ‘hit’ the boundary of the area  $A$ . Most discrete Fourier transform algorithms, like for example the well-known Fast Fourier Transform (FFT) algorithm, are derived for periodic boundary conditions [89] (see fig. A.6). The consequence for the beam propagation program, which uses such a discrete Fourier transform algorithm derived for periodic boundary conditions, is that parts of the beam which, on propagation, hit the boundary of the area  $A$  on one side, re-appear on the other side (fig. A.7). Note that the Fourier transform of each cross-section of a beam that has ‘hit’ the boundary is calculated correctly, but with insufficient detail. This is equivalent to the statement that the width of the area  $A$  in the  $x$  and  $y$  direction is proportional to the reciprocal of the separation in the  $k_x$  and  $k_y$  direction, respectively, of the points in the corresponding discrete Fourier transform, and that  $A$  is too small. In contrast, the Fourier transform of a beam cross-section that is simply clipped is different from that of the unclipped cross-section, as pointed out above.

The other condition, which is often not satisfied, is that the Fourier components of the beam lie within the area  $\tilde{A}$  in Fourier space. If this condition is satisfied/not satisfied in one plane  $z = z_0$ , it is satisfied/not satisfied in all other planes  $z = \text{const.}$  as the modulus of the Fourier components does not change on propagation. Similar to real space, the boundary conditions in Fourier space

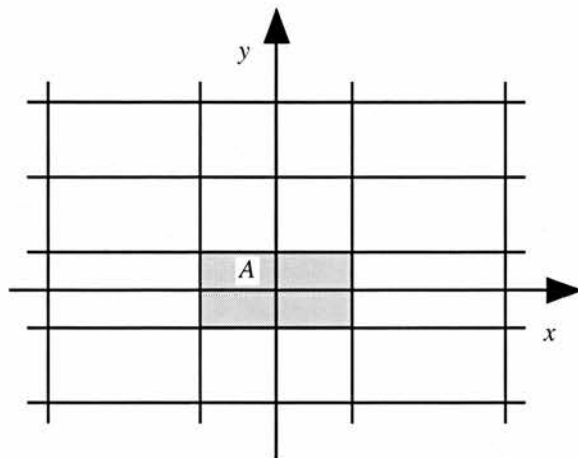


Figure A.6: The FFT algorithm interprets the area  $A$ , which is represented by the data array (Fig. A.5), as one tile in a periodic pattern of similar tiles. In the beam propagation program, these so-called *periodic boundary conditions* lead to problems with parts of the beam wandering out of the area  $A$  (fig. A.7).

are periodic. In complete analogy to fig. A.6, in which a plane  $z = \text{const.}$  is interpreted as a pattern of tiles similar to the rectangular area  $A$ , the corresponding plane in Fourier space is, as far as the discrete Fourier transform algorithm is concerned, a pattern of tiles in the shape of  $\tilde{A}$ . Components of the (continuous) Fourier transform of a beam cross-section, which lie outside  $\tilde{A}$ , are translated back into  $\tilde{A}$  (fig. A.8). Such a beam propagates very differently from the intended beam (fig. A.9).

As the respective length of  $\tilde{A}$  in the  $k_x$  and  $k_y$  direction is inversely proportional to the spacing  $\Delta x$  and  $\Delta y$  of the points in real space (just as the length of  $A$  in the  $x$  and  $y$  direction is inversely proportional to the spacing  $\Delta k_x$  and  $\Delta k_y$  of the points in Fourier space), the area  $\tilde{A}$  can be increased to any size by decreasing the separation between the points in real space, i.e. increasing the number of points used to sample the area  $A$ . Obviously, the corresponding memory requirements and processing time poses an upper limit on the number of sample points.

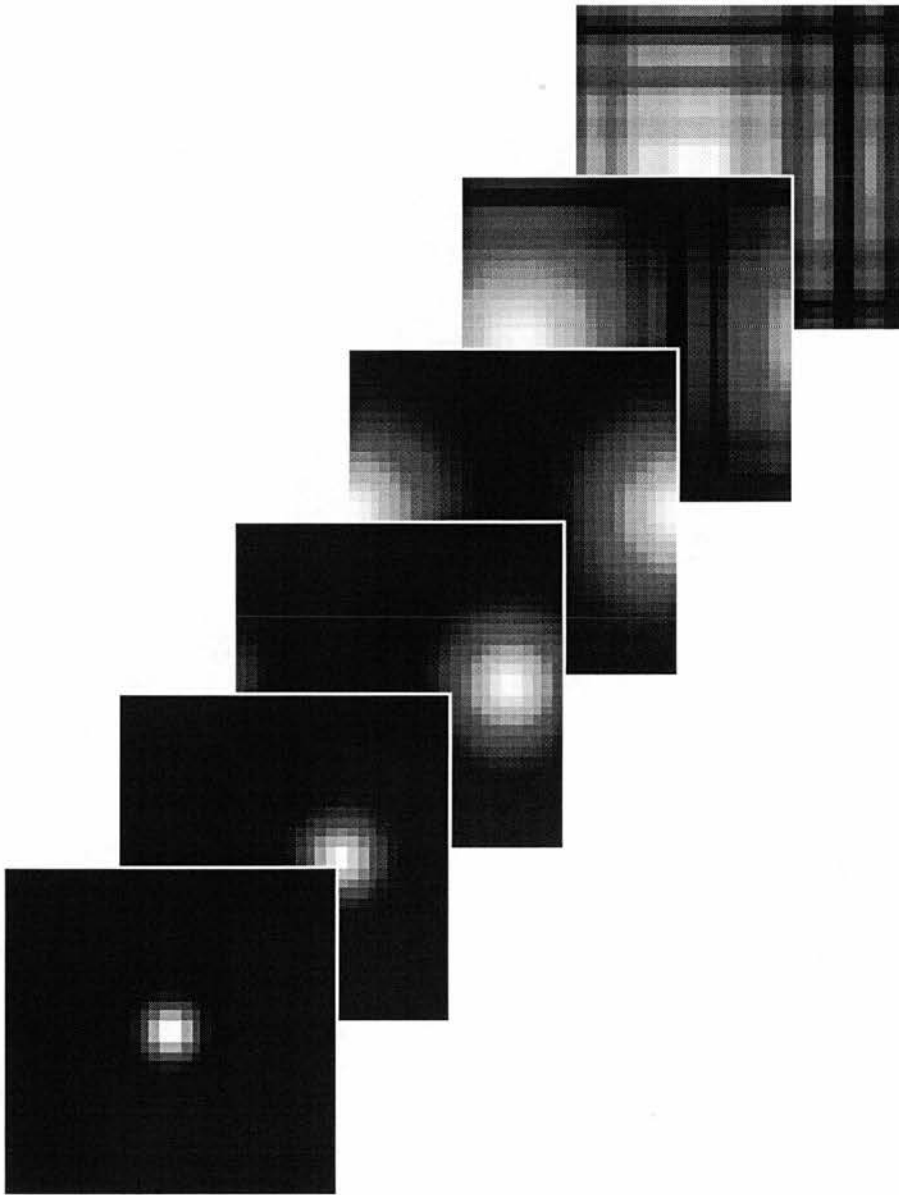


Figure A.7: Simulated intensity distributions of a Gaussian beam propagating at an angle to the  $z$  axis, which passes through the centre of each plot. If part of the beam leaves the simulated area, it reappears on the opposite side. In the last interference between the parts of the beam, which have re-entered the simulated area on the opposite side, and original parts of the beam can clearly be seen.

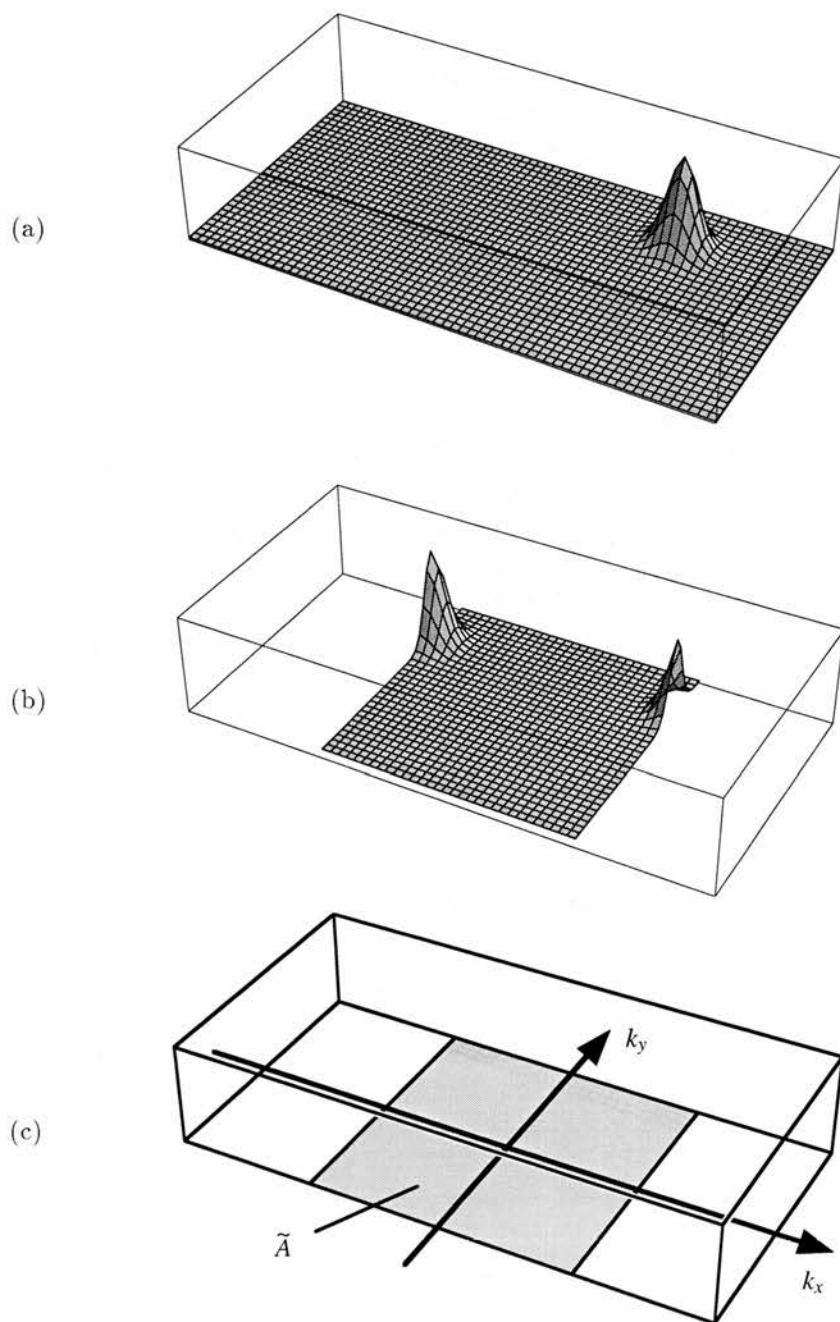


Figure A.8: Continuous (a) and discrete (b) Fourier spectrum of an inclined Gaussian beam. The area  $\tilde{A}$ , which corresponds to the sampling interval for the discrete Fourier transform, is shown in (c).

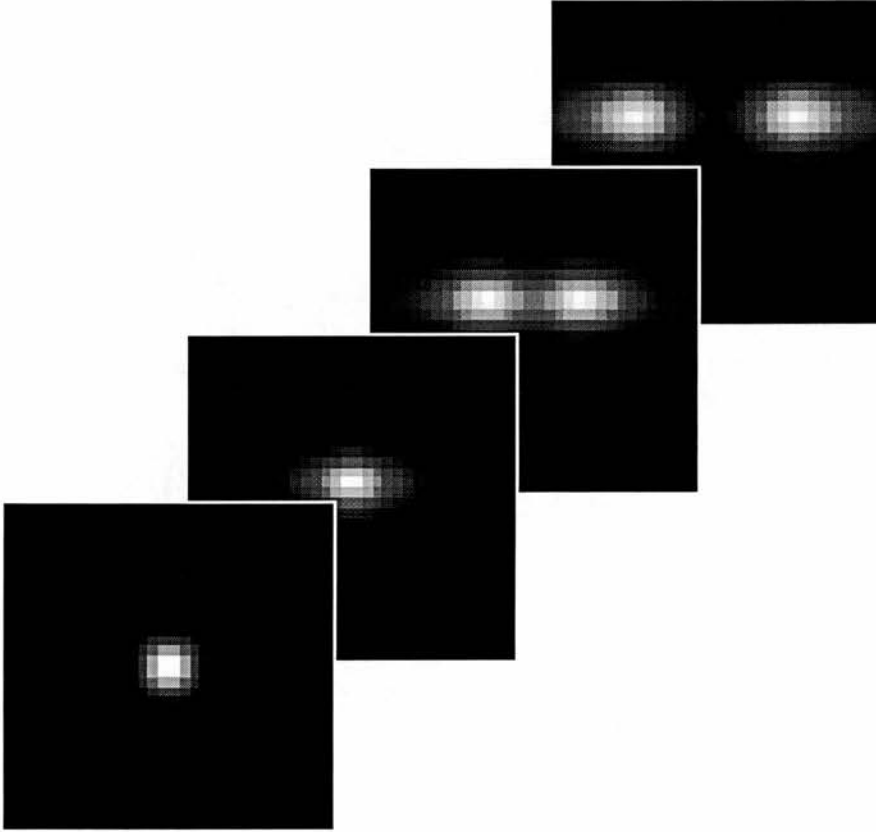


Figure A.9: Simulated propagation of a beam corresponding to the Fourier spectrum described in fig. A.8 (b). The beam was loaded into the package as a single Gaussian beam that propagates to the right. The propagation program interprets the beam as two non-Gaussian beams travelling in different directions.

# Bibliography

- [1] J. H. Poynting, "The Wave Motion of a Revolving Shaft, and a Suggestion as to the Angular Momentum in a Beam of Circularly Polarised Light," *Proc. R. Soc. London, Ser. A* **82**, 560–567 (1909).
- [2] L. Allen, M. W. Beijersbergen, R. J. C. Spreeuw, and J. P. Woerdman, "Orbital angular momentum of light and the transformation of Laguerre-Gaussian modes," *Phys. Rev. A* **45**, 8185–8189 (1992).
- [3] L. D. Landau and E. M. Lifshitz, *Mechanics* (Pergamon Press, Oxford, 1960).
- [4] R. P. Feynman, R. B. Leighton, and M. Sands, *The Feynman lectures on physics* (Addison-Wesley, Reading, Massachusetts, 1963), Vol. 1.
- [5] H. Goldstein, *Classical Mechanics* (Addison-Wesley, Reading, Massachusetts, 1962).
- [6] J. J. Sakurai, *Modern quantum mechanics* (Addison-Wesley, New York, 1985).
- [7] S. J. van Enk and G. Nienhuis, "Commutation rules and eigenvalues of spin and orbital angular momentum of radiation fields," *J. Mod. Opt.* **41**, 963–977 (1994).
- [8] R. A. Beth, "Direct Detection of the Angular Momentum of Light," *Phys. Rev.* **48**, 471 (1935).
- [9] R. A. Beth, "Mechanical Detection and Measurement of the Angular Momentum of Light," *Phys. Rev.* **50**, 115–125 (1936).

- [10] A. H. S. Holbourn, "Angular Momentum of Circularly Polarised Light," *Nature* **137**, 31 (1936).
- [11] N. Carrara, "Torque and Angular Momentum of Centimetre Electromagnetic Waves," *Nature* **164**, 882–884 (1949).
- [12] J. M. Vaughan and D. V. Willetts, "Interference properties of a light beam having a helical wave surface," *Opt. Commun.* **30**, 263–267 (1979).
- [13] M. W. Beijersbergen, L. Allen, H. E. L. O. van der Veen, and J. P. Woerdman, "Astigmatic laser mode converters and transfer of orbital angular momentum," *Opt. Commun.* **96**, 123–132 (1993).
- [14] L. Allen, M. J. Padgett, and J. Courtial, private communication, 1996.
- [15] H. He, M. E. J. Friese, N. R. Heckenberg, and H. Rubinsztein-Dunlop, "Direct Observation of Transfer of Angular Momentum to Absorptive Particles from a Laser Beam with a Phase Singularity," *Phys. Rev. Lett.* **75**, 826–829 (1995).
- [16] M. E. J. Friese, J. Enger, H. Rubinsztein-Dunlop, and N. R. Heckenberg, "Optical angular-momentum transfer to trapped absorbing particles," *Phys. Rev. A* **54**, 1593–1596 (1996).
- [17] N. B. Simpson, K. Dholakia, L. Allen, and M. J. Padgett, "Mechanical equivalence of spin and orbital angular momentum of light: an optical spanner," *Opt. Lett.* **22**, 52–54 (1997).
- [18] A. E. Siegman, *Lasers* (University Science Books, Mill Valley, California, 1968).
- [19] J. Durnin, "Exact solutions for nondiffracting beams. I. The scalar theory," *J. Opt. Soc. Am. A* **4**, 651–654 (1987).
- [20] J. Durnin, J. J. Miceli, Jr. and J. H. Eberly, "Diffraction-free Beams," *Phys. Rev. Lett.* **58**, 1499–1501 (1987).
- [21] M. Harris, C. A. Hill, P. R. Tapster, and J. M. Vaughan, "Laser modes with helical wave fronts," *Phys. Rev. A* **49**, 3119–3122 (1994).

- [22] C. Tamm, "Frequency locking of 2 transverse optical modes of a laser," *Phys. Rev. A* **38**, 5960–5963 (1988).
- [23] J. Courtial and M. J. Padgett, "Performance of a cylindrical lens mode converter for producing Laguerre-Gaussian laser modes," *Opt. Commun.* **159**, 13–18 (1999).
- [24] M. W. Beijersbergen, R. P. C. Coerwinkel, M. Kristensen, and J. P. Woerdman, "Helical-wavefront laser beams produced with a spiral phaseplate," *Opt. Commun.* **112**, 321–327 (1994).
- [25] G. A. Turnbull, D. A. Robertson, G. M. Smith, L. Allen, and M. J. Padgett, "The generation of free-space Laguerre-Gaussian modes at millimetre-wave frequencies by use of a spiral phaseplate," *Opt. Commun.* **127**, 183–188 (1996).
- [26] J. Courtial, K. Dholakia, D. A. Robertson, L. Allen, and M. J. Padgett, "Measurement of the rotational frequency shift imparted to a rotating light beam possessing orbital angular momentum," *Phys. Rev. Lett.* **80**, 3217–3219 (1998).
- [27] J. Courtial, D. A. Robertson, K. Dholakia, L. Allen, and M. J. Padgett, "Rotational Doppler shift of a light beam," *Phys. Rev. Lett.* **81**, 4828–4830 (1998).
- [28] V. Y. Bazhenov, M. V. Vasnetsov, and M. S. Soskin, "Laser beams with screw dislocations in their wavefronts," *JETP Lett.* **52**, 429–431 (1990).
- [29] N. R. Heckenberg, R. McDuff, C. P. Smith, and A. G. White, "Generation of optical-phase singularities by computer-generated holograms," *Opt. Lett.* **17**, 221–223 (1992).
- [30] J. Arlt, K. Dholakia, L. Allen, and M. J. Padgett, "The production of multiringed Laguerre-Gaussian modes by computer-generated holograms," *J. Mod. Opt.* **45**, 1231–1237 (1998).
- [31] N. B. Simpson, L. Allen, and M. J. Padgett, "Optical tweezers and optical spanners with Laguerre-Gaussian modes," *J. Mod. Opt.* **43**, 2485–2491 (1996).

- [32] I. V. Basistiy, V. Y. Bazhenov, M. S. Soskin, and M. V. Vasnetsov, "Optics of light beams with screw dislocations," *Opt. Commun.* **103**, 422–428 (1993).
- [33] J. Arlt, K. Dholakia, L. Allen, and M. J. Padgett, "Parametric down-conversion for light beams possessing orbital angular momentum," accepted for publication in *Phys. Rev. A*, 1999.
- [34] M. Zinner, "Laguerre-Gauß-Moden – Erzeugung und Einsatz in der Atomoptik," Diplomarbeit, Universität Hannover, unpublished, 1996.
- [35] J. Courtial, "Self-imaging beams and the Guoy effect," *Opt. Commun.* **151**, 1–4 (1998).
- [36] K. T. Gahagan and G. A. Swartzlander, "Optical vortex trapping of particles," *Opt. Lett.* **21**, 827–829 (1996).
- [37] K. Dholakia, "Atom hosepipes," *Contemp. Phys.* **39**, 351–369 (1998).
- [38] M. S. Soskin, V. N. Gorshkov, M. V. Vasnetsov, J. T. Malos, and N. R. Heckenberg, "Topological charge and angular momentum of light beams carrying optical vortices," *Phys. Rev. A* **56**, 4064–4075 (1997).
- [39] J. A. Arnaud and H. Kogelnik, "Gaussian Light Beams with General Astigmatism," *Appl. Opt.* **8**, 1687–1693 (1969).
- [40] S. J. van Enk and G. Nienhuis, "Angular momentum in evanescent waves," *Opt. Commun.* **112**, 225–234 (1994).
- [41] M. J. Padgett and L. Allen, "The Poynting vector in Laguerre-Gaussian laser modes," *Opt. Commun.* **121**, 36–40 (1995).
- [42] M. J. Padgett, J. Arlt, N. B. Simpson, and L. Allen, "An experiment to observe the intensity and phase structure of Laguerre-Gaussian laser modes," *Am. J. Phys.* **64**, 77–82 (1996).
- [43] R. Kingslake, "The interferometer patterns due to the primary aberrations," *Trans. Opt. Soc. Lond.* **27**, 94–105 (1926).
- [44] C. Candler, *Modern Interferometers* (Hilger & Watts, London, 1951).

- [45] J. Courtial, K. Dholakia, L. Allen, and M. J. Padgett, "Gaussian beams with very high orbital angular momentum," *Opt. Commun.* **144**, 210–213 (1997).
- [46] A. Yariv, *Optical Electronics*, 3rd ed. (Holt, Rinehart and Winston, New York, 1985).
- [47] K. Dholakia, N. B. Simpson, M. J. Padgett, and L. Allen, "Second-harmonic generation and the orbital angular momentum of light," *Phys. Rev. A* **54**, R3742–R3745 (1996).
- [48] G. D. Boyd and D. A. Kleinmann, "Parametric Interaction of Focused Gaussian Light Beams," *J. Appl. Phys.* **39**, 3597–3639 (1968).
- [49] M. Harris, C. A. Hill, and J. M. Vaughan, "Optical helices and spiral interference fringes," *Opt. Commun.* **106**, 161–166 (1994).
- [50] E. A. Sziklas and A. E. Siegman, "Mode calculations in unstable resonators with flowing saturable gain. 2: Fast Fourier transform method," *Appl. Opt.* **14**, 1874–1889 (1975).
- [51] J. Courtial, K. Dholakia, L. Allen, and M. J. Padgett, "Second harmonic generation and the conservation of orbital angular momentum with high-order Laguerre-Gaussian modes," *Phys. Rev. A* **56**, 4193–4196 (1997).
- [52] K. Patorski, "The self-imaging phenomenon and its applications," *Progr. Opt.* **XXVII**, 3–108 (1989).
- [53] E. Abramochkin and V. Volostnikov, "Spiral-type beams," *Opt. Commun.* **102**, 336–350 (1993).
- [54] E. Abramochkin and V. Volostnikov, "Spiral-type beams: optical and quantum aspects," *Opt. Commun.* **125**, 302–323 (1996).
- [55] E. Abramochkin and V. Volostnikov, "Generation of spiral-type laser beams," *Opt. Commun.* **141**, 59–64 (1997).
- [56] I. Kimel and L. R. Elias, "Relations Between Hermite and Laguerre Gaussian Modes," *IEEE J. Quantum Electr.* **29**, 2562–2567 (1993).

- [57] M. Brambilla, F. Battipede, L. A. Lugiato, V. Penna, F. Prati, C. Tamm, and C. O. Weiss, "Transverse laser patterns. I. Phase singularity crystals," *Phys. Rev. A* **43**, 5090–5113 (1991).
- [58] V. V. Kotlyar, V. A. Soifer, and S. N. Khonina, "An algorithm for the generation of laser beams with longitudinal periodicity: rotating images," *J. Mod. Opt.* **44**, 1409–1416 (1997).
- [59] C. Paterson and R. Smith, "Helicon waves: propagation-invariant waves in a rotating coordinate system," *Opt. Commun.* **124**, 131–140 (1996).
- [60] E. Hecht, *Optics* (Addison-Wesley Publishing Company, Reading, Massachusetts, 1987).
- [61] B. A. Garetz, "Angular Doppler effect," *J. Opt. Soc. Am.* **71**, 609–611 (1981).
- [62] F. Bretenaker and A. Le Floch, "Energy Exchanges between a Rotating Retardation Plate and a Laser Beam," *Phys. Rev. Lett.* **65**, 2316 (1990).
- [63] R. Simon, H. J. Kimble, and E. C. G. Sundarshan, "Evolving Geometric Phase and Its Dynamical Manifestation as a Frequency Shift: An Optical Experiment," *Phys. Rev. Lett.* **61**, 19–22 (1988).
- [64] G. Nienhuis, "Doppler effect induced by rotating lenses," *Opt. Commun.* **132**, 8–14 (1996).
- [65] L. Allen, M. Babiker, and W. L. Power, "Azimuthal Doppler shift in light beams with orbital angular momentum," *Opt. Commun.* **112**, 141–144 (1994).
- [66] S. M. Barnett, M. Babiker, and L. Allen, private communication, 1997.
- [67] M. J. Padgett and J. P. Lesso, "Dove prisms and polarised light," *J. Mod. Opt.* **46**, 175–179 (1999).
- [68] J. Lesurf, *Millimetre-wave Optics: Devices and Systems* (IOP Publishing Ltd., Bristol, England, 1990).

- [69] G. M. Smith, "TEOs at mm-wave frequencies and their characterisation using quasi-optical techniques," Ph.D. Thesis, University of St Andrews, 1990.
- [70] S. C. Tidwell, D. H. Ford, and W. D. Kimura, "Generating radially polarized beams interferometrically," *Appl. Opt.* **29**, 2234–2239 (1990).
- [71] P. L. Greene and D. G. Hall, "Diffraction characteristics of the azimuthal Bessel-Gauss beam," *J. Opt. Soc. Am. A* **13**, 962–966 (1996).
- [72] A. H. F. van Vliet and T. de Graauw, "Quarter wave plates for submillimeter wavelengths," *Int. J. Infrared and Millimeter Waves* **2**, 465–477 (1981).
- [73] M. Born and E. Wolf, *Principles of Optics* (Pergamon Press, Oxford, 1980).
- [74] S. J. van Enk, "Geometric phase, transformations of gaussian light beams and angular momentum transfer," *Opt. Commun.* **102**, 59–64 (1993).
- [75] B. A. Garetz and S. Arnold, "Variable frequency shifting of circularly polarized laser radiation via a rotating half-wave retardation plate," *Opt. Commun.* **31**, 1–3 (1979).
- [76] M. J. Padgett and J. Courtial, "A Poincaré-sphere equivalent for light beams containing orbital angular momentum," *Opt. Lett.* **24**, 430–432 (1999).
- [77] B. B. Mandelbrot, *The Fractal Geometry of Nature* (Freeman, San Francisco, New York, 1982).
- [78] D. Avnir, O. Biham, D. Lidar, and O. Malcai, "Is the Geometry of Nature Fractal?," *Science* **279**, 39–40 (1998).
- [79] N. Lu, *Fractal Imaging* (Academic Press, San Diego, 1997).
- [80] H.-O. Peitgen, H. Jürgens, and D. Saupe, *Chaos and Fractals: new frontiers of science* (Springer, New York, 1992).
- [81] I.-F. Shih, D. B. Chang, and N. L. Moise, "Analog Optical Processing for the construction of Fractal Objects," U.S. Patent 5132831, 1992.

- [82] M. F. Barnsley and S. Demko, "Iterated function systems and the global construction of fractals," *Proc. R. Soc. Lond. A* **399**, 243–275 (1985).
- [83] M. F. Barnsley and L. P. Hurd, *Fractal image compression* (AK Peters Ltd., Wellesley, MA, 1993).
- [84] J. Uozumi and T. Asakura, in *Current Trends in Optics*, J. C. Dainty, ed., (Academic Press, London, 1994).
- [85] T. M. Roach, H. Abele, M. G. Boshier, H. L. Grossman, K. P. Zetie, and E. A. Hinds, "Realization of a magnetic-mirror for cold atoms," *Phys. Rev. Lett.* **75**, 629–632 (1995).
- [86] J. W. Goodman, *Introduction to Fourier Optics* (McGraw-Hill, New York, 1968).
- [87] J. P. Lesso, A. J. Duncan, W. Sibbett, and M. J. Padgett, "Surface profilometry based on polarization analysis," *Opt. Lett.* **23**, 1800–1802 (1998).
- [88] *Mathematica* (Wolfram Research, Inc., Champaign, Ill., 1994).
- [89] W. H. Press, S. A. Teukolsky, W. T. Vetterling, and B. P. Flannery, *Numerical Recipes in C*, 2nd ed. ed. (Cambridge University Press, Cambridge, United Kingdom, 1995).

